Study on Methods for Performance Improvement of Thermionic RF Gun

Konstantin Torgasin

Abstract

Thermionic electron radio frequency (RF) guns are cost effective and simple in operation electron sources which are used for Free Electron Laser (FEL) facilities. The performance of the FEL is determined by the quality of the electron beam produced by the RF gun. In this research the feasibility of improvement of performance of thermionic RF gun was studied as proof of principles based on two methods.

The first method concerns the modification of thermionic RF gun to a *Back-Bombardment-less* RF gun (triode type) by introduction of a quarter wavelength pre-bunching cavity. It is a unique work for drastic reduction of the Back-Bombardment Effect. This study was focused on testing of such a pre-bunching cavity. The results of high power test revealed the large impact of secondary electron emission, which limits the cavity voltage. The secondary electron emission processes were identified as multipactoring. The study gives reasonable suggestion for the measures to suppress the multipactoring.

The second method concerns the application of a laser pulse on thermionic materials for electron emission. The special feature of this method is the application of Thermally Assisted Photoemission (TAPE) effect. This effect allows us to increase the Quantum Efficiency of the cathode material by heating up the cathode. In this research the TAPE was demonstrated on two materials LaB_6 and CeB_6. The quantum efficiency could be raised by one order of magnitude in the heating range of $1000-1600$ K. Another important result is that TAPE enables us to extract the electrons from the cathode material with the incident photon energy below the work function as a single photon absorption process.

Contents

List of Figures

List of Tables

Chapter 1

Introduction

1.1 Motivation

The research described in this thesis was conducted with the aim to improve performance of the thermionic RF gun, which is used at Kyoto University- Free Electron Laser (KU-FEL) facility.

The KU-FEL was constructed at the Institute of Advanced Energy (IAE) to conduct research on energy harvesting materials. In particular the KU-FEL is used for *Mode Selective Phonon Excitation* (MSPE) experiments for study of wide-gap semiconductors as candidates for *next generation solar cells*, such as SiC, TiO_2 and ZnO [1].

The target of the study is the development of a method to increase the charge per bunch and to extend the macropulse duration of the electron beam as generated by thermionic RF gun. Therefore, two methods are investigated as a proof of principles:

- Modification of the thermionic RF gun to the triode-type one for operation in thermionic mode.
- Increase of photoemission quantum efficiency using the Thermally Assisted Photoemission for operation in photoemission mode.

The triode structure of the gun would allow us to reduce the major drawback of a thermionic RF gun, which is called the *Back-Bombardment Effect* (BBE) (see chapter 3). By this means the beam peak current is expected to be increased.
If a short laser pulse is used for electron extraction in a thermionic RF gun, the BBE doesn't occur. In this mode the performance is limited by availability of laser systems. The increase of cathode quantum efficiency using Thermally Assisted Photoemission (TAPE) is expected to increase the efficiency of a given laser system at the same costs.
The increase in peak current and macropulse duration of the electron beam produced by the RF gun, would allow us to extend the spectral range of a oscillator type FEL and to increase its radiation power.

1.2 Thesis Overview

The thesis is organized in following structure:

- The first two chapters give an introduction into the basic concepts of accelerating technology, necessarily for understanding of experimental work, which is described in this thesis. In particular, the electron generation and acceleration using RF guns.
- Chapter 3 describes the Back-Bombarding Effect (BBE) as the main drawback of the thermionic RF electron guns and provides a short overview over conventional methods to mitigate it.

- Chapter 4 describes the concept of modification on thermionic RF gun which is used for Kyoto University-FEL (KU-FEL) facility. The modification of the 4.5-cell thermionic RF gun to triode-type one, allows us to reduce the BBE and to improve the beam quality. The experimental work is focused on the test of properties of a pre-bunching quarter wavelength triode cavity.

- Chapter 5 describes the study on Thermally Assisted Photoemission (TAPE) effect. This effect concerns the usage of thermionic materials for laser excitation. Such approach allows us to avoid the BBE and to increase the quantum efficiency of the electron emitting material.

- Chapter 6 gives the summary of the main results of the thesis.

For better understanding of the technical details of the experimental work presented in last chapters, the following sections give an overview over the structure of a typical FEL and of the KU-FEL facility.

1.2.1 Free Electron Laser (FEL)

In general the Free Electron Laser technology can generate coherent radiation with tunable wavelength, short pulse length, high peak and average power. This properties make the FEL radiation convenient for synchronization in pump-probe experiments. The FEL is a suitable tool for principal excitation in condensed matter systems such as excitation of plasmons, phonons, magnons and intersubband transitions [2]. The table 1.1 summarizes application fields for FEL radiation.

Table 1.1: Summary of application of FEL radiation [3]

Wavelength region	Application fields	Examples
THz-FEL	Solid-state-physics	Interband dynamics in semiconductors and quantum dots Non-linear optics Spin dynamics Vibration spectroscopy
MIR-FEL	Solid-state-physics Chemistry Medicine	Dynamics of phonons in solid materials Chemical analysis Thin-film fabrication Selective removal of harmful substances
NIR-visible- FEL	Chemistry	Time-resolved polarized fluor. spectroscopy
X-FEL	Biochemistry Physics Chemistry	Structural analysis of proteins X-ray photoelectron spectroscopy Observation of atomic motion

The FEL facilities are based on vacuum acceleration technology, hence its construction requires high costs and occupies large space. The research on improvement of FEL performance is highly demanded. The FEL uses electron beam as radiation amplification medium. For this reason the electron acceleration technology is a basic technique of any FEL facility. The typical FEL facility consists of an electron gun, an electron accelerator and of an undulator. In the electron gun the electron beam is generated and accelerated. After filtering and focusing of the electron beam to required kinetic energy and trajectory, the beam is accelerated in the accelerator section. The high energetic beam is introduced to an undulator. The undulator consists of magnets with alternating pole sequence. Such

magnetic configuration forces the electron beam to a sinusoidal trajectory. The electrons emit periodically radiation by each oscillation. The electron beam is deflected and usually damped after one passage through the undulator. If the amplitude of the beam oscillation is small, the radiation shows interference patterns with narrow energy bands. The emitted radiation is oscillating back- and forwards between two mirrors placed at both ends of the undulator. After several passes through the undulator the radiation is coupled out. This is so called oscillator configuration.

The Figure 1.1 illustrates the basic structure of an oscillator type FEL facility. A list of long wavelength FEL facilities from over the world is given in appendix. According to the list the majority of FEL facilities belong to the oscillator type.

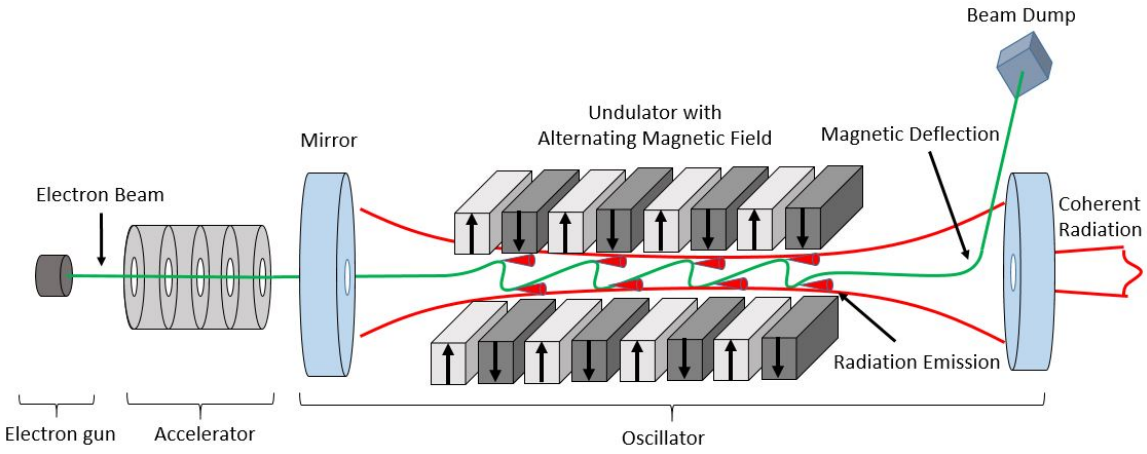

Figure 1.1: Basic structure of an oscillator type FEL facility.

1.2.2 Electron Beam Quality Required for FEL Lasing

Specific electron beam qualities have to be achieved to obtain radiation from oscillator type FEL. These are:

- High peak power
- Narrow energy spread
- Small transverse emittance
- Stable bunch interval
- Stable beam energy
- Effective macropulse duration

The list of beam qualities required for oscillator type FEL is taken from [4].

There are 2 types of RF guns usually used to create the electron beam with corresponding properties. These are the thermionic RF gun and the photo-cathode RF gun. Depending on application both have own advantages and disadvantages, which are mentioned in the next section.

1.2.3 Thermionic and Photo-Cathode RF guns

The table1.2 summarizes the advantages and disadvantaged of the thermionic and photo-cathode RF guns.

The thermionic RF gun, to which the methods studied in this thesis are intended to be applied, belongs to the Kyoto University Free Electron Laser (KU-FEL). Therefore, it is reasonable to give a brief introduction into the facility.

Table 1.2: Thermionic RF Gun versus Photo-RF Gun

	Thermionic RF Gun	Photo-RF Gun
Advantages	High rep. rate (high average current)	Short pulses (bunching)
	Compact structure	High fields
	Easy in operation	Higher achievable current densities
	Moderate costs	No Back-Bombardment Effect
Disadvantages	Long micropulse duration	Requirement of special photocathodes: >Long life time >High quantum efficiency >High vacuum conditions
	Large energy spread	Requirement for special laser systems: >Nonlinear wavelength conversion >Uniformity in pulse shape >Phase stability with timing jitter lower than the pulse length >High rep. rate
	Limited peak current	High costs
	High impact from BBE	Complex operation

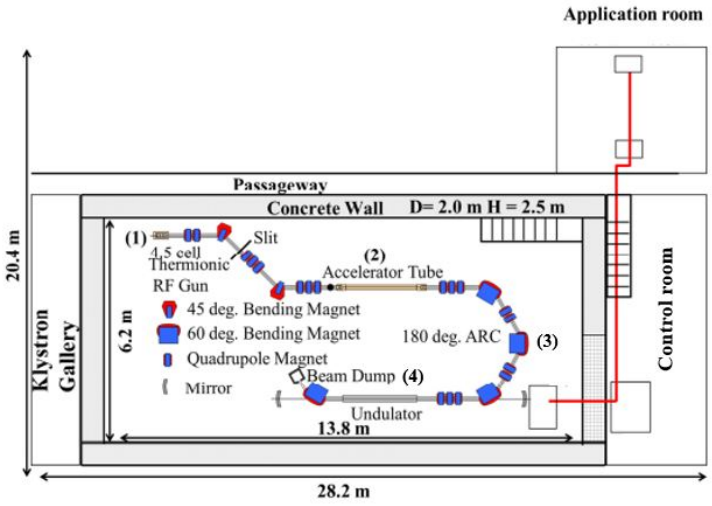

Figure 1.2: Structure of oscillator type Kyoto University-FEL facility [3].

1.3 KU-FEL Facility

The Kyoto University Free Electron Laser (KU-FEL) is a mid-infrared oscillator type FEL facility constructed at the Institute of Advanced Energy (NAE), Kyoto University. The top view on the structure of the facility is shown in Fig.1.2. There are 4 main components of the facility. (1) The 4.5-cell thermionic RF gun with dog-leg shaped energy filter for $8MeV$ electrons. (2) A 3- meters long travelling wave linear accelerator (linac) for acceleration of electrons to $40MeV$. (3) A 180°- bunch compressor. The final component (4), is an optical oscillator consisting of an undulator and 2 mirrors.

1.3.1 KU-FEL Performance

A summary of current performance of the facility is given in the table 1.3. The available radiation spectra are shown in Fig.1.3.

Table 1.3: Specifications of KU-FEL facility [3].

Tunable wavelength range ($> 1mJ$)	$5 - 22\mu m$
Maximal pulse energy	$30mJ(@8\mu m)$
Maximal peak power	$8MW(@8\mu m)$
Spectral width	$\sim 3\%$
Macropulse duration (FWHM)	$\sim 2\mu m$
Micropulse width (FWHM)	$< 0.6ps(@12\mu m)$
Wavelength stability (FWHM)	$< 1.3\%(@12\mu m)$
Repetition rate of micropulse	$2856MHz$

The electron beam quality is mainly determined by the 4.5-cell thermionic RF gun. For this reason the next section describes the RF gun.

1.3.2 4.5-Cell Thermionic RF Gun of KU-FEL Facility

The gun consists of 4 and 1/2 cells and is supplied by $10MW$ power from a klystron at resonance frequency of $2856MHz$. A LaB_6 cathode at $1600°C$ is used for generation and acceleration of electrons up to $8MeV$. The gun was designed also for operation in photo-excitation mode. For that reason a laser port was integrated into the first half cell. The Figure 1.4 shows the photo of the gun (Fig.1.4a) and its cross-sectional drawing (Fig.1.4b).

The 4.5-cell RF gun can be operated in thermionic and photo-excitation modes. The comparison of performances in both modes for lasing at $11.7\mu s$ using the same LaB_6 cathode is showed in the table 1.4.

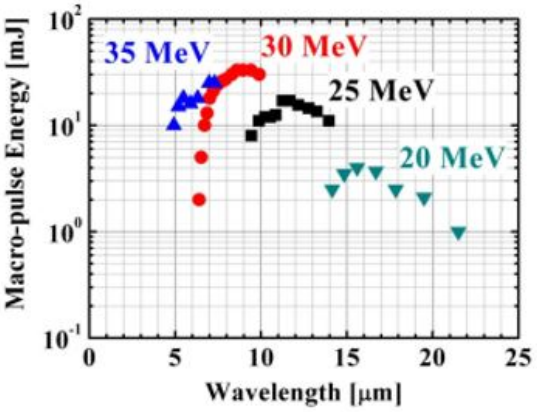

Figure 1.3: Tunability of the KU-FEL [3].

As given in the table the photo-excitation mode produces 3 times higher micro bunch current. The bunch charge in thermionic mode depends on cathode temperature. However, the further increase of the cathode temperature would rise the current in non-linear correlation (positive feedback) due to the BBE. Hence the cathode temperature is also limited. Further the macropulse of the electron beam in photo-excitation mode is limited to $4\mu s$ by the given laser system.

In present configuration the thermionic mode generates higher FEL macropulse energy than the photo-excitation mode due to the higher repetition rate. In thermionic mode the macropulse radiation energy can be further improved by increasing the electron bunch charge and electron beam macropulse duration, if the impact of the BBE is reduced. In the photo-excitation mode the improvement can be attained increasing the quantum efficiency of the cathode. In this thesis both methods were investigated as a proof of principles:

1. Feasibility of triode-type thermionic RF gun configuration.

2. Feasibility of quantum efficiency increase by Thermally Assisted Photoemission.

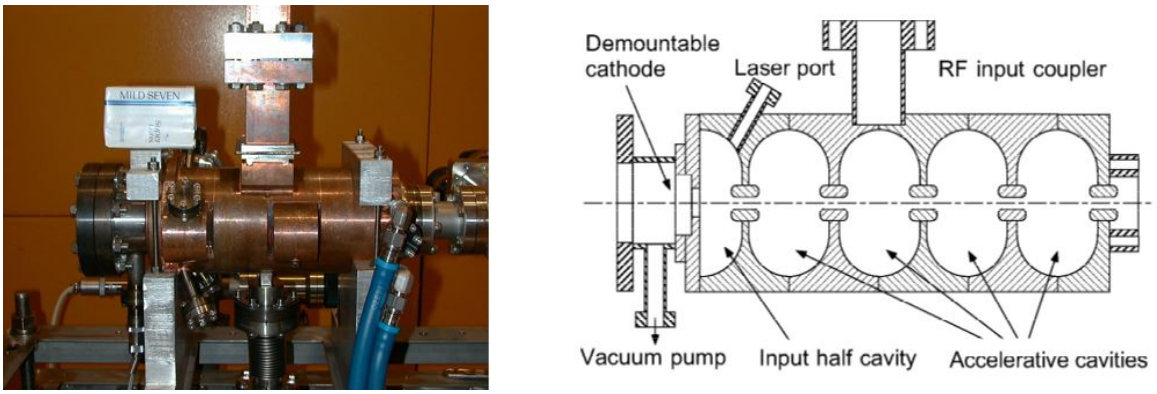

(a) Photographic view **(b)** Cross-section

Figure 1.4: 4.5-cell thermionic RF gun of KU-FEL facility.

1.4 Summary

In this chapter the motivation and the target of the research described in this thesis was given. Further the basic principles of the oscillator type Free Electron Laser were introduced. The structure and performance of the Kyoto-University Free Electron Laser (KU-FEL) facility were described. From the point of energy science this thesis is related to the improvement of the beam quality produced by a thermionic RF gun targeting the improvement of performance of KU-FEL for investigation of energy related materials.

In the next chapter the basic physical concepts for electron beam extraction and acceleration are introduced.

Table 1.4: Characteristics of performance of KU-FEL operated in thermionic and photo-excitation modes [5]

	Thermionic mode	***Photo-excitation mode***
Electron micro bunch charge	$< 50pC$	$150pC$
Electron beam macropulse duration	6.5 μs	4 μs
Micropulse rep. rate	2856 MHz	29.7 MHz
Macropulse duration	2 μs	2 μs
Macropulse energy	13 mJ	0.8 mJ
Micropulse energy	2 μJ	13 μJ

Chapter 2

Electron Beam Generation

The basic target of particle accelerating technologies is the generation of high brightness particle beams. The beams can be processed then for particular application in high energy physics or in material studies. Usually the beam generation is carried out in three steps:

- **Particle Emission**
- **Beam Conditioning**
- **Beam Acceleration**

The table 2.1 summarizes the technical principles of beam generation.
The electron sources are classified according to emission mechanisms: thermionic, photoelectric and field emission. The manipulation of transverse and longitudinal beam distribution belongs to beam conditioning process. Beam conditioning is required in order to match the beam's properties to the design of beam line system. The last point is the acceleration.

Table 2.1: High brightness electron beam generation (adapted from [9])

Emission	Beam conditioning	Acceleration
Thermionic cathode	Emittance compensation	Capture into booster
Photocathode	Ballistic compression	Emittance preservation
Field emission cathode	Magnetic compression	Longitudinal phase space compression
	RF compression	Chirping for bunch compressors

2.1 Electron Emission

For FEL facilities electron beams of high energy, high current, and small divergence are required. Generation of electron beams is based on four factors [10]:

- The cathode, electron emitting material
- A source of energy for extraction the electrons from the cathode
- An electric field for acceleration and beam conditioning
- A vacuum environment for protection from contamination and prevention of scattering on air molecules.

In this chapter these points are described in more details.

The electron density bound in the cathode material is several orders of magnitude higher than the density of extracted electrons. In metals for example the conductive band has roughly one electron per atom ($10^{22} - 10^{23} electrons/cm^2$). A cylindrical electron bunch of $6ps$ long and $200\mu m$ in diameter with charge of $1nC$ contains $1.1 \times 10^{14} electrons/cm^3$. There is about eight order of magnitude difference between bound and free extracted electrons. The thermal energy of the bound electrons is low. At room temperature ($300K$)

for example the thermal energy of electrons around Fermi level in copper is about $0.02eV$. Whereas electron extraction by heating to $2500K$ produces the beam with thermal energy of $0.20eV$ [11].

The electrons are bound in the conducting material. In order to liberate an electron from the bulk material to the vacuum close to the surface a thermodynamic work, called *Work Function* has to be applied. The work function ϕ is defined as:

$$\phi = E - E_f, \tag{2.1}$$

where, E is the total amount of energy required to extract the electron from the lowest free energy state into infinity, and E_f is the highest occupied energy state of an electron in the material (at $0K$). There are three main mechanism to overcome work function and three cathode types respectively:

- *Thermionic Cathode*
- *Photocathode*
- *Field Emission Cathode.*

2.1.1 Photoemission

According to the photo-electric effect the electrons can leave the material by absorbing a photon with an energy equal or higher than the work function $h\nu \geq \phi$. In the high energy photocathode guns high energetic laser pulses are used for emission of electron bunches. This method has advantage of high achievable accelerating fields and flexibility of electron bunch format.
According to the *Spicer's* model the photoemission process is described by 3 steps [12]:

1. *Photon absorption by the electron in conductive band*
2. *Electron transfer to the material surface*
3. *Electron escape into the vacuum*

The energy spread of photo-emitted electrons is proportional to the photon energy.

2.1.2 Thermionic Emission

The electrons are extracted by heating the cathode material. The kinetic energy of electrons overcomes work function due to heating.The thermionic emission current is given by *Richardson-Dushman* equation [13]:

$$J = A_G T^2 exp(-\frac{\phi}{k_B T}), \tag{2.2}$$

where, $A_G = A_0 \lambda_B (1 - r)$ is a generalized Richardson constant, the $A_0 = 1.2 \times 10^6 \frac{A}{m^2 K^2}$ is the universal Richardson constant, λ_B is a band-structure related correction factor, r is reflectivity, T is temperature in Kelvin and $k_B (= 8.617 \times 10^{-5} \frac{eV}{K})$ is the Boltzmann constant.

The usual criteria to characterize thermionic emitters are: (1) Current density, (2) Beam quality (angular divergence of emitted electrons), (3) Poisoning resistance (operation in low vacuum pressure) and (4) lifetime.

2.1.3 Field Emission

An external electric field reduces the work function. This process is called the *Schottky Effect* [14]. The corresponded current density is described by the Richardson-Dushman

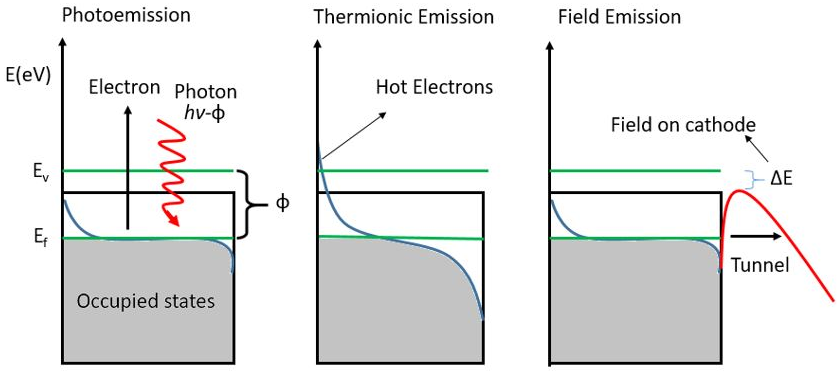

Figure 2.1: Schemata of electron extraction mechanisms

equation including the reduced potential ΔE:

$$J = A_G T^2 e^{-\frac{(E_f - \Delta E)}{k_B T}} \tag{2.3}$$

The reduced potential barrier allows tunnelling for electrons from Fermi level to the vacuum. Conventional field emitters have a shape of sharp needles and blade edges. Since the needles are fragile when heated, it is difficult to find stable operating conditions for field emission cathodes. Field emission cathodes are usually applied in electron microscopy.
The three mentioned electron extraction mechanisms are illustrated in the Fig. 2.1. The E_f, E_v represent the Fermi energy level and the vacuum level of the cathode material. The ϕ is the work function and the ΔE is the reduced potential due to the Schottky effect, the $h\nu$ is photon energy.

2.2 Electron Acceleration

Charged particles can be accelerated by electric fields. For example the electric field between two metallic plates in diode configuration. Under assumption of thermionic emission the electrons are emitted from the cathode plate as voltage between the electrodes

is applied. The initial potential gradient is linear. All the electrons emitted from the cathode reach the anode. The current produced by the cathode in this case is said to be *temperature limited*. The magnitude of the current is mainly determined by the cathode temperature. The emitted electrons create space charge, that causes opposing field. The opposing field is rising with the number of emitted electrons until the field at the cathode surface becomes zero. The electron emission stops then. The net electric field on the cathode surface acts as limiting factor for current emission. In this case the flowing current is said to be *space-charge limited*. The current is determined by the voltage applied to the anode. The threshold current density J is described by *Child-Langmuir Law* [15].

$$J = \frac{4}{9}\varepsilon_0\sqrt{2(e/m_e)}\frac{V^{3/2}}{d^2} \tag{2.4}$$

Substitution of values of e, m_e, ε_0 gives simplified expression

$$J = 2.33 \times 10^{-6}\frac{V^{3/2}}{d^2} \tag{2.5}$$

where V is the potential difference between the electrodes and d is spacing. At a sufficiently high potential the current emitted from the cathode becomes temperature-limited. Figure 2.2 shows a schematic current density versus voltage diagram with arbitrary chosen parameters. The figure illustrates temperature limited and space-charge limited operational regimes.

2.3 Electron Gun

Electron gun is a device for generation and shaping of charged particles in a proper form for injection into an accelerator. General components of an electron gun are the electron

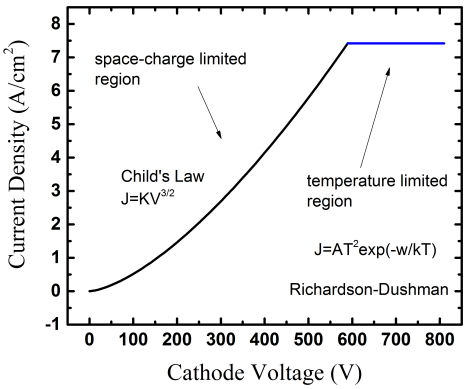

Figure 2.2: J-V curve of a thermionic DC electron gun

emitting material, accelerating field and focusing elements. A simple gun has a configuration of a diode with electron emitting material set at non-zero potential as cathode and earthed anode plate with an electron extraction aperture. The kinetic energy of extracted electrons is determined by the voltage between the cathode and anode. Additional electrodes can be used for focusing. Figure 2.3 shows a schematic view of an electron gun. An ideal electron gun produces beam with uniform current density.

The electrons produce space charge fields, which apply transverse defocusing forces on the beam. As a result the beam is diverging with the distance by an angle θ. For many applications a parallel beam with $\theta = 0$ is desired. By an optimal design of focusing electrodes, the external fields can compensate for space charge defocusing. It is so called *Pierce Condition* [16]. According to the Langmuir Child's law the space charge limited current density in a parallel diode is $j \sim V^{3/2}$. Typical distance between cathode and anode is 1 and 3 times the cathode radius. As electrons passes the anode, the pierce conditions are not maintained and the beam begins to diverge. By uniform current density the transverse electric field is described by

$$E_r = \frac{r}{2\epsilon_0 c}(\frac{j}{\beta}), \tag{2.6}$$

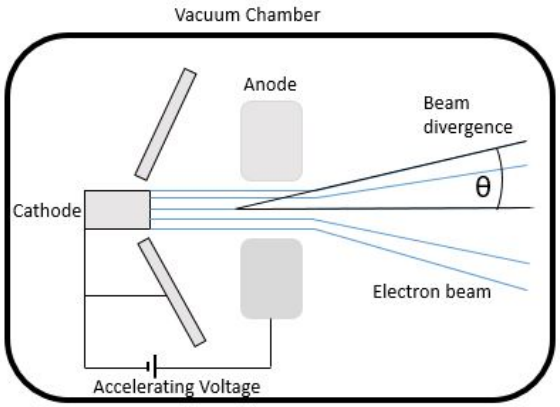

Figure 2.3: Schemata of an electron DC gun

with distance from the beam axis r and axial velocity βc. If the particles are accelerated or focused by fields (electric or magnetic) which vary linearly with displacement, the beam quality is maintained. However, some beam transport devices might induce nonlinear forces. The beam with higher kinetic energy experiences lower degradation of quality by nonlinearities. The target of conventional beam accelerating systems is to maintain the uniform beam profile until the particles have reached relativistic velocities [17].

The acceleration of electron beam extracted from the cathode is accomplished using electric fields. The field can be applied as DC (direct current) or AC (alternating current) voltage. Figure 2.4 illustrates some advantages and disadvantages of application of DC/AC fields for thermionic and photo-emitters.

The study described in this thesis concerns electron acceleration in Radio Frequency (RF) fields. Therefore the following sections are focused on basics of RF technology.

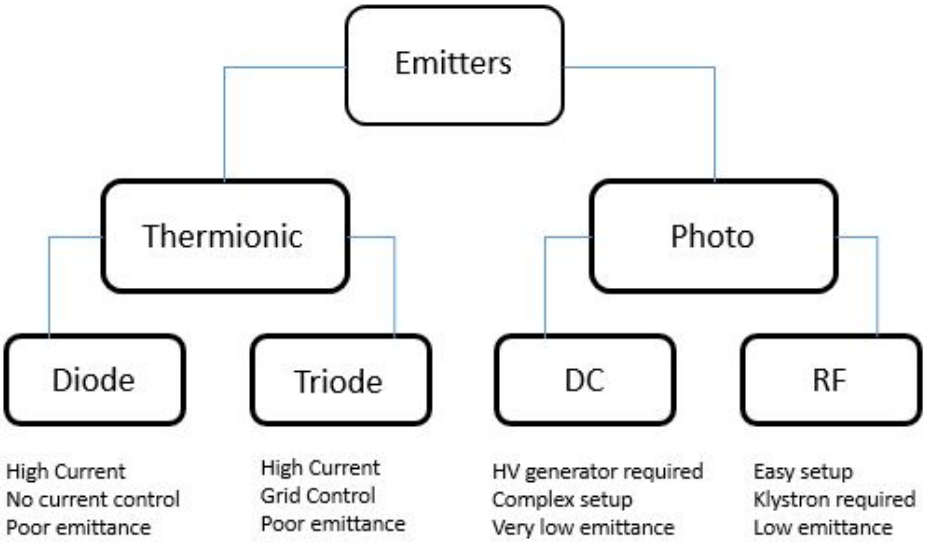

Figure 2.4: Electron emission methods.

2.3.1 RF Guns

The maximal applicable DC voltage is limited to a few hundred kilovolts. The DC gun does not accelerate the electrons to relativistic velocities. For high current the emittance grows and bunch length increases. In order to preserve cathode brightness another type of gun is required. Another concept of an electron gun was introduced by G.A. Westernikow and J.M.J. Madey in 1974. The gun uses microwave field to accelerate electrons [18]. The advantage of such radio frequency (RF) gun is:

- high accelerating gradient
- short bunch generation

The electron beam produced by RF guns has special characteristics. The beam consists of short pulses, *micropulses*, repeated at a driving frequency, *micropulse repetition rate*,

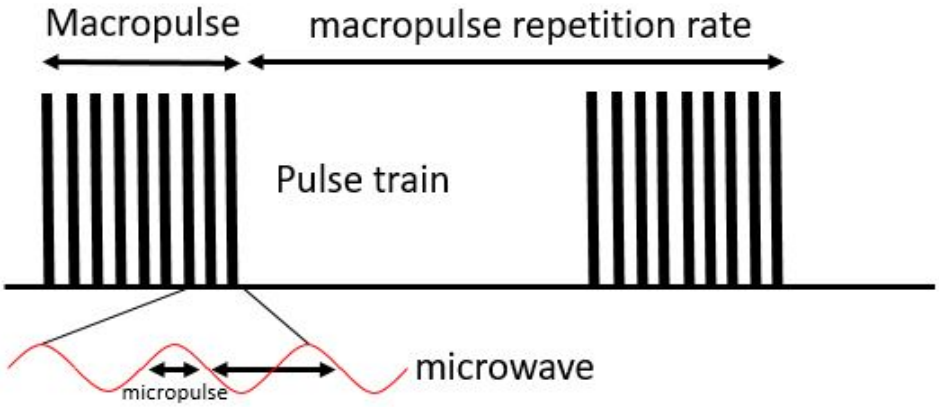

Figure 2.5: RF pulse structure.

with some timing jitter. The current in the micropulse is defined as *peak current*. The corresponding energy dispersion is called *energy spread*. The micropulses are generated in trains, called *macropulses*, repeated at *macropulse repetition rate*. An example of an RF pulse format is given in Fig. 2.5 [19].

2.3.1.1 Thermionic RF Gun

A simple RF gun is a cathode placed in a pillbox with an RF power input port and electron exit aperture. In case of thermionic RF guns the cathode material has an integrated heater to control the temperature. Thereby the mount of cathode is thermally isolated from the rest of the cavity. During RF supply electrons are accelerated in the first half of the RF period. When the RF field reverses its sign, no electrons are accelerated. Thereby the emitted electrons are grouped in *bunches*. Since the emitted electrons experience rising and falling field gradient of the half RF period, the electrons have wide energy spread and long bunch duration.

The main disadvantages of the thermionic RF gun are [19]:

- Electrons emitted in the late phase of accelerating RF period do not reach the aperture of the cavity before the field reverses. These electrons are accelerated back into the cathode. This effect is called *Back-Bombardment Effect (BBE)*, which will be explained in detail in the $3rd$ chapter of this thesis.

- The long bunch duration and wide energy spread require additional bunching systems leading to the growth of beam emittance

- The peak current depends on thermionic cathode current density.

In general the thermionic RF guns are capable to produce bright beams, but have limitations regarding high peak currents.

2.3.1.2 Photo-RF Gun

In photo-RF gun the electrons are extracted by an incident laser pulse. The cavity geometry and laser pulse phase are designed to minimize the beam emittance. By this means a high peak current within short bunch duration is created. Another important advantage of using laser pulse, is the flexibility of the electron beam pulse format, which is determined by laser pulse format. Nevertheless, the field emission in the gun might cause appearance of unwanted current, independent from laser incidents. It is so called *dark current.*

The efficiency of the photo-RF gun is described by a quantity called *Quantum Efficiency* (QE). The QE represents the ratio of electrons emitted by photocathode to the number of incident photons. In not space-charge limited case the QE is given by

$$QE = \frac{Ihc}{\lambda eP} \times 100\%, \tag{2.7}$$

(a) Thermionic RF gun **(b)** Photo-RF gun

Figure 2.6: Schematic cross section of a thermionic and photocathode RF guns.

where, λ is the laser wavelength in (nm), h is the Plank's constant $(6.626 \times 10^{-34} Js)$, e is the elementary charge $(1.6 \times 10^{-19} C)$ and c is the speed of light $(2.998 \times 10^{8} ms^{-1})$. The QE is strongly dependent on material. The photocathodes can be categorized in three main groups. These are: (1) the metal and metal compound materials, (2) semiconductors and (3) some thermionic materials. Metallic cathodes are robust, have high tolerance against vacuum poisoning and long lifetime respectively. The disadvantage of metallic materials is the low QE. The semiconductor materials have high QE, but short lifetime and are sensitive to vacuum conditions. Thermionic cathodes have higher QE than metallic cathodes, but lower than semiconductors. Some properties of photocathodes are given in appendix.

The RF cavity for thermionic and photo-RF guns is illustrated in Fig. 2.6. This work does not include the operation of field emission cathodes, thus the description of the field emission RF guns is omitted.

2.4 RF Cavity

An RF cavity is a type of resonator that can store electromagnetic fields in the RF range. The RF waves form a standing wave in the cavity at resonance frequency. A microwave cavity behaves similarly to a resonant electric circuit with low energy loss at its resonant frequency.

2.4.1 RF Equivalent Circuit

The resonant mode in the cavity can be represented by an RLC circuit. The RF fields induce surface currents in cavity walls leading to energy dissipation. The stored electric energy is represented by capacitance C and magnetic energy by inductance L. The resistance R_s is defined through power dissipation in the cavity walls. The parameters C, L, R are included in the complex cavity impedance Z_C. The excitation by external power source like klystron, is represented by current source I_g. The klystron is connected to the cavity through a transmission line. All the transmission losses are represented by the factor Z_{ext}. An equivalent RLC circuit is illustrated in the Fig.2.7a. According to Kirchhoff's rules the RLC differential equation for a parallel circuit is expressed as:

$$I(t) = \frac{1}{L}\int V(t)dt + C\dot{V}(t) + \frac{V(t)}{R} \tag{2.8}$$

$$\frac{\dot{I}(t)}{C} = \frac{V(t)}{LC} + \ddot{V}(t) + \frac{\dot{V}(t)}{RC} \tag{2.9}$$

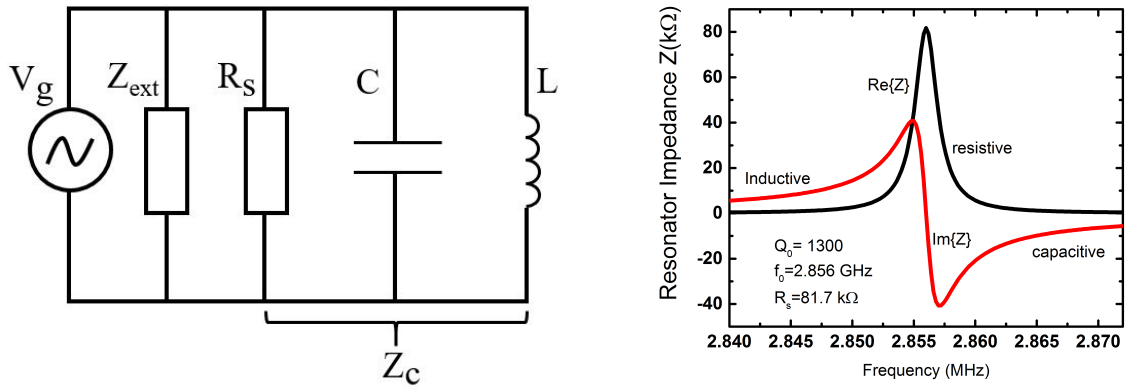

(a) RLC circuit. **(b)** Cavity impedance Z_c.

Figure 2.7: Equivalent RLC circuit and the complex Z_C.

2.4.1.1 Cavity Parameters

The RF power excites the cavity generating a harmonic voltage $V(t) = V_0 e^{(j\omega t)}$. The total cavity impedance at the generator is expressed as:

$$Z_c = \frac{V_0 e^{(j\omega t)}}{I_0 e^{(\omega t)}} = (\frac{1}{R_s} + \frac{1}{j\omega L} + j\omega C)^{-1}. \tag{2.10}$$

The complex input power is

$$P_{in} = \frac{1}{2} V I^* = \frac{1}{2} Z_c \mid I \mid^2 . \tag{2.11}$$

The RF power dissipated in cavity walls is

$$P_d = \frac{1}{2} \frac{\mid V \mid^2}{R_s}. \tag{2.12}$$

The energy stored in the cavity is

$$W = \frac{1}{2} \mid V \mid^2 C. \tag{2.13}$$

The resonant mode is characterized by a *quality factor* Q and resonance frequency ω_0. The quality factor is defined as:

$$Q = \frac{2\pi(\textit{energy stored in the cavity})}{(\textit{energy lost in a cycle})} = \frac{2\pi W}{TP_d} = \omega_0 \frac{W}{P_d}. \tag{2.14}$$

Using definition of stored energy W and dissipated power P_d, the quality factor Q is expressed as:

$$Q = \omega_0 \frac{W}{P_d} = \omega_0 R_s C = \frac{R_s}{\omega_0 L}, \tag{2.15}$$

with resonance frequency $\omega_0 = \sqrt{\frac{1}{LC}}$. The Z_c is related to the quality factor as

$$Z_c = \frac{R_s}{1 + jQ(\frac{\omega}{\omega_0} - \frac{\omega_0}{\omega})}. \tag{2.16}$$

At the resonance $\omega = \omega_0$ the Z_c becomes real $Z_c = R_s$. Figure 2.7b shows the real and imaginary part of the complex cavity impedance Z_c.

2.4.1.2 Accelerating Gradient

The energy gain of a charged particle traveling across the cavity length L_{cav} is called accelerating voltage V_a:

$$V_a = |\frac{1}{e} \times \textit{ energy gain during passage through cavity}| = |\int_0^{L_{cav}} E_z(z) e^{i\omega_0 z/\beta c} dz| \tag{2.17}$$

where ω_0 is operating frequency of RF cavity. And the averaged accelerating field $E_{acc} = \frac{V_a}{L_{cav}}$.

2.4.1.3 Shunt Impedance

Shunt impedance measures the effectiveness of accelerating voltage V_a for a given P_d.

$$R_s = \frac{V_a^2}{P_d}. \tag{2.18}$$

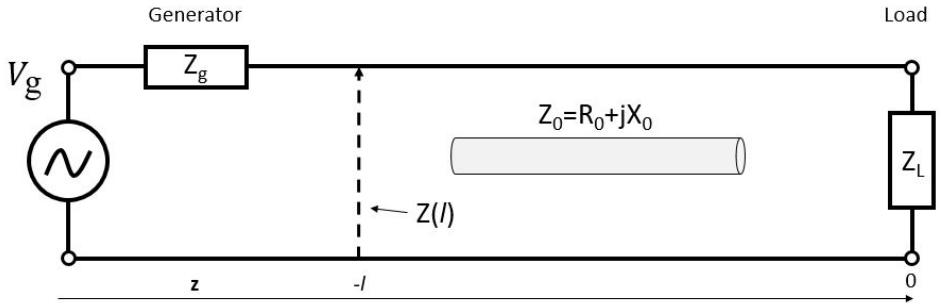

Figure 2.8: Transmission line circuit with a load impedance Z_L and generator voltage V_g .

2.4.1.4 R/Q

The efficiency of accelerating per unit stored energy is given by R over Q value. The R/Q is a function of cavity geometry. It is defined as:

$$\frac{R_s}{Q} = \frac{V_a^2}{\omega_0 W}. \tag{2.19}$$

The R_s is determined through $R_s = Q * R/Q$ value, which is calculated by numerical simulation.

2.4.2 Power Transmission to the Cavity

RF cavity is supplied by an RF power generator. The power is transmitted to the cavity by waveguides. The power transmission is described by transmission line theory. For efficient power supply the parameters of transmission line must be properly chosen. The waveguide is represented by a complex impedance $Z_0 = R_0 + jX_0$ with real part R_0 and imaginary part jX_0.

2.4.2.1 RF Transport System

The impedance of the transmission line depends on the length of the line. The impedance is described by transmission line equation:

$$Z(l) = Z_0 \frac{Z_L + jZ_0 tan(\alpha l)}{Z_0 + jZ_L tan(\alpha l)}, \tag{2.20}$$

where $\alpha = 2\pi/\lambda$ and l is the length of transmission line.

The transmission line connected to a power absorber (e.g. RF cavity) is said to be loaded. If the impedance of the line differs from the load impedance Z_L, power reflection takes place at the point of impedance change. In order to avoid power loss due to reflection, the impedances of the generator and the load must be *matched* [20]:

$$R_L = R_g \tag{2.21}$$

$$X_L = -X_g. \tag{2.22}$$

The reflection of the power due to mismatch at the load is described by the reflection coefficient Γ_L:

$$\Gamma_L = \frac{reflected\ voltage}{incident\ voltage} = \frac{Z_L - Z_0}{Z_0 + Z_L}. \tag{2.23}$$

A coaxial cable represented in transmission line model is shown in Fig.2.8.

2.4.2.2 Power Coupling to the Cavity

The RF power from the transmission line can be coupled to the cavity by three methods:

- magnetic coupling by a loop
- electric coupling by an antenna

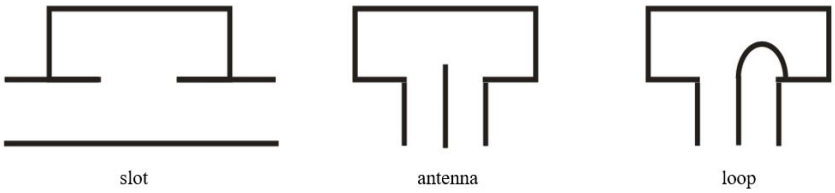

Figure 2.9: RF coupling to the cavity.

- coupling from the wavelike by a slot

The coupling methods are illustrated in the Fig.2.9.

2.4.3 RF System

A RF system consists of a power generator (usually klystron), transmission line and the cavity. Assuming lossless transmission the power loss in the RF system is determined by coupling loss in external devices P_{ext} and by dissipation in cavity walls.

. The total power loss is then $P_{tot} = P_{diss} + P_{ext}$. Correspondingly the loaded quality factor is determined as:

$$Q_L = \omega_0 \frac{W}{P_{tot}}. \tag{2.24}$$

The unloaded and loaded quality factors are related

$$\frac{1}{Q_L} = \frac{1}{Q_0} + \frac{1}{Q_{ext}}. \tag{2.25}$$

The ratio between the power lost at the coupler P_{ext} and the P_{diss} is called *Coupling Coefficient*:

$$\beta = \frac{P_{ext}}{P_{diss}} = \frac{Q_0}{Q_{ext}}. \tag{2.26}$$

There are three important coupling cases:

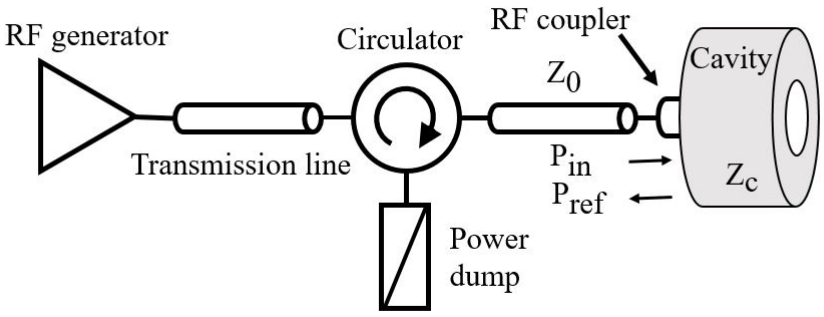

Figure 2.10: Simple RF cavity system.

- $\beta < 1$ undercoupling case
- $\beta = 1$ critical coupling
- $\beta > 1$ overcoupling

The loaded quality can be expressed through the coupling coefficient:

$$Q_L = \frac{Q_0}{1+\beta}, \tag{2.27}$$

and loaded resistance R_L respectively:

$$R_L = \frac{R_0}{1+\beta}. \tag{2.28}$$

The coupling coefficient indicates the ratio of reflected power at the cavity input port. The cavity resonance bandwidth is also given by β. If no power reflection at the coupling port occurs the line is said to be *matched*. The reflection coefficient Γ, depends on the impedance of cavity Z_c and transmission line Z_0.

$$\Gamma = \frac{Z_c - Z_0}{Z_c + Z_0} = \frac{\beta - 1}{\beta + 1}. \tag{2.29}$$

The reflected power P_{ref} is a function of input power P_{in} and Γ.

$$P_{ref} = P_{in}\Gamma^2 = (\frac{\beta - 1}{\beta + 1})^2. \tag{2.30}$$

The power delivered into the cavity through the coupler is

$$P_c = P_{in}(1 - \Gamma^2) = P_{in}\frac{4\beta}{(1+\beta)^2}. \tag{2.31}$$

The P_c takes maximal value for $\beta = 1$.

For high reflected power the power has to be coupled out and damped by an insulator as shown in Fig.2.10.

Using the loaded parameters $R_L = \frac{Q_L}{\omega_0}$ and $\omega_0^2 = \frac{1}{LC}$ the differential circuit equation can be expressed as:

$$\dot{I}(t)\frac{\omega_0 R_L}{Q_L} = \ddot{V}(t) + \frac{\omega_0 R_L}{R_L C}\dot{V}(t) + \omega_0^2 V(t). \tag{2.32}$$

2.4.4 Beam Loading

Beam loading is an effect of excitation of accelerating cavity through the electromagnetic fields generated by particle beam. Beam loading induces voltage across the cavity gap, which is opposed to the accelerating voltage. As a consequence the supplied power has to be increased and the cavity has to be properly detuned to ensure efficient power delivery. The bunch charge experiences half of its own induced voltage. This relationship is called the *Fundamental Theorem of Beam Loading* [21]. The influence of beam on cavity voltage is described by the beam admittance, which is defined as $Y_b = V_c/I_b$ with beam current I_b, and cavity voltage V_c. The beam admittance is a complex number consisting of a real part $Re(Y_b) = G_b$, called beam conductance and imaginary part $Im(Y_b) = jB_b$, called beam susceptance. The beam loaded cavity voltage is given then by:

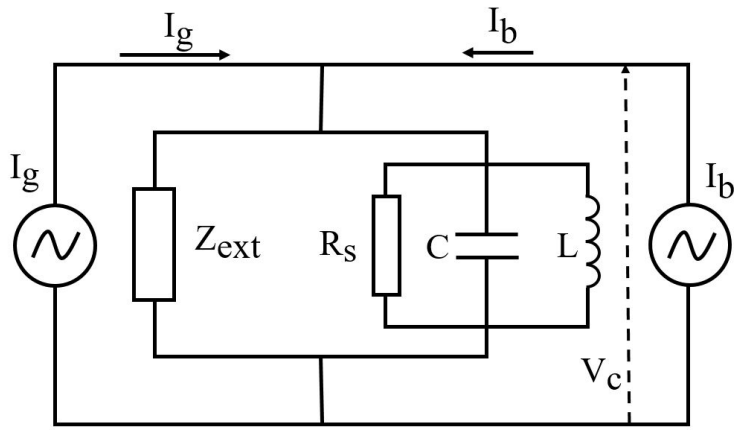

Figure 2.11: RLC circuit of RF system with beam loading.

$$V_c = \frac{I_g}{Y_c + Y_b} = \frac{I_g}{G_c + G_b + j(B_c + B_b)}. \tag{2.33}$$

The RF power generation, transmission and consumption by the cavity can be represented schematically in a diagram as shown in Fig.2.11.

2.5 Multipactoring

Accelerated particles can initiate the *Secondary Electron Emission* (SEE) by hitting the cavity walls or by ionization of residual gas molecules. The secondary emitted electrons might absorb energy from the accelerating RF fields. This process is called *Electron Load*. The electron load can limit the field amplitude and result in x-ray radiation.
The SSE is attributed to the three main processes:

1. Multipactoring

2. Field Emission

3. RF Electric Breakdown

The multipactoring is a resonant process of particle motion in an oscillating field. The process is illustrated in Fig.2.12. The primary electron emitted from the surface at $x = 0$ travels to the opposite plate at $x = x_0$ during the one-half RF period. If the kinetic energy of the primary electron is high enough it can knock out secondary electrons from the plate. The secondary electrons may return to the first plate since the field is reversed and knock out further electrons. This process can continue until the avalanche is limited by space-charge effect (see Fig.2.12a.). Multipactoring occurs when following conditions are fulfilled [21].

- travel time between the plates correspond to the integer number of half periods of AC voltage
- secondary electron coefficient must be greater than unity $\delta > 1$ (kinetic energy of primary electron must be high enough to knock out further electrons)

The maximum electric field for multipactoring is given by

$$E_{max} = \frac{V_{max}}{x_0} = \frac{m_e \omega^2 x_0}{2e}, \tag{2.34}$$

where e is elementary charge and m_e is electron mass.

In summary some important characteristics of multipactoring are given here [21]:

- Multipactoring occurs at low electric fields when raising the cavity voltage to operating level.

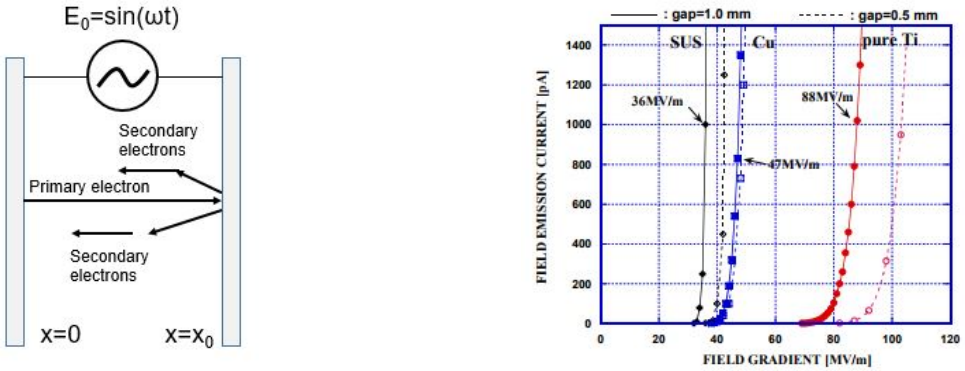

(a) Multipactoring **(b)** Dark Current [22]

Figure 2.12: Multipactoring (a) and dark current emission from SUS, Cu, Ti (b).

- Overcoupling condition reduces the filling time constant and accelerates the field build up. This condition assist to overcome the multipactoring region before resonant conditions are reached.
- Low vacuum pressure and clean surfaces can suppress multipactoring.
- Operation at multipactoring conditions at relatively high power levels (RF conditioning) can help to reduce secondary emission coefficient.
- Surface coatings can reduce secondary electron emission.
- Symmetric geometry enhances the multipactoring, since electrons from the large area are involved.

The field emission is an electron emission from the bulk material into vacuum induced by strong electric DC field. Figure 2.12b shows the field gradient at which field emission occurs for different materials. The field emission depends strongly on the surface conditions. It is considered as a primary source of vacuum breakdown. The electric breakdown

is a current flow through the insulator (e.g. vacuum).

2.6 FEL Beam Requirement

The target of this work is the improvement of a thermionic RF gun for application in MIR-FEL. The FEL facilities require high brightness electron beams with very short micropulses. It is reasonable to give some overview about FEL beam requirements. Table 2.2 summarizes the beam requirements for FEL [19].

Table 2.2: FEL beam requirements [19]

	IR	Visible	XUV	X-Ray
Wavelength (μm)	1-500	0.1-1	0.01-0.1	$<$0.01
Energy (MeV)	10-100	100-200	200-500	$>$500
Micropulse length (ps)	1-20	1-20	1-20	1-20
Micro repetition rate (MHz)	10-100	10-100	10-100	10-100
Peak current (A)	$>$20	$>$50	$>$100	$>$200
Norm. emittance (π mm $mrad$)	60-500	20-60	3-20	$<$3
Energy spread (%)	$<$0.5	$<$0.2	$<$0.1	$<$0.1
Macropulse length (μs)	$>$10	$>$10	$>$10	$>$10

2.7 Summary

In this chapter the basic knowledge of RF acceleration technology was introduced. In particular the characteristics of an RF electron gun. Some mechanisms of electron load,

which limit the applicable RF field were also mentioned.
The multipactoring, which was introduced in last sections of this chapter, is an important process, which occurs at low cavity voltage. This process and the issue of power line matching will be mentioned in further chapters and should be understood well.
The next chapter describes a major problem of the thermionic RF guns, namely the Back-Bombarding Effect (BBE). Since the study of this thesis aims to overcome the BBE, next chapter provides an overview over conventional methods for reduction of the BBE.

Chapter 3

Electron Back-Bombardment Mitigation

3.1 Motivation

Thermionic RF guns have advantage over photocathode RF guns in the compact structure, higher repetition rate and simplicity of operation. The main drawback of thermionic RF gun is the impact of back-bombarding electrons. Technical solution of this problem would allow us to reduce the costs and dimensions for electron injectors. In this chapter a short overview over methods for reduction of the Back-Bombardment Effect (BBE) for thermionic RF guns is presented. Examples of technical realization with discussion of merits are also given.

3.2 Introduction

Free Electron Laser (FEL) facilities require electron beam sources with high peak current and low emittance [23]. The radio frequency (RF) electron guns have advances against DC guns due to higher achievable accelerating fields. There are two main types of RF electron guns used as injectors for FEL. Depending on the process of electron generation the electron RF guns are divided in thermionic and photocathode RF guns. In thermionic RF guns the cathode is heated and electrons are emitted continuously and accelerated then during the half RF period. Thereby a long electron beam pulse with wide energy spread is obtained. This problem is avoided in photocathodes, where a laser pulse is used to extract the electrons from cathode material. Short laser pulses generate short electron bunches with higher current densities. However, the performance of photocathodes is limited by the availability of high average power lasers. In order to build a compact injector and to avoid high costs for laser systems, technological development of electron emission control in thermionic RF guns is required. The following overview over methods to counteract the main drawback of thermionic RF gun shall motivate further investigations in this field.

3.3 Back-Bombardment Effect

In thermionic RF guns an alternating electric field is used to accelerate the electrons [23]. The electrons emitted in the late RF phase might not leave the gun cavity before the field reverses. The reversed field accelerate electrons back to the cathode. As a consequence the back accelerated electrons hit the cathode. This phenomena is called the Back-Bombardment Effect (BBE) [24]. Figure 3.1 shows the schema of the BBE. The impact of the BBE on RF gun can be divided in 3 processes [4]:

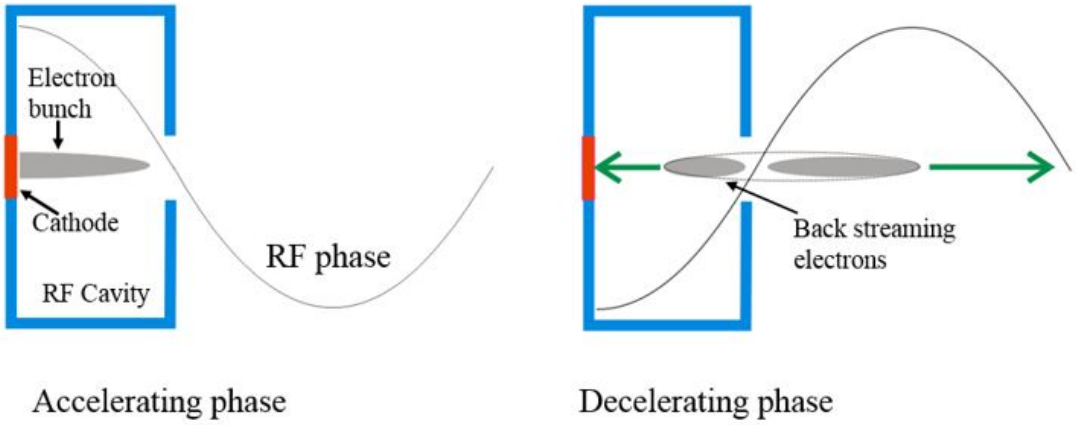

Figure 3.1: Schematic Illustration of the Back-Bombardment Effect (BBE).

- Cathode heating
- Emission current increase
- Beam energy degradation

Due to the incidence on cathode the back-streaming electrons deposit their kinetic energy into the cathode material. As the consequence the cathode temperature is increased, which leads to the rise of emission current. The micropulse heating dT does not significantly change the cathode temperature, but the average heating over the macropulse ΔT rises the current from the set temperature T_i to the higher one T_e. The cathode heating during the macropulse is illustrated in the Fig.3.2.

.

The cavity voltage decreases by rising current due to the beam loading effect [21]. Subsequently the beam energy decreases.

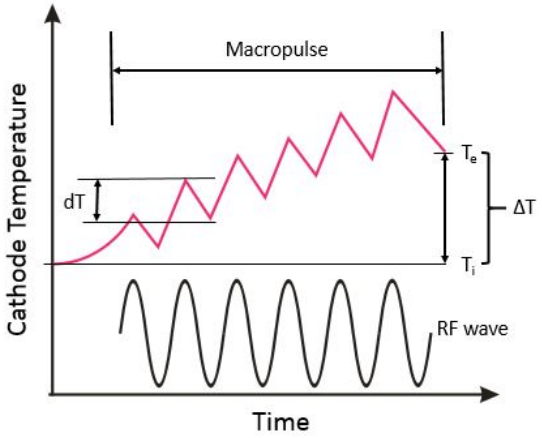

Figure 3.2: Averaged cathode temperature increase due to the BBE.

The appearance of BBE can be identified by the ramp in current in the macropulse. The Figure 3.3a shows an example of an RF macropulse with the current ramping due to the BBE, measured at Kyoto University Free Electron Laser (KU-FEL). The corresponded beam energy degrades for about 10% within 4μ is as shown in Fig. 3.3b [4].

The transient increase in the cathode temperature owing to the BBE was verified experimentally by the group from University of Hawaii. The group has measured the temperature increase of $13.8K/\mu s$ over the $5\mu s$ pulse [25]. Degradation of emittance and energy spread during the macropulse of $3\mu s$ assigned to BBE, was reported in Ref.[26].

The back-streaming electrons can be classified as low and high kinetic energy particles. The electrons with low kinetic energy are accelerated back from the area close to the cathode surface. The high energetic electrons are accelerated back from further away of the cathode (including multiple cell structures). The penetration length of the material depends on kinetic energy of incident electrons. The low energetic electrons deposit their energy close to the surface and contribute at most to the heating up process [27]. In general the back-bombardment (BB) heating is increasing with higher cavity voltage and

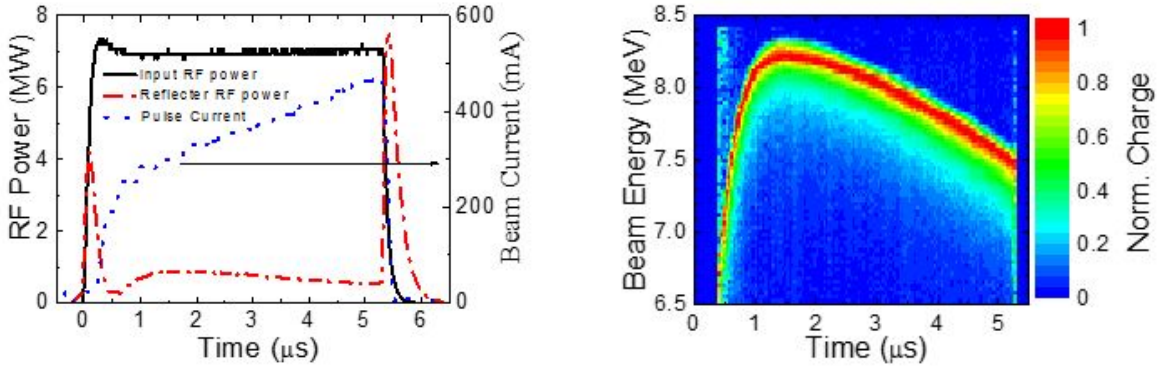

(a) RF macropulse structure

(b) Beam energy during the macropulse

Figure 3.3: Macropulse current ramping and beam energy drop due to BBE [4].

higher current.

For FEL applications a long macropulse and a high peak current with stable electron beam energy is required, especially for oscillator type FEL. Therefore it is important to reduce the BBE in the thermionic RF guns applied as FEL injectors [4].

3.4 Measures of Counteracting

As mentioned in previous section the BBE has three stages. The counteracting measures may target each of them separately or in combination, respectively. The methods for reduction of the BBE can be categorized as follows:

- Reduction of BB-heating
- Compensation for beam energy degradation
- Change in electric filed distribution

3.4.1 Reduction of BB-heating

Reduction of BBE heating can be accomplished by redirection of back-streaming electrons such that the amount of incident electrons on the cathode surface is reduced. Another way is to compensate heating on cathode by external temperature control. This section introduces common technical realizations for control of cathode temperature.

3.4.1.1 Magnetic Deflection

The back-streaming electrons with lower energy are deflected by a transverse magnetic field [24, 6],[25]-[30]. Figure 3.4a shows the principle of electron deflection by a magnetic field. Therefore installation of an external dipole magnet in vicinity of cathode is required. By this method the current pulse length of Mark III RF gun was extended from $1.4\mu m$ to $6\mu m$ using the deflecting field of $60G$ [6].
The magnetic field acts also on forward accelerated electrons, which sets limitation on applicable magnetic strength. A beam trajectory correction system would be required at the gun exit. For this reason magnetic deflection is suitable for low energetic BB electrons only. An-other impact is that the magnetic field in the gun increases slightly the emittance [28].

3.4.1.2 Hollow Cathode

From the point of view of axial symmetry in accelerating fields the high-energy BB electrons impact mostly around the centre of the circular cathode. The hollow shape allows reduction of the thermal impact from the central cathode region to the whole cathode [27]. Some authors refer to hollow cathode as *ring cathode* [29].

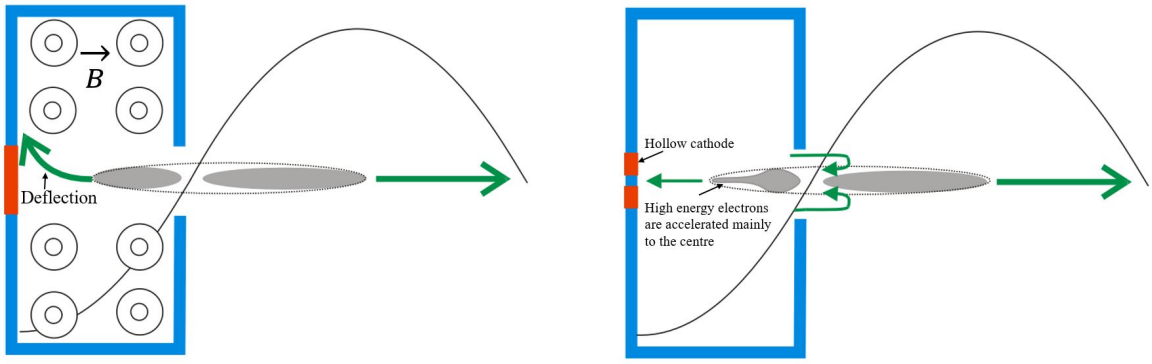

(a) Magnetic deflection **(b)** Ring cathode

Figure 3.4: Magnetic deflection and hollow cathode application.

The principle of BB electron damping in the hollow cathode center is illustrated in the Fig.3.4b. However, a test of a hollow cathode showed degradation of transverse emittance, since the electrons with smaller emittance are coming from the central part of circular cathode [29]. Another disadvantage is the current limitation due to the reduced cathode surface (hollow shape).

3.4.1.3 External Heating/Cooling

In order to control electron current the cathode temperature during the macropulse must be kept constant. Cathode heating adjustment by a joule heater (ms range) is not fast enough to compensate macropulse transient heating (μs range) caused by BB electrons. One way to accomplish fast temperature adjustment is to use a laser pre-pulse [29, 31].

The laser pulse irradiation set before RF macropulse allows fast heating up the cathode. After pulsed heating the cathode surface is cooled down by diffusive heat transfer into the cathode bulk material. By proper adjustment of pulsed heating the diffusive cooling can

compensate for the BB heating within the macropulse. The drawback of this method is the requirement of an additional laser system, which increases costs.

A group at University of Hawaii is working on application of laser pre-heating method. Corresponding simulations show the increase of macropulse length by factor 6 ($5-30\mu s$). However, they have faced the problem of laser peak power limitation due to plasma formation on the cathode surface [31].

Another approach is the operation of thermionic emitter at very high temperature ($2400K$). High operating temperature decreases the temperature variation due to BBE. This technique requires cathode materials with high melting point. For this reasons a special prototype thermionic RF gun with electron beam heating of tantalum emitter was developed at the NSC KIPT, Kharkiv, Ukraine [32].

3.4.1.4 Cathode Materials

The choice of cathode material is very important for thermionic cathodes. Based on atomic structure some materials have higher resistance against the back-streaming induced heating [33, 34]. The LaB_6 showed higher tolerance for BBE than dispenser cathodes. The CeB_6 was predicted to be a better choice regarding the BBE resistance than LaB_6.

3.4.2 Beam Loading Compensation

Beam loading is the change of cavity voltage induced by the fields of charged beam particles. Control of beam loading allows to compensate for beam energy degradation during the macropulse.

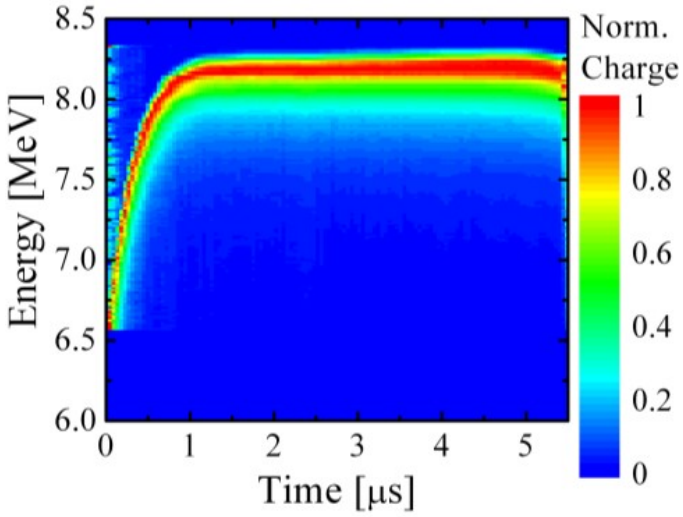

Figure 3.5: Beam energy after compensation by RF power control [4].

3.4.2.1 RF Power Control

Beam loading compensation techniques are usually based on modulation of amplitude and phase of the input RF power [35].

An example for beam loading compensation as applied to counteract the BBE in the RF gun of KU-FEL facility is the amplitude modulation of RF power [36, 37]. Thereby RF Pulse shape was modified by pre-programmed klystron gain. Figure 3.5 shows the graph of beam energy obtained by amplitude modulation at the KU-FEL RF gun [24]. The current pulse of $4\mu s$ was obtained by this method. For lasing pulse duration of $3\mu s$ was required. However, the input RF power adjustment based methods have a disadvantage of slow temporal response and complexity in technical realization.

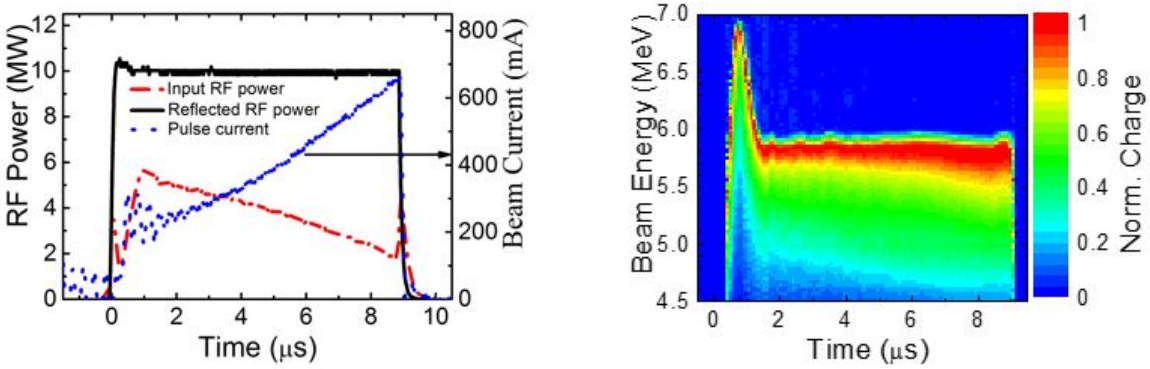

(a) Macropulse by detuned gun cavity

(b) Beam energy stabilization

Figure 3.6: Beam energy stabilization by gun cavity detuning [4].

3.4.2.2 Cavity Detuning

Another method for beam loading compensation is the so called *cavity detuning*. Hereby the gun cavity is detuned by several hundred kHz below the driving RF resonance. The method was approved on the S-band RF gun at the KU-FEL facility. The corresponding beam energy was stabilized over $7.5\mu s$ by detuning for $-590kHz$ [38]. Figure 3.6a shows corresponded results for RF macro-pulse and the Fig.3.6b for beam energy [24]. The beam energy without cavity detuning is given in Fig.3.3b. Technically the detuning was accomplished by controlled increase of the RF gun cavity body temperature. The simplicity in realization is a significant advantage of this method.

In general beam energy compensation based methods require reduction of operational power.

3.4.3 Electron Emission Control

The timing of electron injection into the accelerating RF phase and the kinetic energy of electrons, can be modified by special geometrical design of the RF gun body. The gun body design might be based on a simple one-cell structure or more complex multi-cell structure for case specific needs.

3.4.3.1 Gridded RF Gun

The usage of DC biased grid is a technique usually applied in electronics for triodes [39]. The voltage introduced to the grid located in front of cathode is used to control the beam current and pulse shape. Thereby the electron injection into the RF fields takes place under the condition:

$$-U_{bias} + \alpha U_a \sin \omega t > \theta \tag{3.1}$$

where α is the grid penetration factor, U_{bias} is biased voltage on grid and U_a is the anode voltage amplitude [40]. A schematic drawing of a gridded RF gun is given in the Fig.3.7. The electrons pass the grid mesh when the electric field beside cathode is larger than zero. The electron injection takes place during the time period θ.

Some examples of gridded thermionic RF guns used in FEL facilities are the Novosibirsk THz FEL [41] and the FEL at Fritz Harber Institute (FHI) in Berlin [42]. Disadvantages of application of grid mesh is the increase in transverse emittance [43] and the limitation in microbunch repetition rate [44].

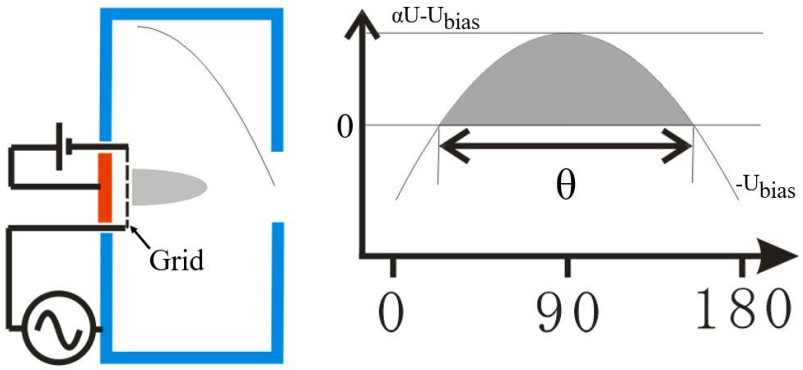

Figure 3.7: Gridded RF gun.

3.4.3.2 Two-Mode Cavity

The authors in Ref.[45] have proposed an interesting method for electron emission control for a RF gun. The method is based on combination of a pillbox type RF cavity and a subsequent cylindrical coaxial resonance system. The mechanical variation of the length of cylindrical cavity for $l = n\lambda_0/4$ allows varying the electric field distribution of the cavity (change between π and 0 modes). A similar approach targeting reduction of BBE was described in [46]. The authors describe a cavity, which is simultaneously driven by a fundamental and an harmonic RF waves. The two modes ($TM010$ and $TM020$) are overlayed in a special designed cavity geometry (one cell) for bunching the electron beam.

Figure 3.8a shows the principle of two mode superposition. The graph is divided in three zones corresponding to conditional BBE stages. The stage I represents extraction and acceleration of electrons. The stage II indicates reversing field and back-acceleration of electrons. The stage III has no electron extraction from the cathode. The superposition with $1st$ harmonic field allows enlarging the stage I for forwards accelerated electrons and

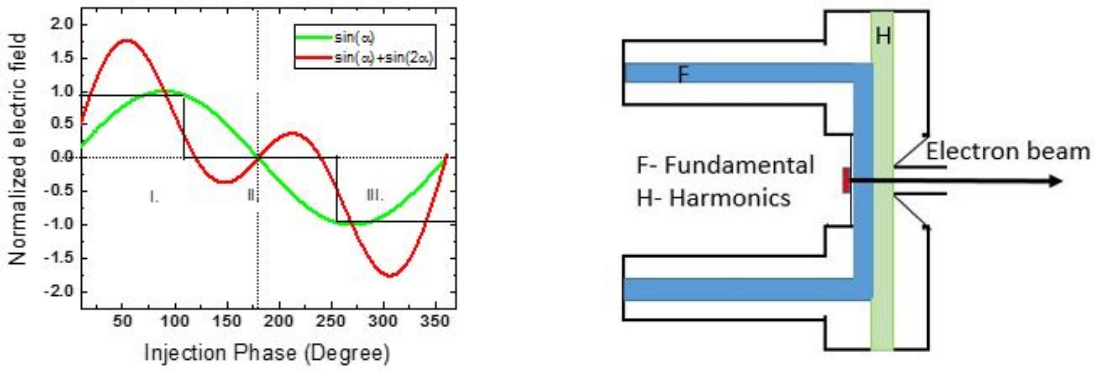

(a) Fundamental and harmonic superposition **(b)** Gun cross-section

Figure 3.8: Two-frequency cavity.

reduces the amount of back-accelerated electrons respectively [47].

Design and beam dynamic calculation of the two-frequency RF gun is described in Ref.[47]. The Figure 3.8b shows the cross-section of the two frequency gun body. The corresponding simulations have shown that such a configuration can reduce the BBE for 60%.

3.4.3.3 Back-Bombardment-less RF Gun

Another approach was proposed by K. Kanno and E. Tanabe as a *Back-bombarding less RF electron gun* [48]. In contrary to gridded RF gun this design uses an additional quarter wave RF cavity for pre-bunching. The pre-bunching cavity has a separate RF power supply. By this means the injection phase of electrons into the main gun cavity can be controlled. Figure 3.9 shows a schematic model of the *Back-bombardment-less RF gun*. Simulations have shown complete elimination of BBE [48].

The main advantage of such a design is its compactness and capability for adaptation to conventional RF cavities. An example of technical realization of quarter wavelength

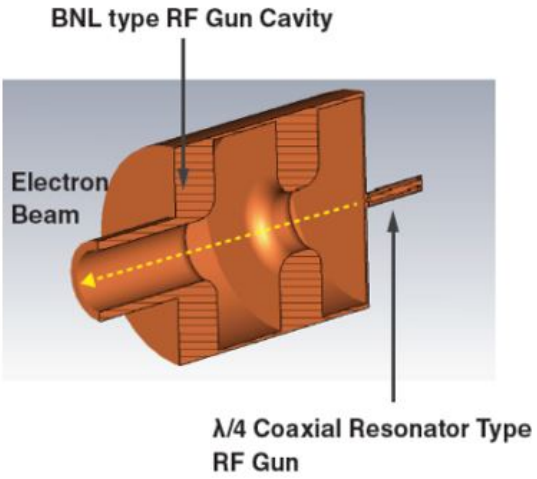

Figure 3.9: Schematic view on back-bombardment less RF gun [49].

pre-bunching cavity is the triode-type thermionic RF gun at KU-FEL. This gun will be described the chapter 6 in this in details. However, the cavity is suffering from multi-pactoring due to its small dimensions [50] (see chapter 5).

3.4.4 Complex Structures

Further examples to be mentioned in this chapter, refer to rather complex structured RF gun cavities. Besides of BBE mitigation, complex cavity designs are usually targeting several goals. These are mostly the low emittance, narrow energy spread, and the high charge per bunch. The change in cavity structure for BBE mitigation concerns reduction of the gap distance of the first cavity cell. However, small cavity dimensions decreases the RF breakdown limit.

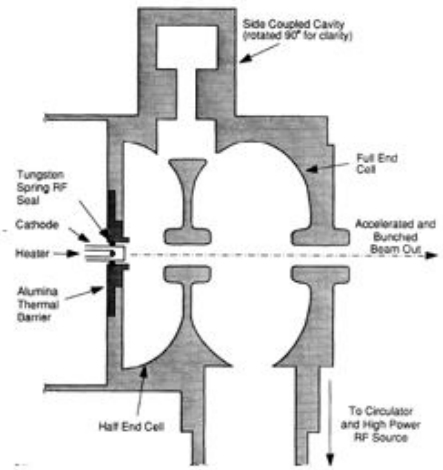

Figure 3.10: Cross-section of 1-1/2 cell side coupling standing wave RF gun [52].

3.4.4.1 1-1/2 Cell RF Gun

A $1-1/2$-cell side coupling standing wave thermionic RF gun was developed at Stanford Synchrotron Radiation Laboratory (SSRL). Owing to the first half-cell structure the electrons gain most of the energy in the second (full) cell. By this means the energy of back-bombardment power is kept at low level [51]. The cross-section of the gun is shown in Fig.3.10.

3.4.4.2 Beijing Free Electron Laser (BFEL) RF Gun

The on-axis field distribution in the RF gun cavity that would allow to reduce the back-bombarding power and provide suitable energy and phase spectra of electrons can be established in a cavity with multi-cell structure [53]. In particular the reduced length of the first cell in a multi-cell structure, can shorten the electron bunch duration.
The multi-cell structure has an advantage of maintaining the low beam emittance due to

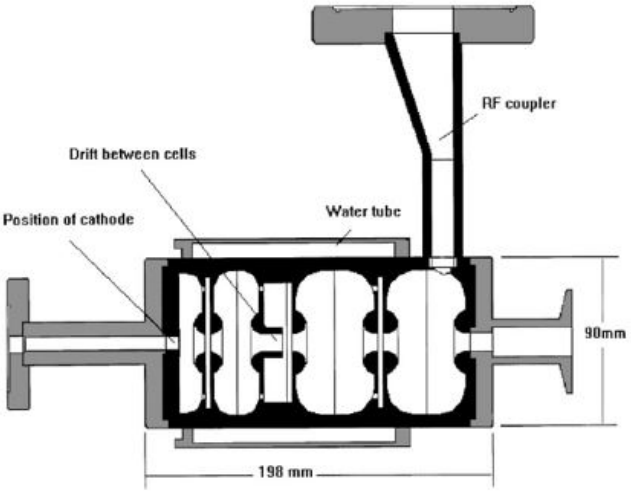

Figure 3.11: Cross-section of the BFEL electron Gun [54].

fast acceleration to relativistic velocities. Such a gun was applied in Beijing Free Electron Laser (BFEL) facility. The cross-section of the gun is shown in the Fig.3.11. The first cell is about 1/3 of length of the full cell. Such design allows reducing the amount and power of back-streaming electrons. Corresponded suppression of BBE was already reported [54].

3.4.4.3 On-axis Coupling Structure (OCR) RF Gun

Another example of a multi-cell RF gun structure is the On-axis Coupling Structure (OCS). This gun uses standing wave in $\pi/2$ mode for electron gun acceleration [55]. Figure 3.12 shows the cross-section of the OCR gun. Besides of reduction of BBE this structure offers higher group velocity and lower emittance over the commonly used structures. The gun has large aperture, which is intended for application of deflecting magnet with high field. The design of the gun allows the application as thermionic RF gun or as photocathode RF gun, which gives another advantage of this structure. The FEL-SUT

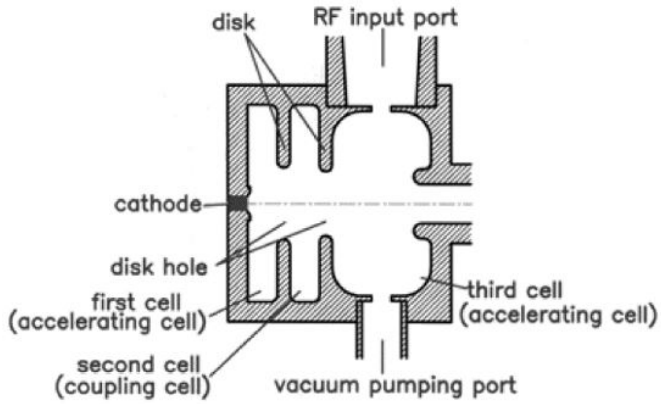

Figure 3.12: Cross-section of the OCR gun [56].

facility at the Research Center of Science University of Tokyo is applying the OCS RF Gun as electron source.

3.4.4.4 Independently-Tuned Cells (ITC) RF Gun

Another remarkable gun structure is the Independently-Tuned cells, the ITC-RF gun. The gun consists of two cavities which have independent RF power supplies. Such design allows ballistic bunch compression (BBC) of electron bunches by varying the ratio of field amplitude of different cavities [57].

An ITC-RF gun was been developed at Tohoku University, Japan, in the Group of Prof. Hama [58]. The schematic cross-section of the ITC-RF gun is shown in Fig.3.13. The design was developed for bunching of electron beam to short pulses with high peak currents. The BBE mitigation was not the dominant target for that gun and the impact of BBE remains still an issue to be solved [59, 60].

Further development of the principle of independent cell-tuning with reference to the BBE reduction was undertaken as External Cathode ITC (EC-ITC) RF gun [61]. The innovative change thereby is the external gridded thermionic DC cathode. Such configuration is designed to ensure almost complete elimination of the BBE [62].

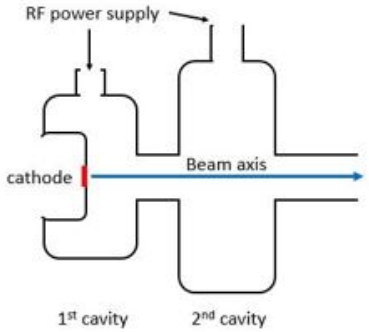

Figure 3.13: Cross-sectional schema of a ITC-RF gun.

3.4.4.5 Hybrid Structures

The methods mentioned in previous sections are frequently applied in combinations. For example pulsed DC voltage is applied for generation of electrons and the subsequent RF field is used for further beam acceleration as at the SACLA XFEL facility [63]. Another interesting hybrid structure is a gridded cathode biased with fundamental or harmonic RF fields like in FHI IR FEL facility [42], which can be extended to multi-cell structures as proposed in Ref.[44]. Another proposal is it to embed a three pole wiggler into the anode structure of a 100 MHz thermionic RF gun for deflection of BB electrons. Such a structure would allow 20-fold reduction of BB power in cost of significant rise of emittance [64].

3.5 Summary

The thermionic RF guns have an advantage in compact structure, simple operation and relative low manufacturing costs as compared to photocathode RF guns. However, the thermionic RF guns suffer from the back-bombarding effect, which limits the generation of long macropulses with stable current as required for oscillator type FEL. In this chapter were presented several methods and examples for technical realization for mitigation of the Back-Bombarding Effect (BBE).

There are simple methods, which do not require serious gun modifications. In particular magnetic deflection. The grid biased cathodes are also widely used for this reason. Most of the simple methods cause emittance degradation, since they do not specifically act on back-streaming electrons, but also on forward accelerated. In this sense the beam loading compensation is a beneficial measure. More effective suppression of BBE methods require special gun design. Especially particular structures with shortened first accelerating cells. Whereas short gaps reduce the applicable RF field due to the increase of the breakdown probability. Multi-cell structures allow to accelerate electrons to high energies and to maintain low emittance. In conclusion it should be said that there are no universal solutions for complete BBE mitigation by maintenance of the macropulse length. So, the best choice is done by combination of several techniques in each specific case.

The most FEL facilities do apply photocathode RF guns without facing the problem of BBE. This choice rises the construction and maintenance costs for the facilities. In order to make photocathode RF guns competitive regarding the costs, further development in photo-extraction technology is required.

The content of this chapter was presented at the International Conference "Synchrotron and Free electron laser Radiation: generation and application" (SFR-2018) and submitted for publication.

Chapter 4

Triode-Type Thermionic Electron RF Gun

4.1 Motivation

The Kyoto University- Free Electron Laser (KU-FEL) facility uses an S-band 4.5-cell thermionic RF gun as electron injector. Because of the multi-cell structure of the electron gun, the back-streaming electrons deposit high power into the cathode material, which causes significant temperature rise [65]. The cathode-heating due to the BBE for that RF gun has already been verified experimentally [66]. Some methods, which were applied for counteracting the Back-Bombardment Effect (BBE) at the KU-FEL facility were introduced in previous chapters [67]-[69]. Those methods are based on RF feeding control. The RF control limits the applicable voltage for the klystron and reduces the RF power available for acceleration. Another disadvantage of beam energy compensation methods is that they don't eliminate the BBE impact. The BBE itself has a positive feedback from

the cathode temperature increase. This relation doesn't allow us to operate the RF gun at any available temperature. The peak current is limited.
For improvement of charge per pulse ratio the cathode should be operated at higher temperature, hence a new method which would be capable to reduce the amount of back-streaming electrons is required.

In this chapter the concept of triode-type thermionic RF gun is introduced. The main target of the project is to modify the 4.5-cell thermionic RF gun to triode-type one. A successful modification is expected to suppress the BBE significantly and to improve the performance of the KU-FEL.

4.1.1 Introduction

The main target of this study is the proof of principles of an innovative method to control the injection of electrons into the accelerating RF phase. The method is based on a model of a "Back-Bombardment-less" RF gun, which was proposed by K. Kanno and E. Tanabe [48]. The main idea of this approach is the introduction of a quarter wavelength cavity with cathode to the main RF gun body. The cavity has separate RF power supply and RF phase control. It serves for pre-bunching of the electron beam for injection into the main gun cavity. The bunched electron pulse is injected into the accelerating RF field in an appropriate phase, before the field reverses its polarity. On this way the amount of back accelerated electrons can be reduced. In analogy with an electronic device, where the electron emission is controlled by an additional electrode, the cavity is referred to as *triode cavity*.

Figure 4.1 illustrates the principle of a Back-Bombardment-less RF gun. The main point of this method is that this concept can be potentially applied to any thermionic RF gun. Such approach was applied to the modification of the 4.5-cell RF gun.

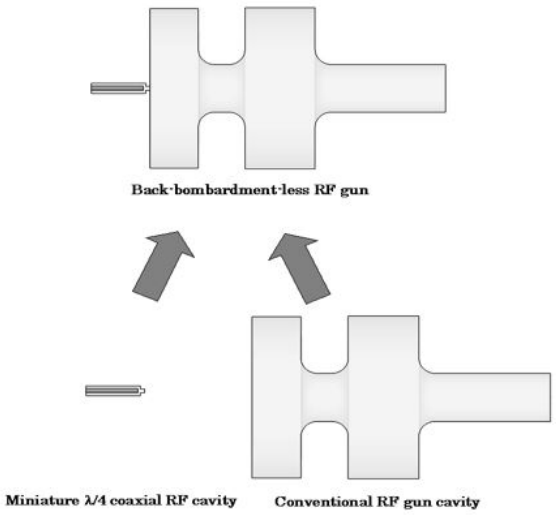

Figure 4.1: Triode concept [48].

The Figure 4.2 shows a 1-D phase plot of RF field applied in the 4.5-cell RF gun (see Fig.4.2a) and in the same RF gun with pre-bunching cavity Fig.4.2b (triode structure). The corresponded beam trajectories are also included in the graph as black lines. Red lines correspond to back-streaming electrons. From the graph 4.2b it becomes evident that the number of back-streaming electrons is significantly reduced. Comparing a conventional RF gun, the triode approach offers following advantages [48]:

- Lower longitudinal emittance
- Higher peak current of the output beam
- Reduced BB-power

The plan of the proof of principles consists of following steps: To conduct the cold (without electron emission) and hot (with electron emission) tests for confirmation of the capability of the cavity to generate the electron beam with desired parameters. In the case of success for the tests, the cavity should be introduced to the main 4.5-cell RF gun and applied

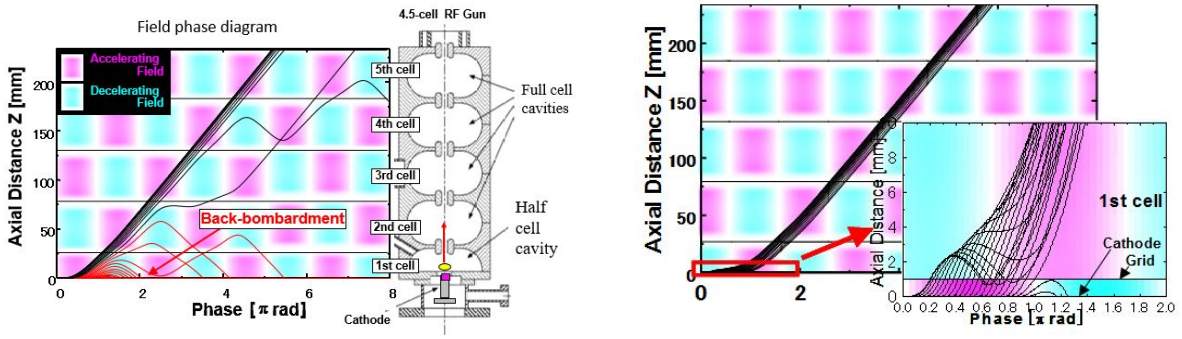

(a) BBE for 4.5 -cell RF gun

(b) BBE with pre-bunching

Figure 4.2: Simulation of BBE of 4.5-cell thermionic RF gun of KU-FEL facility. For conventional (a) and triode structure (b).

in the KU-FEL facility. The KU-FEL performance with the triode RF gun would be the final verification of the proof of principles of the triode system.

4.1.2 Background

The cavity design with corresponding beam dynamics calculation was done in previous studies [70]-[74]. The new in the chosen design is the usage of a cut off aperture instead of conventional grid electrodes. This thesis describes the development and testing (cold and hot test) of a quarter wavelength cavity for 4.5-cell thermionic RF gun.

4.2 Triode-Type Thermionic RF Gun

The triode RF gun structure is a modification of the existing 4.5-cell thermionic RF gun currently being used in the KU-FEL facility, for mitigating the impact of BBE. Therefore an additional quarter wavelength coaxial cavity was developed as a pre-bunching

cavity. The design of the vacuum chamber is intended to be attached to the main 4.5-cell accelerating cavity [70]. The schematic view of triode-type 4.5-cell thermionic RF gun is shown in the Fig.4.3. The triode cavity structure was designed to ensure the compactness and wide frequency acceptance [71]. Corresponding numerical simulation predicts for such triode structure to have more than 80% reduction in the power of back-streaming electrons [72].

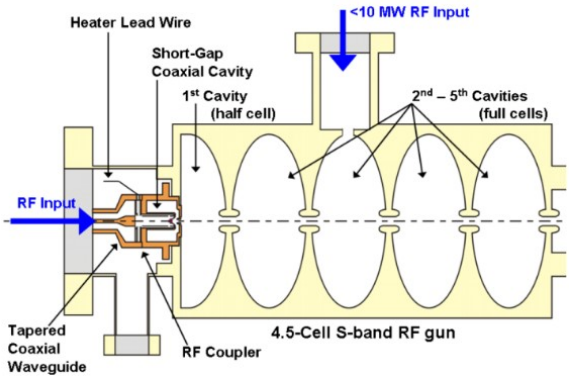

Figure 4.3: Triode-type structure of back bombardment less 4.5-cell thermionic RF gun [73].

4.2.1 Triode Cavity Design

In order to keep the triode structure compact a special longitudinal power coupler with coaxial wave guide for the triode cavity was designed and fabricated [74]. The RF power is fed to the coaxial wave guide through a coaxial window ($N50$ connector on $CF16$ vacuum flange). The triode cavity made from oxygen-free copper has a Wehnelt structure for the optimization of the electron beam trajectory to achieve low transverse emittance [70, 71]. Figure 4.4 shows the schematic structure of the triode cavity. The electron-emitting cathode material with a joule heater is embedded into a molybdenum plug (indicated by

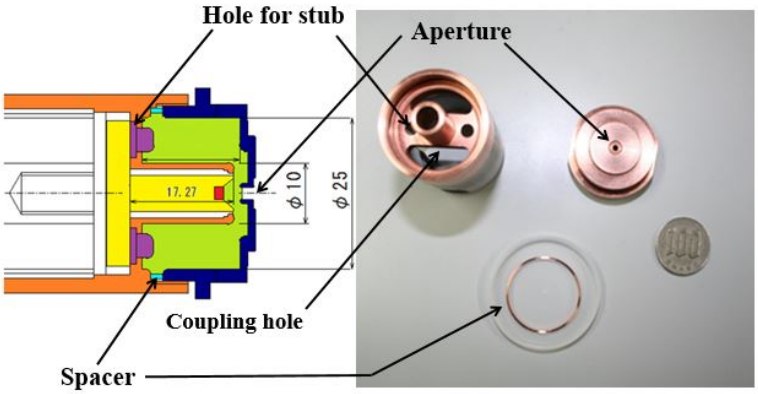

Figure 4.4: Quarter-wavelength triode cavity design [73].

a yellow color in the figure). The plug doesn't come into contact with the inner cavity core in the cathode material area. A tungsten spring is used to prevent the RF from penetrating the free space between the plug and inner cavity core. The cylindrical cavity

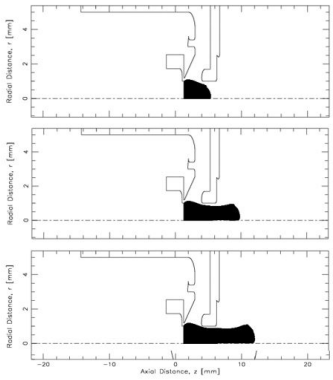

(a) Beam trajectory snapshots

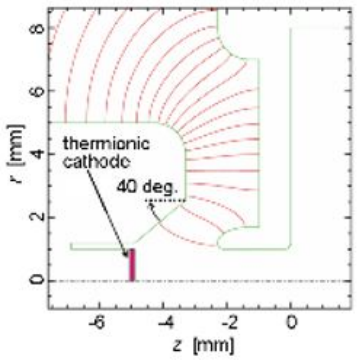

(b) Wehnelt structure of cathode

Figure 4.5: Cavity design.

is made from two separable parts. This design allows opening the cavity for controlling the position of the plug. A copper gasket is applied as a spacer between the two parts. Gasket thickness is selected according to the resonance frequency. The resonance frequency of the triode cavity can be adjusted by the insertion of stubs (indicated by purple color in

Figure 4.6: Triode device consisting of a quarter-wave cavity with longitudinal power coupler.

the figure) with proper length [75].

Figure 4.5 shows the Wehnelt structure (Fig.4.5b) of the cathode and snapshots of beam trajectory calculation (Fig.4.5a) for the current density $J = 80A/cm^2$ and cavity voltage $V_c = 30kV$. The drift length and the aperture size of the cavity are adjusted to reduce the space charge effect and minimize particle loss. The fabricated *triode device* (cavity and longitudinal power coupling waveguide) is shown in Fig.4.6.

4.2.2 Triode-Type Thermionic RF Gun Setup

The main 4.5-cell RF gun body is supplied directly by a $10MW$ klystron (Thomson TV2019B6). The triode cavity in triode RF gun configuration is supplied by the same klystron through a wave guide-type $20dB$ directional coupler as shown in Fig.4.7. The triode power line has an additional phase shifter and a variable attenuator. These are required to match the optimal condition for the pre-bunching of the electron beam prior to its injection to the main accelerating cavities (4.5-cells). The input and reflected power are measured using a $40dB$ bidirectional coupler. The insulator device (circulator with

a power dump) ensures that the power reflected from the cavity coupler is dumped and does not interfere with the input power from klystron.

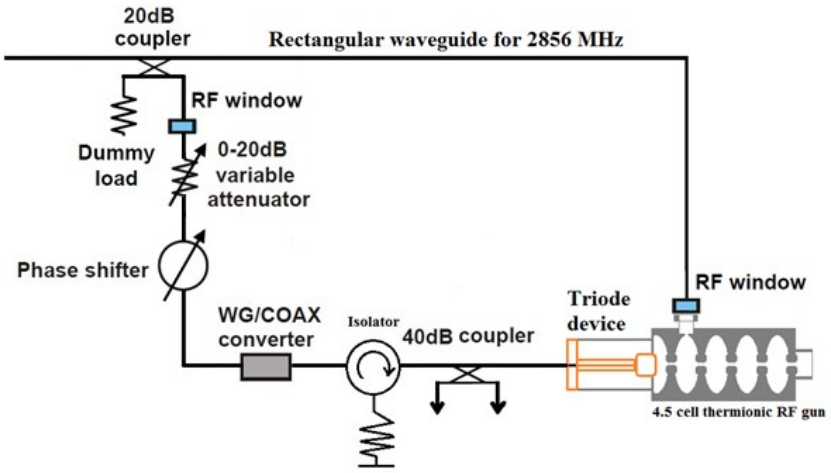

Figure 4.7: Klystron power junction for triode RF gun configuration [73].

4.2.3 Equivalent Circuit

Resonance curves of the triode cavity are calculated according to the equivalent circuit model as presented in Fig.4.8 [76]. The model consists of three components: (1) the RF source, (2) the resonant cavity and (3) the electron load. It is convenient to describe the components using complex admittance $Y = G + jB$, with real conductance G and imaginary susceptance jB. The power source is represented by an external load $G_{ex} = \beta G_c$ and by the current $I_g = \sqrt{(8G_{ex}P_{in})}$. The β denotes the coupling constant and P_{in}, the input power. The resonant circuit constants, namely the capacitance C_c, the inductance L_c, and the conductance G_c are determined by cavity parameters, namely the cavity

resonance frequency f_0, the R/Q factor and the unloaded quality factor Q_0.

$$C_c = \frac{1}{2\pi f_0(R/Q)},\ L_c = \frac{R/Q}{(2\pi f_0)},\ G_c = \frac{1}{Q_0(R/Q)}. \tag{4.1}$$

The cavity voltage V_c is described by:

$$V_c = \frac{I_g}{(G_c + G_b + G_{ex})^2 + (B_c + B_b)^2}. \tag{4.2}$$

The cavity voltage is related to the power consumed by the cavity P_c as:

$$P_c = Re[\frac{1}{2}(V_c^* I_g - G_{ex} V_c^* V_c)] \tag{4.3}$$

According to this model the power ratio of power reflected from cavity $P_{ref} = P_{in} - P_c$ and input power P_{in} can be expressed through circuit parameters:

$$\frac{P_{ref}}{P_{in}} = 1 - 4\frac{(G_{ex} + G_b)}{((G_c + G_b + G_{ex})^2 + (B_c + B_b)^2}. \tag{4.4}$$

The influence of beam loading effect is described by an admittance Y_b, which is defined as $Y_b = I_b/V_c$ with beam current I_b. The beam admittance is a complex number $Y_b = G_b + jB_b$ and depends on the energy transferred to electron beam during the acceleration. The factor $j(B_c + B_b)$ is the imaginary part of the beam loaded cavity admittance, which describes the shift in resonance frequency. The cavity susceptance jB_c denotes cavity detuning and can be expressed as:

$$B_c = \frac{1}{R/Q}(\frac{f}{f_0} - \frac{f_0}{f}). \tag{4.5}$$

For the case when there is no electron beam, the beam susceptance becomes zero ($B_b = G_b = 0$) and Eq.4.4 is simplified to

$$\frac{P_{ref}}{P_{in}} = 1 - \frac{4(G_{ex}G_c)}{(G_c + G_{ex})^2 + (B_c)^2} = 1 - \frac{4\beta}{(1+\beta)^2 + Q_0^2(\frac{f}{f_0} - \frac{f_0}{f})^2}. \tag{4.6}$$

At the resonant condition the imaginary part is zero $(B_c + B_b) = 0$. The numerical study of cavity performance according to the equivalent circuit model was done using KUBLAI code [77].

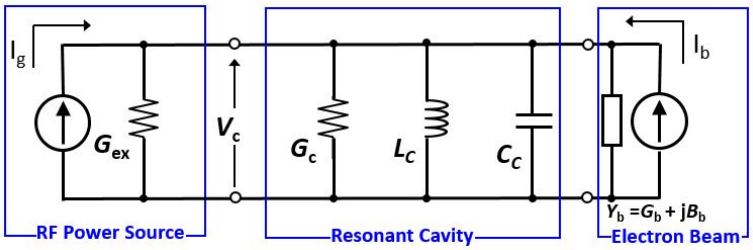

Figure 4.8: Equivalent circuit model for the beam loaded cavity [73].

4.3 Triode Operational Conditions

For successful pre-bunching of emitted electrons, the RF phase of triode cavity and that of the main cavity has to be synchronized. According to numerical studies the maximal peak current I_{peak} is attained at different phase difference φ between the triode cavity, for different cavity voltages. Thereby the beam properties do not significantly change for the cavity voltage $20kV$-$30kV$. Table 4.1 summarizes the beam parameters obtained by numerical study [78].

Table 4.1: Beam parameters at highest peak current ($J_c = 80A/cm^2$, $L_g = 3.35mm$ (gasket length)) [78].

	20 kV	30 kV
φ (degree)	156	137
P_{back} (kW)	2.79	4.77
I_{peak} (A)	110	400
$Q(pC)$	46.6	52.7
$\varepsilon_{rn}(\pi mmmrad)$	3.27	2.69

4.4 Cavity Test

The designed values of the triode cavity according to numerical simulations are: $Q_0 = 2816, R/Q = 68.7, V_c = 10 - 30kV$ and surface current density $J = 80A/cm^2$, with peak current of $I_{peak} = 62A$ $(20kV)$ [78]. The triode cavity was tested separately from the 4.5-cell accelerating body in an isolated vacuum chamber.

4.4.1 Testing Setup

The measurement setup for low and high input power is shown in Fig.4.9. The triode cavity vacuum chamber was equipped with a Faraday cup located $36mm$ away from the cavity aperture. Different setups were used for the high and low power tests. For the low power test with input power of $1mW$, reflected power and frequency dependence were measured using a spectrum analyzer (Agilent, $N9320B$) in cw mode. Reflected power was measured using a circulator. For higher input power, the $10MW$ klystron, which supplies the KU-FEL facility, was used as pulsed RF source with $1Hz$ repetition rate. The input and reflected power were simultaneously measured using an oscilloscope with two diode detectors and a bidirectional $40dB$ coupler.

4.4.2 Heating Test

The heating test was conducted in order to estimate the influence of the environmental temperature on the resonance frequency. The cavity can be heated up during the operation by wall heating due to the absorption of RF power and by cathode heating due to radiation and contact heating. In this experiment, the external ribbon heater, as shown in the Fig.4.10 was used for wall heating test.

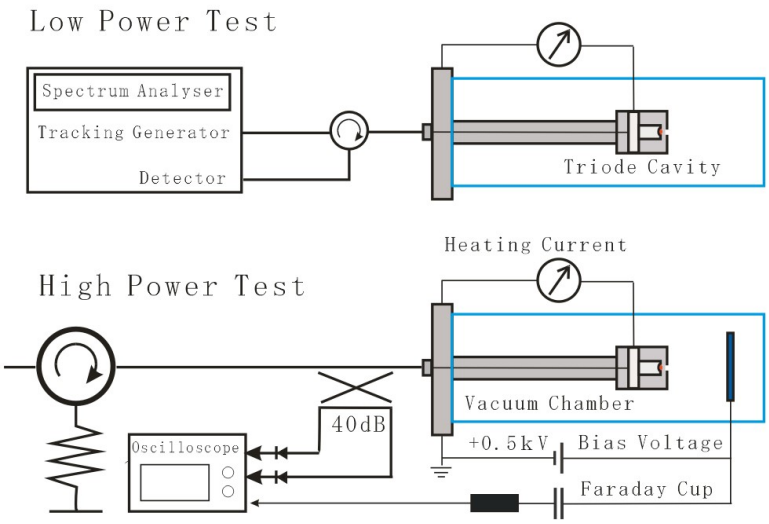

Figure 4.9: Cavity testing setup for low and high input power [73].

The temperature was measured at the cavity wall using a wire thermometer while the frequency was measured using a spectrum analyzer. In the heating test, the cavity was outside of the vacuum chamber, under atmospheric pressure. A stainless dummy plug was used instead of the cathode. Figure 4.11a shows the dependency of resonance frequency on the cavity wall temperature. The cavity resonance was found to change by $-60kHz/K$ when the cavity wall temperature rises. The body temperature of the 4.5-cell thermionic RF gun is kept at $335K$ [4]. Since the triode cavity is intended to be attached to the 4.5-cell cavity body, the triode cavity temperature is not expected to exceed this value.

For the cathode heating test, a tungsten dispenser cathode with a diameter of $2mm$ (fabricated by Heat Wave) was applied. The test was conducted in vacuum chamber at a vacuum pressure of $7.5 \times 10^{-8} Torr$. The resonance frequency (measured using a spectrum analyzer) at room temperature ($286.15K$) was $f_0 = 2.8687GHz$. The cathode heating changes the resonance by $-2.5kHz/K$ as shown in Fig.4.11b. The difference in the frequency dependence by body heating and cathode heating verifies the good isolation

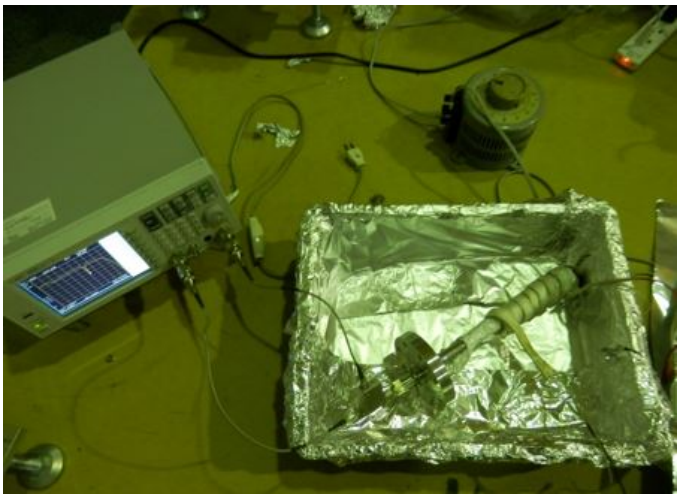

Figure 4.10: Ribbon heating test setup.

of the cathode material and cavity walls.

The maximal possible cathode heating power is $P_w = 8.7W$, which corresponds to a cathode temperature of $1811K$. The cathode operation conditions are usually 1500-$1700K$. The corresponding current density is $J = 19.4\text{-}102A/cm^2$ as estimated by the Richardson-Dushman equation for tungsten dispenser cathode [7]. The triode cavity was designed in such a way that resonance frequency can be adjusted by a stub tuning mechanism. In order to meet the resonance frequency of $2.856GHz$ for the cold test, a gasket with $2mm$ thickness and stubs of $1mm$ length were used.

4.4.3 Cold Test

The cold test was conducted to determine the attainable maximal cavity voltage without beam loading. A cathode dummy made of stainless steel (SUS) was used for the cold test. The properties of the triode cavity were tested at vacuum pressure of $3 \times 10^{-7}Torr$ in a

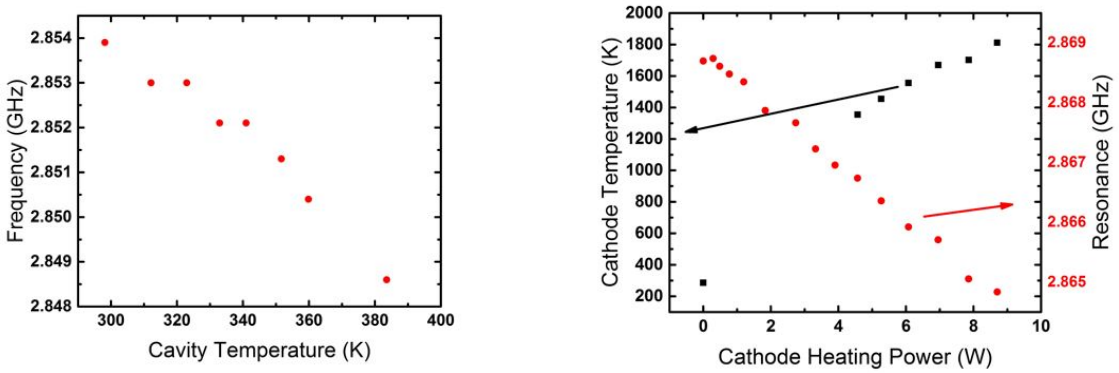

(a) Ribbon heating **(b)** Cathode heating

Figure 4.11: Frequency dependence of the triode cavity on heating [73]. (a) Ribbon heating of cavity body. (b) Cathode heating.

test vacuum chamber detached from the 4.5-cell RF gun. Since the load in the low and high power tests is different, the cavity parameters also deviate slightly .

4.4.3.1 Cavity Parameters

Cavity parameters (β, Q_0) were calculated by fitting the cavity resonance curve according to Eq.4.4. Since the fitting equation has a quadratic dependence on β, there could be two solutions corresponding to the coupling conditions. To select the appropriate solution, cavity coupling conditions must be determined. According to the equivalent circuit model, the coupling coefficient is defined as:

$$\beta = \frac{G_{ex}}{G_c} = \begin{cases} > 1 & \text{overcoupled conditions} \\ = 1 & \text{critically coupled conditions} \\ < 1 & \text{undercoupled conditions.} \end{cases} \tag{4.7}$$

In the triode cavity the coupling coefficient was designed for strong overcoupling, since high β ensures wide frequency acceptance. The coupling conditions are determined by

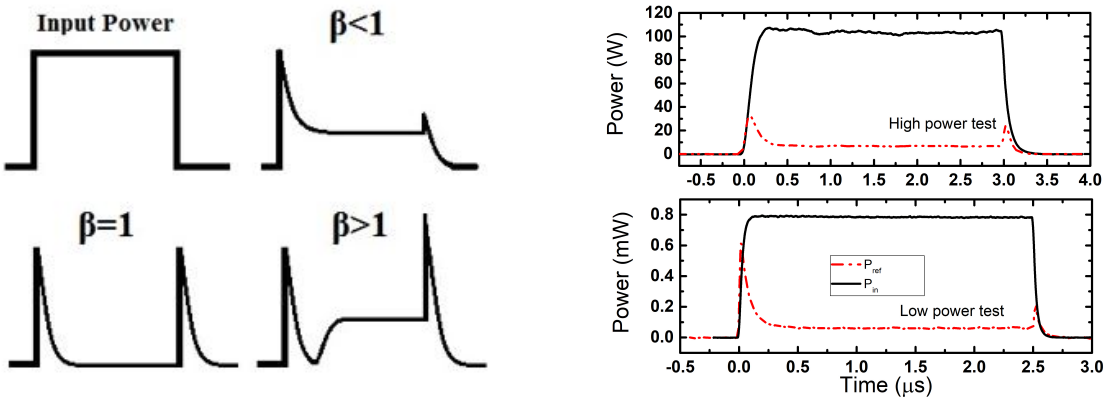

(a) Transient signal structure

(b) Macropulse at low and high power

Figure 4.12: Transient power signal [73].(a) Signal structure of reflected power for different coupling conditions. (b) Measured Signal at high and low input power.

geometrical structure of the half-moon shaped coupling holes (see Fig.4.4). The actual coupling condition can be determined from the transient signal form as shown in Fig.4.12a [79]. Figure 4.12b shows the measured transient signal of the cavity for high and low power tests. The measured transient signal clearly shows undercoupled conditions contrary to the design.

The numerical calculation of coupling coefficient for triode coupling geometry is difficult. The deviation in coupling condition is caused by inaccurate calculation and the complexity of fabrication process. The dependence of the measured power ratios (reflected power/input power)on the input RF frequency is shown in Fig.4.13 for both low and high power tests. Results of the two tests are in agreement. The cavity parameters obtained from fitting are shown in Table 4.2.

The evaluated value of Q_0 is different from designed one. The deviation is due to the effect of machining and handling on the cavity inner walls. Surface deformation degree and roughness do affect Q_0 significantly.

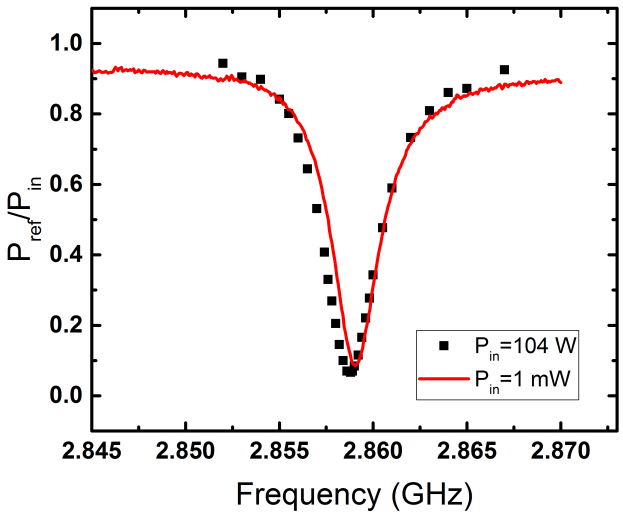

Figure 4.13: Resonance curves as measured by low and high power tests [73].

Triode cavity parameters were already reported previously in Ref.[80]. However, those values were calculated with the wrong assumption of overcoupling conditions and are not in agreement with real values.

4.4.3.2 Power Dependence

Figure 4.14a shows the power ratio P_{ref}/P_{in} for different P_{in} values under resonant conditions. If P_{in} exceeds the value of $3.4kW$, the power ratio and the resonance frequency increase unexpectedly. The power ratio is expected to be constant for any input power at resonant conditions unless electron emission is taking place. For the higher power region a small discharge current after RF pulse is measured by Faraday cup. The inset shows also the increase in level of P_{ref} compared to the situation at lower power ($P_{in} < 5.54kW$). This increase is possibly caused by the beam loading even if no electron beam is detected by the Faraday cup. Figure 4.14b shows the graph of cavity voltage derived from Eq.4.2

Table 4.2: Cavity Parameters

	Low Power	High Power	Designed Values
Resonance frequency (GHz)	2.8591	2.8588	2.856
Unloaded Quality Factor (Q_0)	1376+/-14	1250+/-39	1400
R/Q Value (from 2-D FEM Simulation)	62.9		
Coupling Coefficient β	0.52	0.59	»1

for the resonant case without beam loading. The cavity voltage corresponding to the threshold where the resonance shift take place ($P_{in} = 3.4kW$) is $V_c = 22.7kV$. This is a sufficient voltage for beam generation [78].

4.4.4 Hot Test

The hot test (with cathode heating) was undertaken to verify whether the system can generate electron beams with sufficient properties for driving an oscillator-type FEL facility. Figure 4.15 shows the tungsten dispenser cathode as used for the hot test. The molybdenum cathode mount with joule heater is shown in Fig.4.15c. For comparison the stainless steel dummy cathode as used for cold test is shown in Fig.4.15d. The dispenser cathode installed in the cavity is shown in Fig.4.15a. The photo of glowing cathode in the vacuum chamber, as given in Fig.4.15b, verifies that the joule heater is working properly.

The heating characteristics of the tungsten dispenser cathode used for the test were described earlier in section *Heating Test*. The triode cavity was tested under vacuum conditions of $3 \times 10^{-8} Torr$.

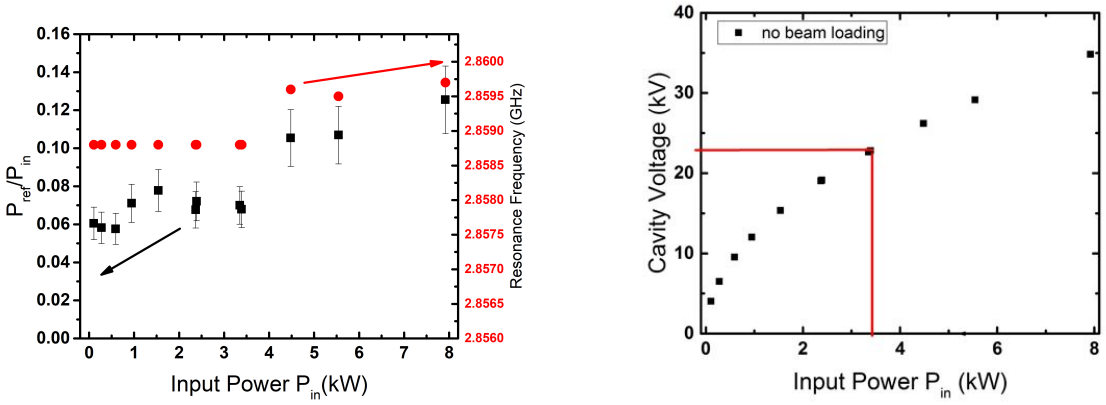

(a) Power ratio **(b)** Cavity voltage

Figure 4.14: Input power dependency of the cavity using dummy cathode [73].

Figure 4.16 shows the photo of configuration of testing setup for high power test.

The measured power ratio dependence on P_w, for high input power ($P_{in} > 10kW$) is shown in Fig.4.17a. At a high heating power the reflecting power is increased significantly. This behavior indicates a voltage drop in the cavity. When reflected power is increased, a current during the macropulse is detected. Figure 4.17b shows the transient RF signals and detected current for the case of $P_{in} = 14kW$ and $P_w = 8.02W$. This current has low frequency dependency (see Fig.4.18b) and low sensitivity to heating power change. The energy of detected electron current of around $1keV$ was estimated by scanning over negative bias voltage at the Faraday cup, as shown in the Fig.4.18a. The energy and the current of the electron beam are too low for the application for FEL.

At the condition of increased P_{ref} due to changed coupling situation, there is no significant resonance structure in power ratio, at least not in the considered range ($2.871-2.855GHz$, resonance at $P_{in} = 1mW$ was $2.660GHz$), which is shown in Fig.4.18b. The measured current under the condition of $P_w = 8.02W$ and $P_{in} = 13kW$ is $I_f = 3.1\mu A$ (see Fig.4.17b). With the assumption of an ideal thermionic emission the expected current density for

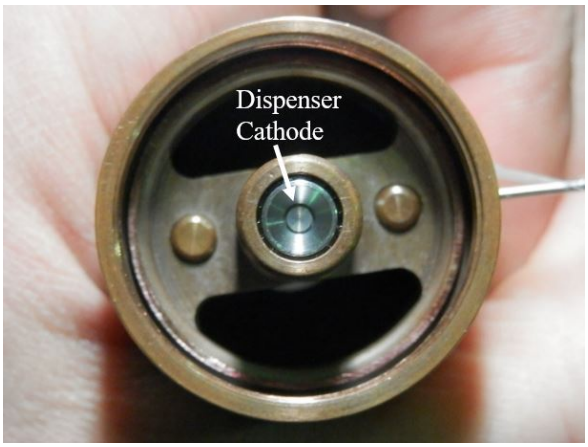

(a) Cathode embedded in the cavity

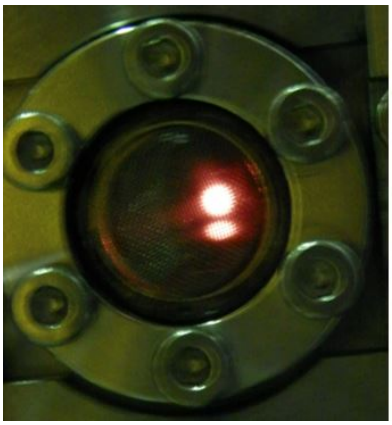

(b) Hot cathode

(c) Cathode mount with joule heater

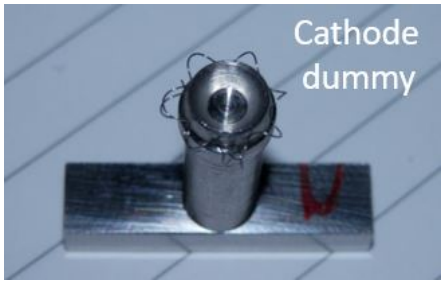

(d) Dummy cathode

Figure 4.15: Tungsten dispenser cathode with joule heater and SUS dummy cathode.

the cathode with a temperature of $1800K$ ($P_w = 8W$) is $J = 208A/cm^2$. For a rough estimation, the current can be assumed to be half of the ideal thermionic current $I_{th}/2 = 3.26A$ (at $1800K$), which gives an electron extraction efficiency of $I_f/I_{th} \sim 1 \times 10^{-6}$. Since the extraction ratio is very low, the real beam admittance can't be evaluated from the measurement. The cavity voltage of about $15kV$ is calculated from the difference of measured P_{in} and P_{ref}. This voltage however, includes the energy consumed by the beam. The measured values for the extracted beam energy is negligible for this voltage.

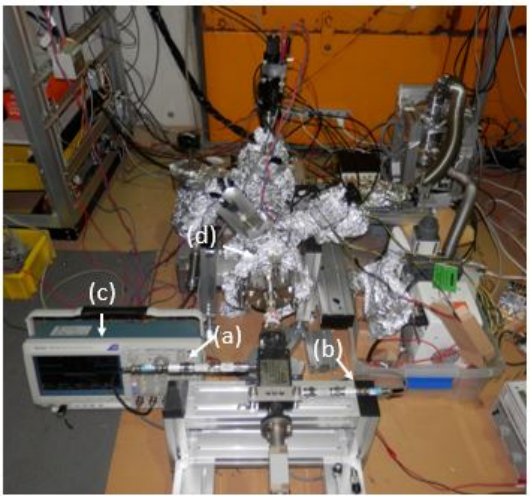

(a) Crystal detector for measurement of input power
(b) Crystal detector for measurement of reflected power
(c) Oscilloscope
(d) Triode vacuum chamber

Figure 4.16: Photo of testing triode device in vacuum chamber.

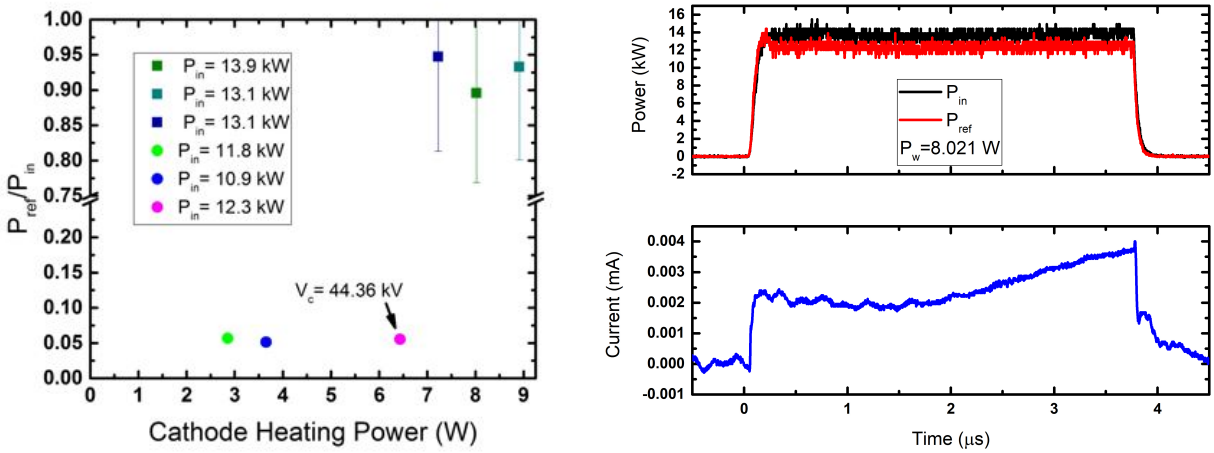

(a) P_{ref}/P_{in} versus P_w [73]

(b) Conditions with high P_{ref}

Figure 4.17: High power test with cathode heating.

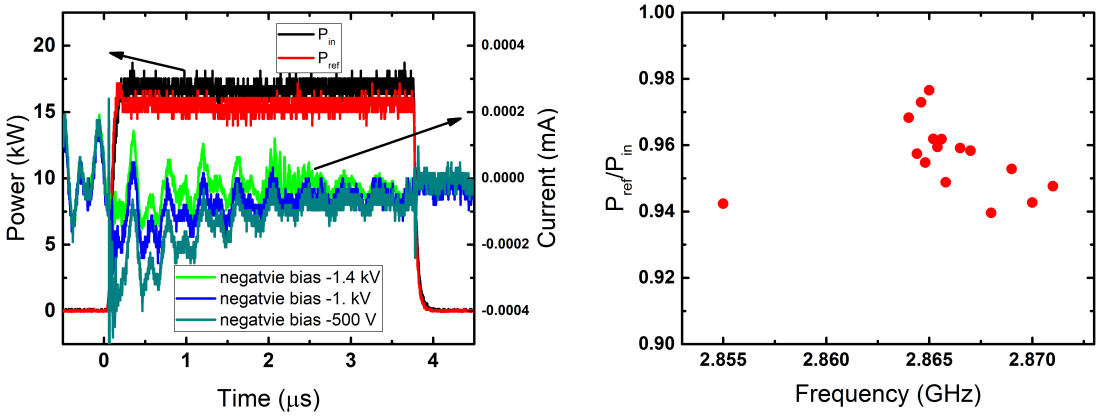

(a) Current at negative bias voltage

(b) Conditions with high P_{ref} [73]

Figure 4.18: (a) Electron beam energy estimation using negative bias. (b) Frequency dependence of P_{ref}/P_{in}.

4.5 Discussion

The results of cold test have demonstrated that sufficient cavity voltage of $22.7kV$ is attainable for the triode cavity. At a higher voltage some discharge current at the end of the RF macropulse was detected (see Fig.4.19d). The discharge indicates field emission in the vicinity of the aperture due to a high electric field in the cavity gap. Cathode heating increases the discharging current, which leads to abrupt changes in coupling conditions. Some current with low beam energy can be coupled out and detected. The low frequency dependence of the power ratio at the changed coupling condition indicates a high value of beam susceptance $B_b >> B_c$. This also means that the thermionic electrons are bunched in the cavity.

The low extraction ratio of electrons and changed coupling conditions can be explained by the influence of the multipactoring process [82]. Since multipactoring is power-dependent,

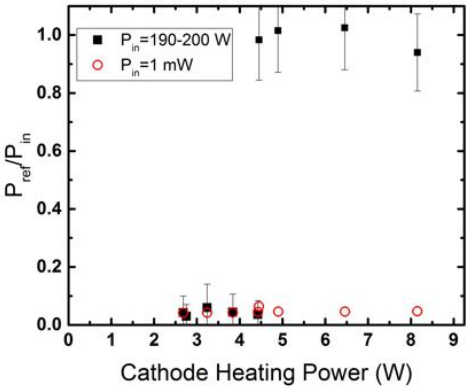

(a) P_w dependence [73]

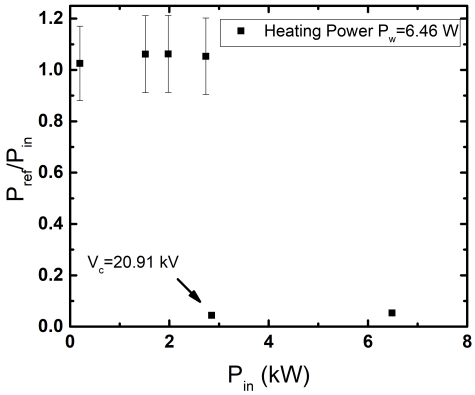

(b) P_{in} dependence

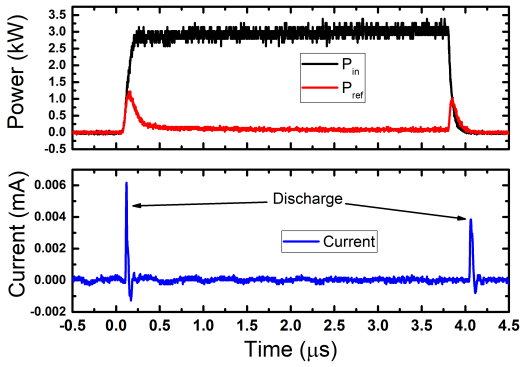

(c) Hot test discharge

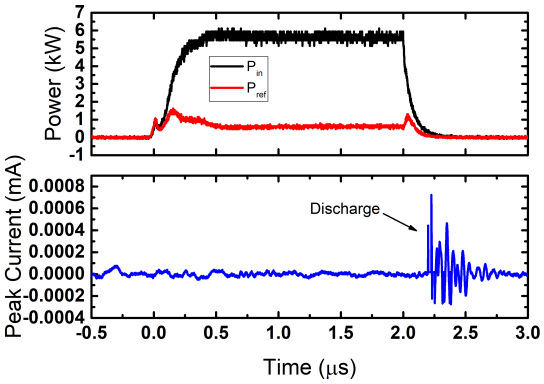

(d) Cold test discharge

Figure 4.19: Power ratio dependence on: (a) heating power at low P_{in}, (b) input power at high P_w, (c) two discharges by hot test, (c) discharge by cold test.

more information can be collected through the consideration of the cavity behavior at low input power.

Figure 4.19a shows power ratio dependence on the cathode heating power at low P_{in} ($\sim 200W$ and $1mW$). The change of coupling conditions with P_{ref} close to 100% was observed when the heating power exceeded $4.45W$. The cavity voltage before the change in coupling condition was $5.83kV$. This phenomenon is power-dependent and disappears for higher input power as shown in Fig.4.19b (with $P_w = 6.46W$). When the cathode heating is increased, the coupling condition changes again, leading to a high reflected power. The observed power dependence proves the assumption of multipactoring. However, the cathode heating lowers the frequency and power dependency of multipactoring, which makes the evaluation of multipactoring more complex.

An unexpected result is that no electron beam is detected at high cavity voltage conditions. The Fig.4.19c shows the transient signal at the point, where the conditions with changed coupling disappear at sufficiently high power. The transient signal shows 2 discharges, one at the beginning of the macropulse and another one at the end. The discharge detected at high cavity voltage by cold test has only one signal at the end of the macropulse, as shown in Fig.4.19d. The 2 discharges indicate that electron extraction from the cavity is an effect occurring at the low voltage that disappears due to the transient rise and decay of electric field in the cavity. In order to estimate the influence of the discharge, the beam loading conditions have to be considered.

4.5.1 Beam Loading Influence

The change in coupling conditions for the cold test takes place when the input power exceeds $3.4kW$ (see Fig.4.14a). This change is caused by beam loading. Figure 4.20 shows the P_{ref}/P_{in} for the cold and for the hot test ($P_w = 6.46W$). Estimation of beam

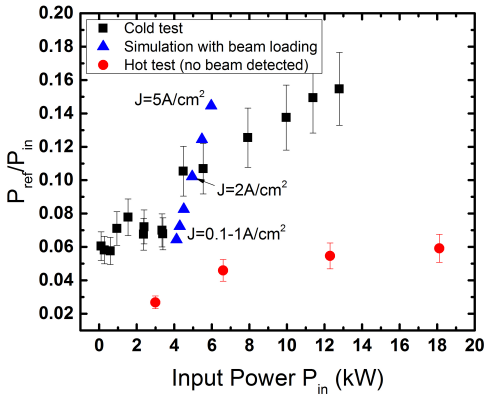

Figure 4.20: Power ratio for hot and cold tests and simulated beam loading for various current densities $J = 0.10 - 5A/cm^2$ [73].

loading effect is also included in the figure (triangles). Based on simulations the change in coupling, which is detected by the cold test, is caused by the current density of $2-5A/cm^2$. Despite the detected discharge, the power dependence of the hot test didn't show beam loading influence. In order to estimate the cavity voltage conditions at discharge, the transient signal is evaluated.

4.5.2 Cavity Voltage and Discharge

The evolution of cavity voltage can be estimated according to RLC circuit equation:

$$I_g(t) = GV(t) + \frac{1}{L}\int V(\tau)d\tau + C\frac{dV(t)}{dt}. \tag{4.8}$$

The equation is solved using Laplace transformation.

$$I_g(t) = \frac{|I_g(s) - I_0|/C + V_0 s}{s^2 + sG/C + 1/LC}. \tag{4.9}$$

The I_g is the generator current according to the equivalent circuit (see sect.4.2.3). It is derived from the measured transient of P_{in}. The I_0 and V_0 are initial values for current

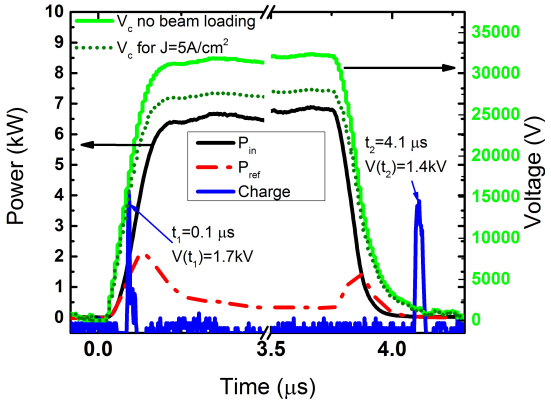

Figure 4.21: Transient signal of cavity voltage as calculated from the measured input power with ($J = 5A/cm^2$) and without beam loading [73].

and voltage, respectively. An example of the calculated cavity voltage evolution in beam-loaded and unloaded cases is given in Fig.4.21. The transient signal allows us to estimate the cavity voltage $V_c(t)$ at the time when discharge occurs at the beginning and at the end of the macropulse. Since the discharge impacts the cavity voltage, the calculated values are approximate. The difference in the rising and decaying voltages for the cases with beam loading ($J = 5A/cm^2$) and without beam loading is negligible. Because of this, the beam loading influence is not considered further.

Figure 4.22a shows the dependence of cavity voltage on input power when the discharge appears.

The range of voltage conditions causing discharge is $5 - 8kV$ at decaying field for the cold test. In the case of the hot test, cavity voltages at discharge for the decaying field are between $0.8 - 1.7kV$. These results correspond to the estimated extracted electron beam energy of $\sim 1keV$ (see Fig.4.18a). With regard to the decaying field, the discharge voltage can be considered as independent from the input power for both the hot and cold tests.

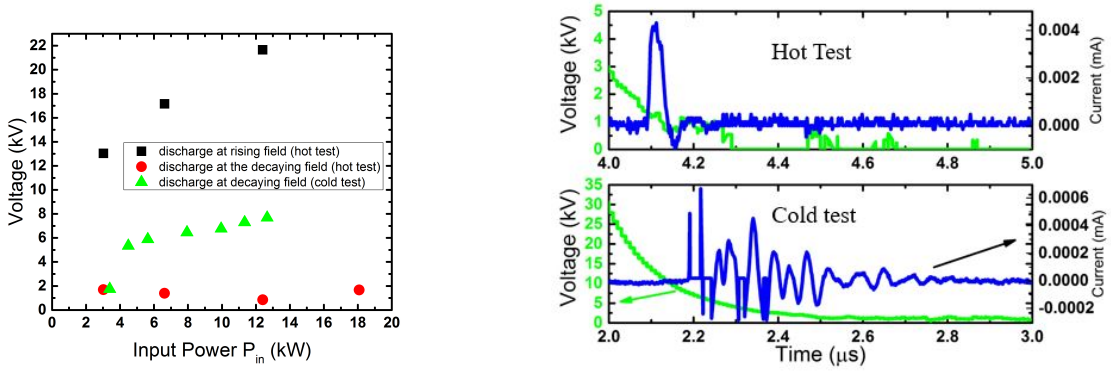

(a) Cavity voltage estimation for discharge **(b)** Discharge current at the end of macropulse

Figure 4.22: Cavity voltage estimation [73]. (a) At time point of discharge. (b) Discharge shape at high and low power tests.

The discharge current of the cold case is an order lower than the hot case. The waveforms of the discharge current are also different in both cases. The cold case has a discharge oscillating in a wide temporal range. The decaying voltage over the discharge oscillating time has large uncertainty of about $dV = 6kV$. The hot case has a discharge having a well defined bell shape with width around $dV = 0.6kV$. Figure 4.22b shows examples of a discharge current for the cases of hot and cold tests.

For the rising field, the discharge occurs at different voltages $V_c(t) = 13, 17.2$ and $21.7kV$. The discharge voltage at the decaying field is lower when the cathode is heated, hence the heating benefits electron extraction. Assuming that the discharge is the result of the multipactoring process, the decaying field, where the discharge occurs (see Fig.4.22a) can be considered as conditions corresponding to the multipactoring. In case of rising field the filling time is different (shorter) from the decaying field. The filling time of the cavity itself $\tau = 2Q_L/\omega_{cav} = 0.09\mu s$. The discharge response time is lower than the filling time and is detected at a different voltage depending on the input power. The discharge at rising field did not occur for the cold test. This means that the rising time is too fast for

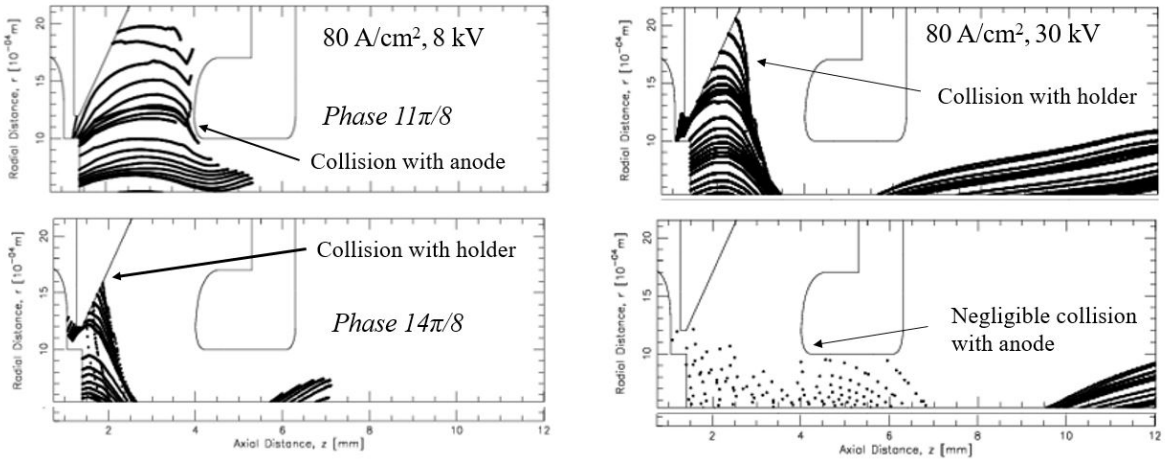

Figure 4.23: Beam tracking snapshots at two phases for $J = 80A/cm^2$ at $V_c = 8kV$ and $V_c = 30kV$. The y- axis is the radial distance in $10^{-4}m$ [81].

the discharge initiation process. For the hot test, the back-bombardment process of low energy thermionic electrons does benefit the seeding of secondary electrons.

4.5.3 Multipactoring

In case of cathode heating and cathode dummy, the multipactoring occurs at the low voltage, which is established in the cavity for a short time by the loading and decaying field. The multipactoring condition can be described by a two-side model [82]:

$$V_0 = \frac{(4m_e\pi)}{e}\frac{(f^2d^2)}{(2n-1)} \tag{4.10}$$

with V_0 -threshold multipactoring voltage, m_e -electron mass, e -electron charge, f -RF frequency, d - gap distance, and n -order of multipactoring. Resolving the equation and calculating for $V_0 = 6kV$ and first order process ($n = 1$), the gap distance is obtained as $d = 3.2mm$. In the case of the hot test with $V_0 = 1kV$, the gap distance is $d = 1.3mm$.

This estimation allows us to locate the multipactoring process according to cavity geometry. The length of $1-2mm$ corresponds to the distance between the cathode material and the aperture nose. The beam tracking simulation can provide further information about the processes in this region.

Figure 4.23 shows snapshots of beam tracking simulation for $J = 80A/cm^2$ at low $V_c = 8kV$ and high $V_c = 30kV$ voltages. The low energy electrons do not leave the triode cavity with the accelerating half RF period and are accelerated back into the cathode mount (holder), which is shown as a snapshot at $14/8\pi$ phase. The snapshot at $11/8\pi$ phase, shows the high beam divergence for the low cathode voltage ($8kV$). Due to the divergence some electrons hit the aperture nose. At high cavity voltage the divergence is small and the most of electrons do not impact the anode. Such relation is confirmed by the plot of beam conductance G_b for various current densities, which is shown in Fig.4.24a. At $V_c > 8kV$ the beam conductance is proportional to the current density. Below $8kV$ the conductance can be higher at lower current density, which indicates disproportional particle loss due to the absorption on cavity walls (electrons hitting the aperture nose). There are two locations which are suspected to initiate the multipactoring. First one is the cathode holder and the second one is the aperture nose. The calculation of the impact on these locations for $J = 80A/cm^2$ over one RF period is shown in Fig.4.24b. The impact by the back- streaming electrons on cathode holder is higher than that on aperture nose, caused by diverging electrons. The cathode holder is made of molybdenum (Mo) and the anode of oxygen free copper (OFC). According to the Ref.[83], the Mo has maximal yield of secondary electron emission ($\delta_m = 1.25$) at lower primary electron power ($E_m = 375eV$) than Cu ($\delta_m = 1.3$, $E_m = 600eV$). This fact leads to conclusion that the *Secondary Electron Emission* (SEE) is initiated by the back- streaming electrons hitting on cathode holder. The SEE is evolving then to the multipactoring process between the cathode

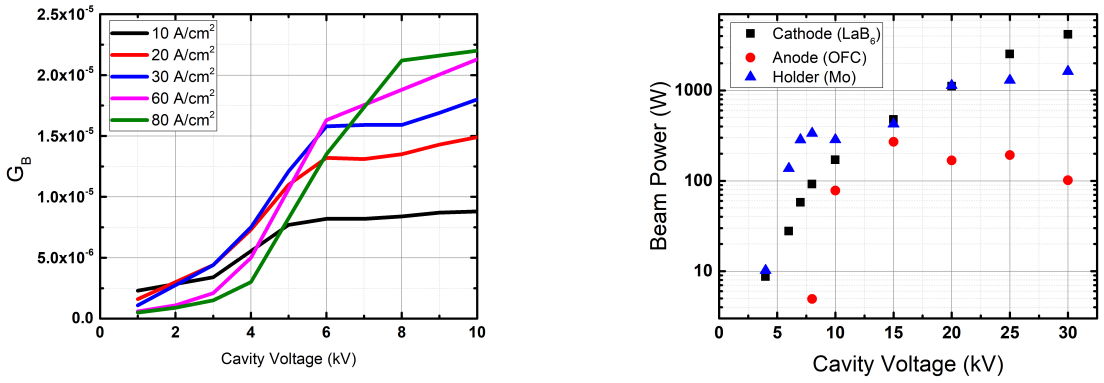

(a) G_b for different current densities

(b) Electron impact, $J = 80A/cm^2$

Figure 4.24: Particle loss and impact in the triode cavity [81].

holder and the anode nose, because of resonant conditions at driving RF frequency. An unclear finding is that the multipactoring condition (low V_c) in the hot test is maintained over the macropulse duration at a certain cathode heating (see Fig.4.17b).

4.5.3.1 Countermeasures

In order to continue the proof of principles the multipactoring must be suppressed. Therefore several strategies can be followed:

- Change the coupling conditions
- Coating
- Change the cavity geometry

The coupling conditions of the cavity can be modified applying an impedance transformer. In course of this work an impedance transformer was been developed [84]. However, the coupling conversion to $\beta = 2.3$ did not suppress the multipactoring as shown in the

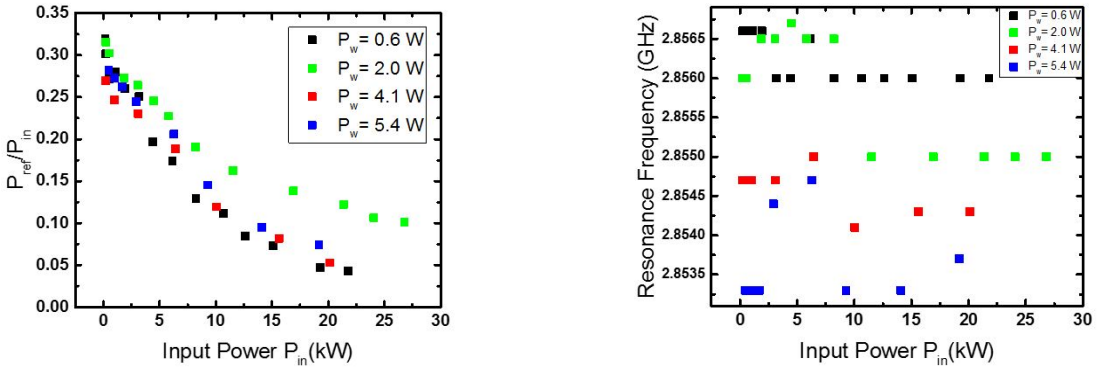

(a) Power ratio at variousP_w **(b)** Frequency dependence

Figure 4.25: Power dependency of P_{ref}/P_{in} for different cathode heating powers P_w at overcoupling conditions ($\beta = 2.3$).

Fig.4.25 ($P_{ref}/P_{in} \neq const.$).

For a given cathode heating power, the multipactoring condition could be suppressed by sufficiently high input power. However, the thermionic beam was not detected in such case. The reason for the absence of the beam is not clear yet.

The coating seems to be an appropriate options. According to the graph 4.24b the coating on the cathode holder itself would be sufficient to prevent SEE. Similar approach would be the application of the cathode holder made from a material with higher SEE threshold. The change in geometry is an critical issue for the beam trajectory since the triode cavity was designed to maintain low energy spread and transverse emittance. Modifications on the anode might degrade the beam properties. Since the SEE is initiated on cathode holder the anode geometry can be kept at present design, which is an important finding. Owning to the separable structure of the cavity it is possible to modify the cathode holder itself without significant change on anode. This gives a good opportunity to apply fine grooving on cathode holder to suppress multipactoring [85]. The suppression of multipactoring is the outgoing work for this study.

4.6 Summary

The quarter wavelength coaxial cavity for the triode type thermionic RF gun was tested under cold and hot cathode conditions. The cold test showed that a cavity voltage of $22.7kV$ is attainable. This voltage is enough for the generation of a high-quality electron beam. At a higher cavity voltage a discharge at the end of RF macropulse occurred.

For the hot test a tungsten dispenser cathode was used. The cathode heating power of $P_w > 4.45W$ causes abrupt changes in coupling conditions with significant increase of reflected power even at low input power ($200W$). Under these conditions, a beam current was detected. The beam current was $3.1\mu A$ with a cavity voltage of $15kV$ and electron energy of about $1keV$ (estimated by negative bias voltage scan). The electron emission efficiency according to Richardson-Dushman equation is about 0.0001%. Such beam properties are not sufficient for operation in FEL facility.

Further study showed that the cavity undergoes a process limiting the rise of cavity voltage, which was identified as multipactoring. The multipactoring occurred at a cavity voltage of about $5-8kV$ for the cold test. For the hot test, the discharge at decaying field happens at a cavity voltage of about $1kV$. The multipactoring distance was estimated by a two-side model to be $d = 1.3-3.2mm$. For the rising field, the discharge shows dependence on input power. The beam tracking study has shown that the cathode holder experiences impact from back-streaming electrons at decaying field during one RF period. There are strong evidences that this impact causes secondary electron emission, which evolve to the multipactoring between the anode and cathode holder at driving frequency. Due to multipactoring, the operation of the current design triode cavity as a pre-bunching cavity is not possible. Some suggestions to overcome the multipactoring were also provided.

4.7 Conclusions

In this study the proof of principles for the triode type RF gun could not be completed because of unexpected multipactoring processes in the triode cavity. This work demonstrates that for the design of a small-sized cavity, the low power effects like multipactoring must be considered. This study provides an founded suggestion regarding the origin and the nature of the multipactoring taking place in triode cavity. Furthermore the study gives indicates that the suppression of the multipactoring can be accomplished without significant modifications on anode geometry, which allows us to maintain the present cavity design. The next step after suppression of the multipactoring would be the beam test and successive implementation of the triode cavity to the 4.5-cell RF gun for FEL performance check. Then the proof of principles of the triode concept would be completed.

The results of the study described in this chapter were partially published/submitted in following articles:

- K. Torgasin et al., *Practical design of resonance frequency tuning system for coaxial RF cavity for thermionic triode RF gun*, in Proc. FEL'12, Nara, Japan, 2012, pp. 333-336.
- K. Torgasin et al., *Cold Test of the Coaxial Cavity for Thermionic Triode Type RF Gun*, in Proc. IPAC'13, Shanghai, China, 2013, pp. 324-326.
- K. Torgasin et al., *Coaxial Quarter Wavelength Impedance Converter for Coupling Control of Triode Cavity*, in Proc. RuPAC'16, St. Petersburg, Russia, Nov. 2016 p. 691.
- K. Torgasin et al., *Properties of quarter-wavelength coaxial cavity for triode-type thermionic RF gun*, Jpn. J. Appl. Phys. 56, 096701 (2017).

- K. Torgasin et al., *Study on secondary electron emission of quarter wavelength coaxial cavity for triode type thermionic RF electron gun*, submitted July 2018.

The content taken from the published paper is presented in this chapter with friendly permission of the publisher, Japan Society of Applied Physics (JSAP). The list of copyright owned figures is given in appendix.

Chapter 5

Thermally Assisted Photoemission (TAPE)

5.1 Motivation

The 4.5-cell thermionic RF gun, which is used for KU-FEL facility was successfully operated in photo-excitation mode [5]. The performance of the RF gun in this mode was given in the chapter 1 of this thesis. The usage of laser for electron extraction allows us to generate short bunches with high peak currents avoiding the Back-Bombardment Effect (BBE). However, the application of laser has some disadvantages. The repetition rate is around 100 times lower as compared to thermionic mode. Further difficulties arise from the complexity of laser systems. The performance of laser systems is strongly correlated with the costs of system components e.g. amplifiers. To improve the performance of the thermionic gun operated in photo-excitation mode using a laser system at the same costs, a special method for controlled increase of cathode Quantum Efficiency (QE) (see section

2.3.1.2) is required.

The laser system of KU-FEL applies 2 amplifiers to increase the laser power [87]. An amplifier has a trade-off relation between the laser power and macropulse duration at certain amplification conditions. In order to extend the laser macropulse duration the initial peak power of the laser has to be decreased. The increase of QE of the cathode would allow us to decrease the laser power maintaining the same photocurrent and to extend the macropulse duration of the laser.

In this chapter a proof of principles is investigated for the increase of the QE, using cathode heating, by so called *Thermally Assisted Photoemission* (TAPE). The chapter consists of two parts, the first describes the experimental measurements and results, the second describes theoretical approaches for explanation of results.

5.2 Introduction

The Thermally Assisted Photoemission (TAPE) is extraction of electrons from the cathode material at high temperature using laser. The heating changes the energy distribution of electrons in materials as shown in Fig.5.1. By heating up a cathode, electrons can occupy a higher energy state than given by Fermi level. At very high temperatures the thermal electron energy can exceed the work function and escape from the cathode. The corresponding thermionic current density on the cathode has been described by Richardson-Dushman equation [13]:

$$J = A_G T^2 e^{(-\frac{\phi}{k_B T})}, \tag{5.1}$$

where ϕ is the work function in eV, k_B is the Boltzmann constant and T is the cathode temperature in Kelvin. $A_G = \lambda_B(1-r)A_0$ is the generalized Richardson constant, which

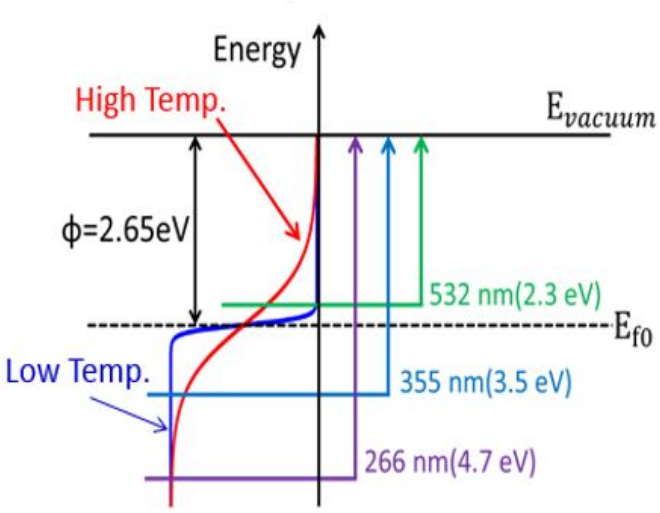

Figure 5.1: Energy diagram schematic of Thermally Assisted Photoemission (TAPE) [86].

contains the averaged quantum-mechanical reflection r, the band structure related correction factor λ_B, and the universal Richardson constant $A_0 = 1.20173 \times 10^6 Am^{-2}K^{-2}$. The TAPE effect makes use of thermionic excitation in order to change the energy distribution of electrons in cathode materials. Due to thermal excitation some electrons occupy higher energetic states, which increases the probability of extraction by photon and the energy of the extracted electrons. Thus the quantum efficiency can be increased by thermal excitation as well.

For conventional Photo-cathode RF guns the cathode heating is not available. Thus the implementation of TAPE can be carried out only on thermionic RF guns in photo-excitation mode.

5.3 Background

Thermionic and photo-electron injectors are widely adopted in FEL facilities. However, the high brightness photo-cathode RF guns have special requirements for the cathode material, vacuum conditions and cavity structure. Very high quantum efficiency (QE) $> 1\%$ semiconductor photocathodes such as Cs_2Te, CsK_2Sb, and $GaAs$, require an extremely high vacuum (XHV) to keep the quantum efficiency for a long time. On the other hand, low quantum efficiency ($0.001 - 0.01\%$) materials such as metal and metal compound photocathodes usually have long lifetimes but require lasers with high pulse energy which increases costs [88]. The main target for further photocathode development is to increase the lifetime of high QE materials or to increase the QE for robust materials.

Some thermionic RF guns are capable to operate in photo-excitation mode. The merit of such operation is the avoidance of BBE and the control over cathode temperature. Thermionic cathode materials have already been applied as robust photocathodes in RF guns. Tungsten dispenser cathodes were reported to be suitable for operation in photo-injectors [89, 90]. Also LaB_6 cathodes have already been successfully used as photocathodes [91]-[94].

Metal hexaborides have been investigated as a cathode material. Since invention in 1950 by J.M. Lafferty [95] metal-hexaboride materials have gained high significance for thermionic cathodes, due to a low work function, high melting temperature, high emission current, compared to other thermionic cathodes, and low evaporation rate [96]. The Figure 5.2 shows the atomic structure of metal-hexaboride compounds. The metal atom serves as electron donor for thermionic emission. The surrounding boron lattice allows diffusion transport of metal atoms to the surface, when evaporation of the surface layer occurs. The materials have high melting temperature and high electron emissivity. In

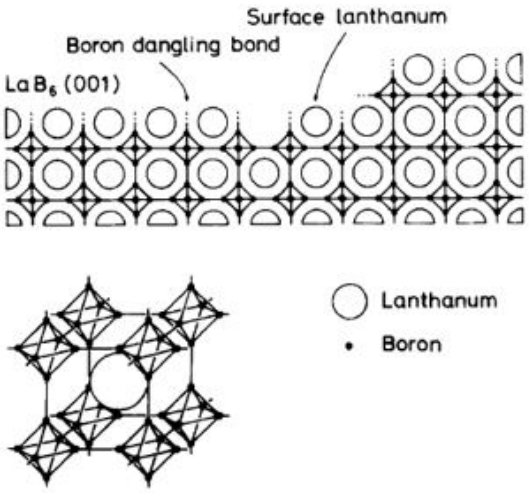

Figure 5.2: Atomic structure of metal-hexaboride compounds [95].

this chapter the focus is set on investigation of photoemission properties of the two representative hexaboride thermionic cathode materials, LaB_6 and CeB_6.

5.4 Samples

Table 5.1 summarizes the main properties of the two cathodes. One significant difference between them is the generalized Richardson constant indicating higher electron emissivity by LaB_6 for the same temperature. On the other hand, it was reported that CeB_6 has a higher resistance to carbon contamination and a lower evaporation rate than LaB_6 [98]. Due to its lower evaporation rate, CeB_6 has a longer lifetime than LaB_6 when it is used as thermionic cathode. Further, the CeB_6 and LaB_6 materials have similar optical properties [99]. Regarding photoexcitation, QEs of both materials were also reported to be the same at $1300K$ for excitation at $266nm$ and $355nm$ [92]. These results suggest that the generalized Richardson constant does not affect the photoemission processes.

Table 5.1: Summary of cathode material properties. Additionally, the correspondence of excitation laser wavelengths and photon energy [97].

	CeB_6	LaB_6
Generalized Richardson Constant ($Am^{-2}K^{-2}$)	3.6	29
Melting point (K)	2463	2483
Work function in (eV)	2.65	2.7
	Wavelength	Photon energy
Photon energy of excitation wavelength	266 nm	4.66 eV
	355 nm	3.49 eV
	532 nm	2.33 eV

However, these QEs refer to low cathode temperature ($1300K$) measurement. In this study the heating range is extended ($< 1800K$).

One point of interest would be the application of the TAPE effect for electron extraction by laser with photon energy below the work function of the cathode material. This process is illustrated in Figure 5.1. External cathode heating increases the population of electrons whose energy is above the Fermi level E_{f_0}, and will reduce the photon energy required for electron extraction.

5.5 Measurement Setup

The measurement setup is shown in Fig.5.3. The cathode materials were tested under DC conditions. The applied voltage between the cathode and the anode was $1kV$ and the electric field about $0.1MV/m$. A nanosecond YAG laser (Surelite II-10, Continuum) with $2Hz$ repetition rate and around $5ns$ pulse length was used as laser source. The

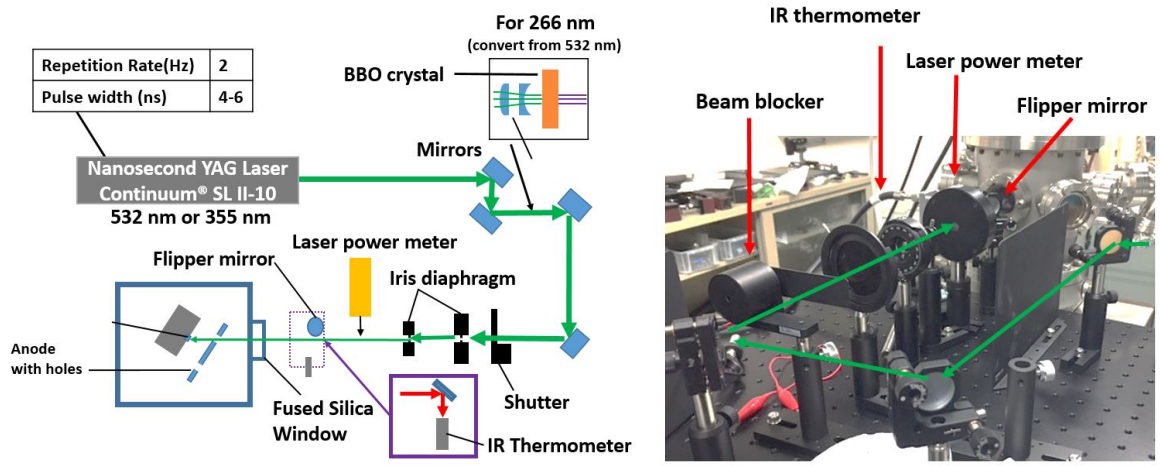

(a) Schematic view **(b)** Photographic view

Figure 5.3: Experimental setup [86].

fundamental wavelength of the laser was $1064nm$. Three laser wavelengths, 532, 355 and $266nm$, were generated by harmonic generation crystals and introduced to the test chamber. The beam diameter of the laser is larger than the cathode diameter, so a small fraction of the beam was selected by an aperture with diameter of $2.7mm$. By this means the intensity spread of the laser profile was reduced. The incident laser beam area was kept constant for all measurements and covered the entire cathode. The laser beam was linearly polarized. The vacuum level was in average $5\times10^{-8}-1\times10^{-7}Torr$. The vacuum conditions showed a slight sensitivity to changes of the cathode temperature and the thermionic current. The cathode temperature was controlled by changing the supplying current to the cathode heater and was measured by an IR thermometer.

The tested cathodes were single crystals with $1.72mm$ diameter in $< 100 >$ orientation, supplied by Applied Physics Technologies. The equivalent circuit diagram of the measurement setup is shown in Fig.5.4a. Figure 5.4b shows the cathode mount with electrical heating. The pulsed photoemission current was AC coupled and measured using an os-

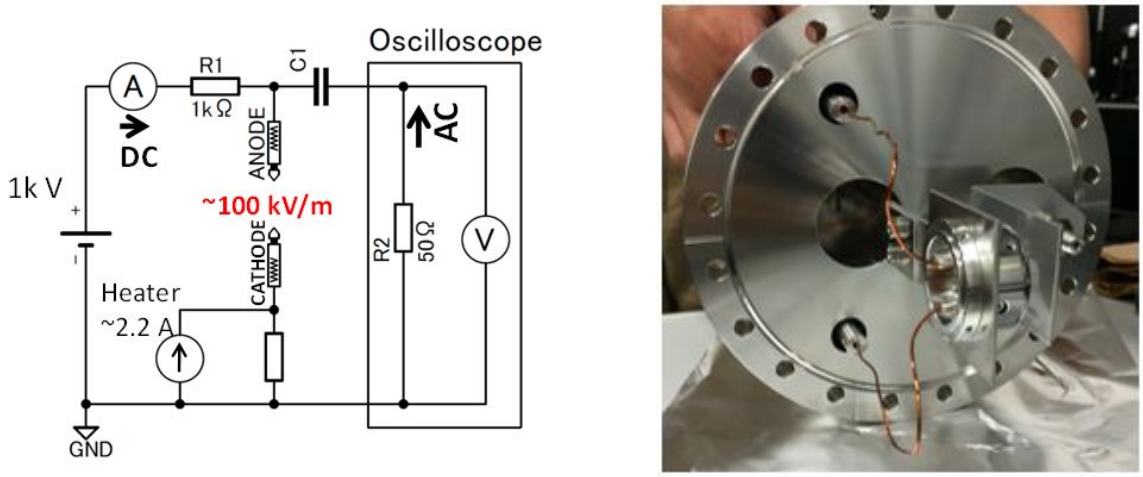

(a) Circuit of measurement setup [86]

(b) Cathode mount

Figure 5.4: Circuit model of the measurement setup and cathode mount.

cilloscope. By means of AC coupling, the DC thermionic current could be measured separately from the photocurrent by an analogue amperemeter.

5.6 Results and Discussion

The main point of interest is to investigate the effects of thermal excitation on the photoemission properties of metal hexaboride materials. Another point is the feasibility of electron extraction by photon energy below the work function of the cathode material using the TAPE effect. Therefore the photoemission at different excitation wavelengths, 266, 355 and 532nm is measured. The correspondence of laser wavelengths and photon energy is given in Table 5.1.

5.6.1 Thermionic Emission of LaB_6 and CeB_6

Figure 5.5 shows the thermionic current dependence on cathode temperature. The plotted data for LaB_6 consists of several measurement sets, which are indicated by different symbols (circles and triangles). When the cathode temperature was increased to $1478K$, a significant increase of thermionic current from LaB_6 was observed. In the case of CeB_6 (square dots in the graph), the cathode temperature needed to be increased up to $1550K$. The measured thermionic current of LaB_6 is higher than that of CeB_6 at the same temperature. Such behavior is attributed to the difference in the generalized Richardson constant (see Tab.5.1) and corresponds to previous work [96]. For comparison the thermionic emission curves according to the Richardson-Dushman equation (Eq.5.1) are also shown in the figure.

The emission rising slope at low current is not well reproduced by measurement. The main reason for it is the surface contamination of materials due to the poor vacuum. Nevertheless the measured emission tendency of both materials correspond to theoretical values in the measured temperature range.

5.6.2 Photoemission at 355 nm

In order to compare the photoemission properties of LaB_6 and CeB_6, photoemission under different temperature conditions has been tested with the laser wavelength of $355nm$. Figure 5.6a shows a typical photocurrent pulse signal measured with the LaB_6 cathode. Figure 5.6b shows the glowing cathode in the vacuum chamber.

Typical laser pulse energy in this experiment was around $13J/pulse$. The current was evaluated by integrating the measured voltage pulse over $100ns$. The measured rela-

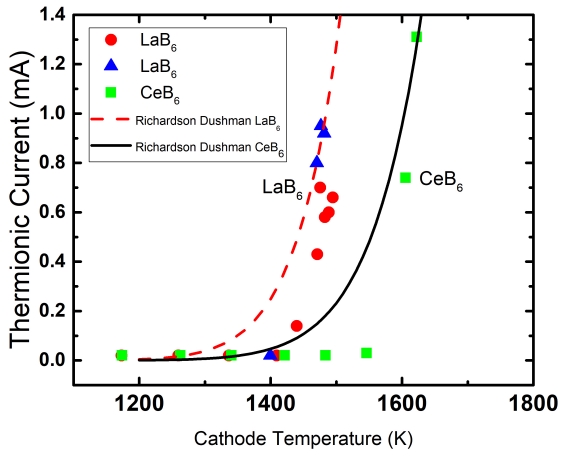

Figure 5.5: Thermionic emission from LaB_6 and CeB_6.

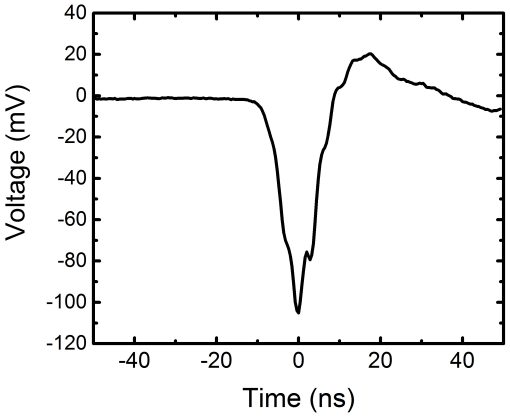

(a) Photocurrent pulse [86]

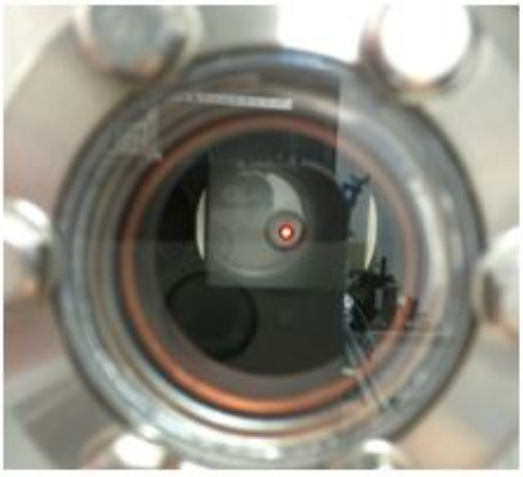

(b) Cathode in the chamber

Figure 5.6: Photopulse and heated cathode.

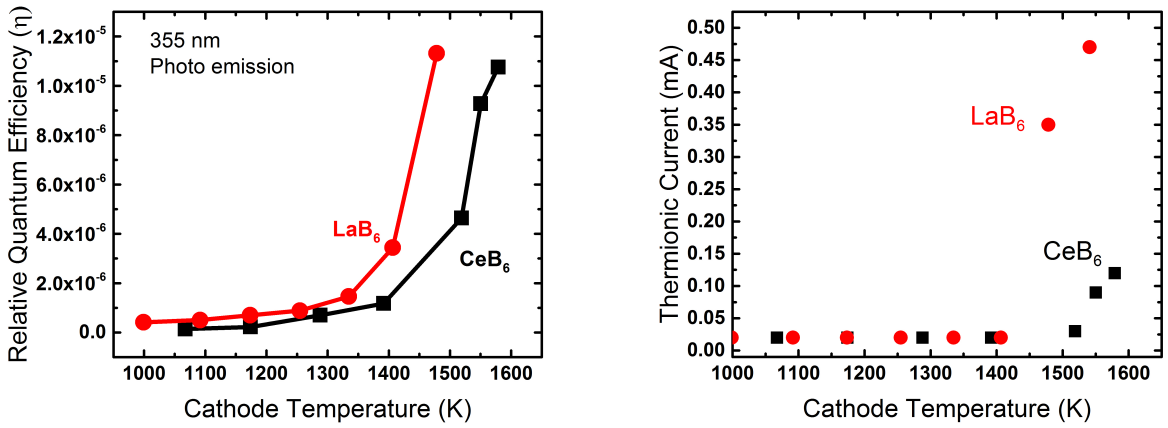

(a) Thermionic current

(b) Relative quantum efficiency @ 355nm

Figure 5.7: Electron emission of LaB_6 and CeB_6 irradiated, thermionic current and the relative QE by irradiation at $355nm$ [86].

tive quantum efficiency as a function of the cathode temperature is shown in Fig.5.7a. Corresponding thermionic current is shown in Fig.5.7b. The photoemission current was normalized by laser power and expressed in relative quantum efficiency (QE) η by the following relationship.

$$\eta = \frac{number\ of\ detected\ electrons}{number\ of\ incident\ photons} \tag{5.2}$$

The relative QE is shown to be temperature dependent. This dependency is different for LaB_6 and CeB_6. The LaB_6 has higher QE than CeB_6 at the same temperature. This tendency corresponds with thermionic emission. It seems that the generalized Richardson constant has an impact on QE, since it indicates the relative difference of the amount of the electrons which reach higher energy levels from thermal excitation.

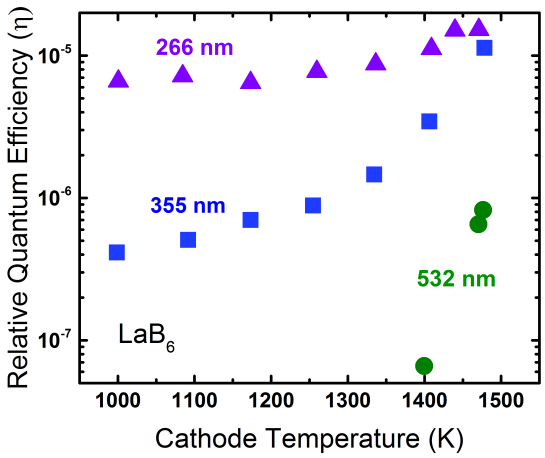

Figure 5.8: Results of relative quantum efficiency measurement of LaB_6 cathode being irradiated at 3 different laser wavelengths, 266, 355 and 532nm [86].

5.6.3 Quantum Efficiency Dependence on the Cathode Temperature at Different Wavelengths

In order to study the photoemission properties related to the photon energy, LaB_6 was illuminated by laser at 3 different wavelengths, 266, 355 and 532nm. The data was acquired by changing the cathode heating from lower to higher temperatures. Figure 5.8 shows the experimental results. The highest photon energy (4.66eV@266nm) shows the smallest dependency on cathode temperature. This behavior indicates that the effect of thermal excitation is small when using photons with higher energy. However, the effect is not negligible regarding laser energy requirement.

As shown in Fig.5.8, electrons could be extracted using 532nm photons if the cathode temperature is higher than 1400K. The corresponding photon energy (2.33eV@532nm) is below the work function (2.7eV).

For low photon energies a special care should be taken to separate the thermionic current from the photocurrent As mentioned in the setup section, the thermionic DC current and pulsed photocurrent are measured separately. The background is measured under beam blocked conditions and subtracted from the detected photocurrent signal. Nevertheless, the laser pulse may increase the cathode temperature temporally with subsequent pulsed thermionic emission. Thus the detected photocurrent may contain a fraction from thermionic current. In order to estimate potential impact of pulsed cathode heating a $1-D$ heat transfer model based on Lambert-Beer law is used [100].

$$C\rho\frac{\partial T}{\partial t} = \lambda\frac{\partial^2 T}{\partial x^2} + I_0^{-\alpha x}, \tag{5.3}$$

with heat capacity $C(J/kgK)$, cathode density $\rho(kg/m^3)$, cathode temperature T, thermal conductivity $\lambda(W/mK)$, cathode depth $x(m)$, laser intensity $I_0(W/m^2)$ and absorption coefficient α.

Figure 5.9 shows the calculated pulsed heating of LaB_6 for the cathode temperature of $1500K$ for several laser pulse energies. The data presented in Fig.5.8 for $532nm$ excitation was recorded with pulse energy of $\sim 32\mu J$, which corresponds to additional heating of $\sim 12K$. Comparing with Fig.5.7b the corresponded thermionic current increase has an order of $10^{-2}mA$. Since CeB_6 has lower electron emission rate at the same cathode temperature, the impact of pulsed thermionic current is lower.

Figure 5.10 shows thermionic and corresponded photocurrent of LaB_6 and CeB_6 for irradiation at $355nm$ and $532nm$. The values of the photocurrent correspond to the maximal measured current, whereas it does not represent the peak current since our detection system is not fast enough to detect $5ns$ signals. The thermionic current from the pulsed heating is negligible. For the $355nm$ wavelength, the photocurrent is significantly higher than the thermionic current for both materials. For the $532nm$ wavelength, the CeB_6 generates a lower photocurrent even at a high laser pulse energy ($\sim 84\mu J$). Nevertheless

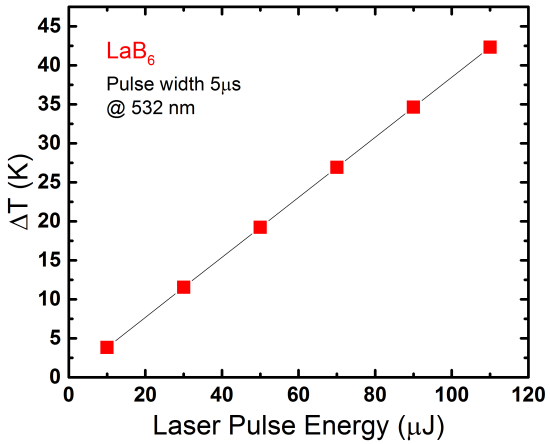

Figure 5.9: Calculation of cathode temperature rise by incident laser pulse energy. Cathode material LaB_6 at $1500K$. Laser wavelength $532nm$ [86].

the estimated pulsed heating current is an order below the measured photocurrent. Thus the result represent the real photocurrent.
The photocurrent extraction by illumination at $532nm$ demonstrates that the TAPE is feasible for both materials below the work function.

Measurements of relative QE at several irradiation wavelengths for CeB_6 are shown in Fig.5.11. The different symbols used for representation of relative QE at the same wavelength correspond to different measurement sets. Deviation between the measurement sets can be accounted for measurement error. Comparing photoemission at $266nm$ and $355nm$ irradiation wavelengths, minimal error is measured for higher photon energy. The data for $532nm$ excitation shows photoemission at a higher cathode temperature $(1700 - 1900K)$. This is caused by material degradation due to long operation times. In order to recover the emissivity the cathode temperature had to be increased. Nevertheless it was demonstrated that the photoemission below the work function can be recovered by increasing

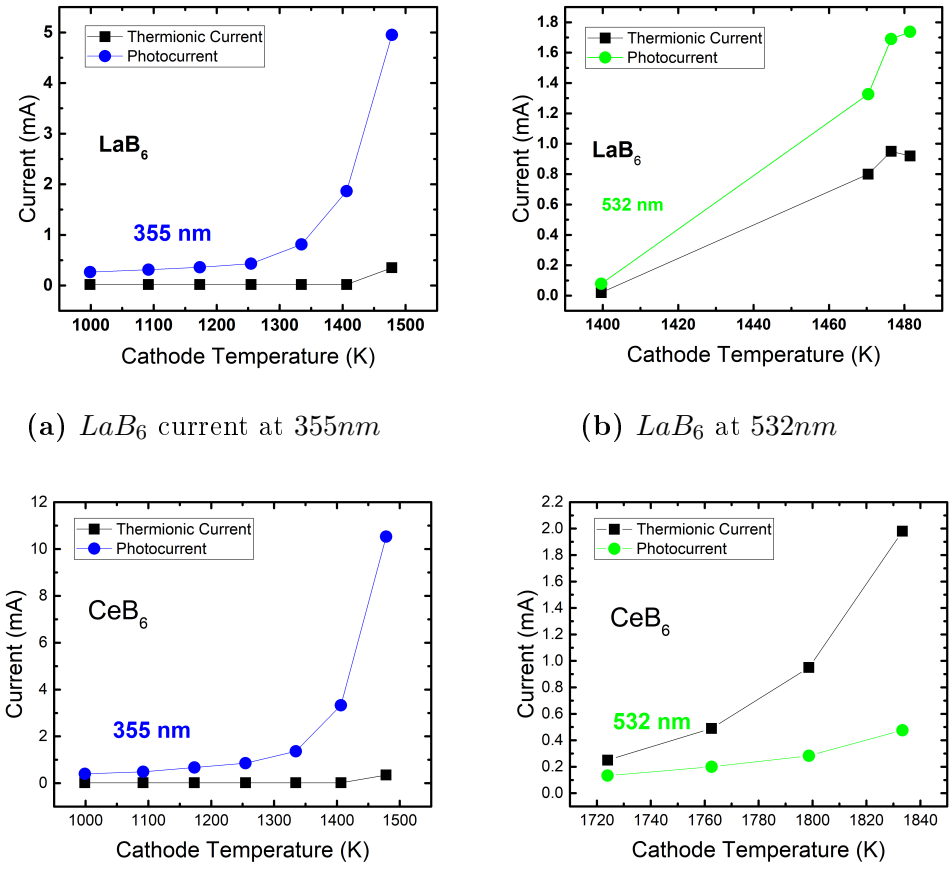

(a) LaB_6 current at $355nm$

(b) LaB_6 at $532nm$

(c) CeB_6 at $355nm$

(d) CeB_6 at $532nm$

Figure 5.10: Thermionic and Photocurrent for different cathode temperatures. (a) LaB_6 for excitation by laser of $355nm$ at $12\mu J$ and (b) excitation at $532nm$ with $84\mu J$. (c) CeB_6 for excitation by laser at $355nm$ with $\sim 13\mu J$ and (d) excitation at $532nm$ with $\sim 32\mu J$.

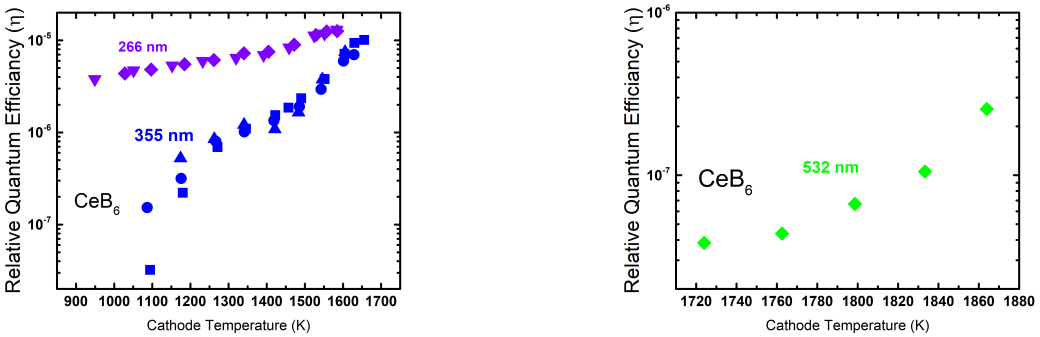

(a) CeB_6 at $1340K$ **(b)** CeB_6 at $1800K$

Figure 5.11: Results of relative quantum efficiency measurement of CeB_6 cathode being irradiated at 3 different laser wavelengths. (a) Irradiation by $266nm$ and $355nm$. (b) Irradiation by $532nm$.

the cathode temperature even if material degradation has taken place.

5.6.4 Laser Power Dependence Below Work Function

Electron extraction by laser photon energy below the work function can also be accomplished by two photon excitation processes. In Ref.[101] the authors have tried to perform electron extraction on LaB_6 below the work function. They had reported significant instability of emitted current and suggested a nonlinear process of photoemission. In order to exclude this option, the laser pulse energy dependence was measured. Figure 5.12 displays the dependency of photoemission current of LaB_6 (Fig.5.12a) and CeB_6 (Fig.5.12b) on the incident laser pulse energy at $532nm$ with the cathode temperature of around $1340K$ and $1800K$ respectively. The photon energy at this wavelength is lower than the work function. In this measurement, the integrated charge of the pulse had too small of a signal

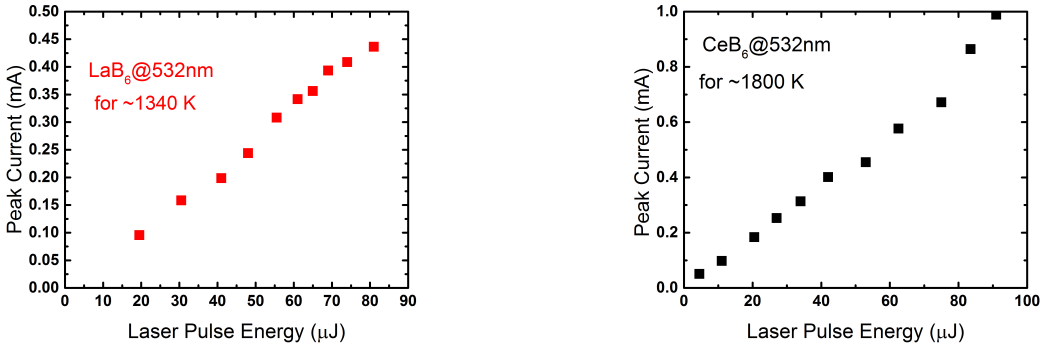

(a) LaB_6 at $1340K$ **(b)** CeB_6 at $1800K$

Figure 5.12: Dependence of the peak photoemission current on laser pulse energy at $532nm$. (a) LaB_6 for the cathode temperature of around $1340K$. (b) CeB_6 for the cathode temperature of around $1800K$. For (a) and (b) the laser illuminated area was $1.72mm$ in diameter [86].

to noise ratio. Therefore, the peak value of the current pulse was measured and plotted as the vertical axis of Fig.5.12. The linear correlation of peak current with laser pulse energy is obvious. Thus in our setup the photoelectron extraction below the work function assisted by cathode heating is a one photon absorption process.

5.6.5 Surface Effects

A hysteresis like-behavior of photocurrent was observed by the heating and cooling procedure.

Figure 5.13 shows the recorded hysteresis-like behavior, which differs for each excitation wavelength. The data points were recorded in a short time interval of around 1-2min. This tendency indicates changing surface conditions. By cooling down the photoemission current is higher than by heating up at the same cathode temperature. It can be

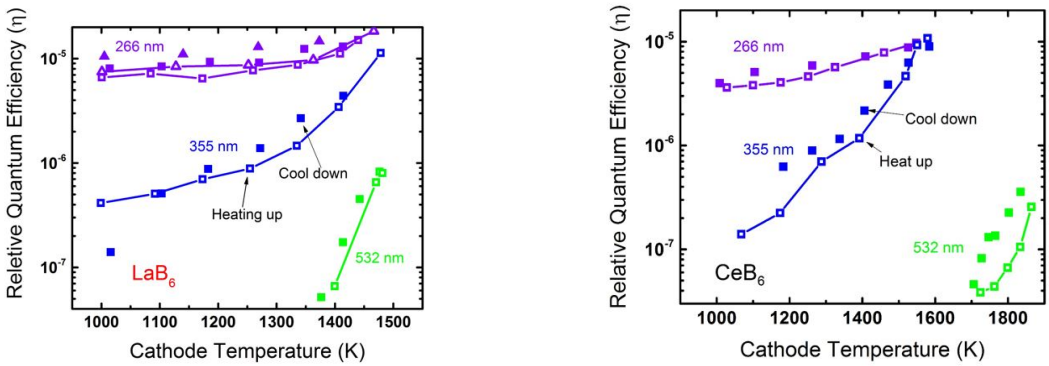

(a) Surface effect of LaB_6 **(b)** Surface effect of CeB_6

Figure 5.13: Relative QE as obtained under irradiation at 266, 355 and 532nm laser as function of cathode temperature during heating up and cooling down processes [86].

understood as the removal of surface contamination during the heating up process. In particular, in Ref.[102], it was reported that below a critical temperature the cathode surface is covered by an oxide layer. This layer can be removed by heating above the critical temperature. Thereby the surface oxide reduces the QE.

Hysteresis-like behavior was also observed for CeB_6 which is shown in Figure 5.13b. Hysteresis was observed for all applied laser wavelengths. The data presented in previous sections was acquired by heating up the cathode. The measurements of cooling down process were not considered. The width of the hysteresis can be smaller at lower vacuum pressure conditions ($< 10^{-8}Torr$). As one can see in Fig.5.13b, the surface effect is weaker than the TAPE effect.

5.6.6 Summary of Experimental Results

In general the heating of the cathode gives a bi-exponential rise for the photon-energies of $4.66eV$ and $3.49eV$ over temperature range of $1000 - 1600K$, as shown in Fig.5.8

and 5.11a. The excitation using photon-energy below the work function ($2.33eV$) has a mono-exponential rise of photocurrent over $1500-1600K$. The cathode heating causes the change of surface composition, which is shown as a hysteresis-like behavior in the Fig.5.13. The impact is relatively small (up to 30%). Thus the surface impurity is not the main reason for the photocurrent increase. According to the linear dependence of quantum efficiency on laser power, the photoemission as measured by our setup is resulting from one-photon absorption process.

Noteworthy is the fact that another group has reported a bi-exponential temperature assisted QE rise for a different type of material (Ir_5Ce) [103]. This fact indicates that the considered phenomenon is not material specific, but can be demonstrated only at materials with high melting point. According to the photoemission theory a bi-exponential rise is not expected. In the following part of the chapter the photoemission theory is considered based on measurements made for LaB_6 in order to elucidate the photo-excitation mechanisms.

5.7 Fowler-DuBridge Theory

In this section a classical photoemission theory from metal, the so called *Fowler-DuBridge* (FdB) theory is considered to explain the measurement results. As a matter of fact, the current emitted from a material is linearly proportional to the incident laser irradiance if the sum of the absorbed photon energy and the momentum component of the electron normal to the surface is greater than the work function (linear regime). The relation between the current density J and the Quantum Efficiency QE can be expressed as:

$$J(h\nu) = QE(1 - R(h\nu))I(\frac{q}{h\nu}), \tag{5.4}$$

with reflectivity R, laser intensity I, electron charge q and photon energy $h\nu$. The correlation between material heating and the photo-emitted current was developed by Fowler and

improved by DuBridge (FdB) [104], [105]. The theory is based on following assumptions [106]:

- Electrons in the bulk material obey Fermi-Dirac statistics with uniform distribution in momentum space.
- The probability for an electron to absorb a photon doesn't depend on the initial state of the electron.
- An electron can be emitted into vacuum if its kinetic energy with momentum normal to the surface is greater than the work function.
- The absorption of a photon increases only the kinetic energy of the electron with velocity component normal to the surface.
- The number of emitted electrons is proportional to the number of excited electrons whose kinetic energy, increased by photon absorption, is greater than the work function.

The FdB theory was extended to many photon processes by J.Bechtel [107]. The total photon current density is expressed as the sum over partial currents:

$$J_{tot} = \sum_{n=0}^{\infty} J_n. \tag{5.5}$$

Each partial current is described by:

$$J_n = a_n A(\frac{q}{h\nu})^n (1 - R(h\nu))^n I^n T^2 F(\frac{nh\nu - \phi}{k_B T}). \tag{5.6}$$

Where n is a number of photons used to excite an electron, a_n (with the unit $(cm^2s/C)^n$) is a material dependent coefficient, which includes all of the physical processes not considered by Eq.5.6 (scattering, escape probability, etc.). The $A = 120\ cm^{-2}K^{-2}$ is the Richardson constant, $k = 8.617 \times 10^{-5}eV$ is the Boltzmann constant, R is the surface reflectance, ϕ is the work function and T is the mean temperature of the surface. The $F(x)$ is a *Fowler function*, which is defined as [104]:

$$F(x) = \begin{cases} e^x - \frac{e^{2x}}{2^2} + \frac{e^{3x}}{3^2} - ... & \text{x<0} \\ \frac{\pi^2}{6} + \frac{x^2}{2} - (e^{-x} - \frac{e^{-2x}}{2^2} + \frac{e^{-3x}}{3^2}) & \text{x>0.} \end{cases}$$

The first term of the partial current density ($n = 0$) corresponds to the Richardsonâ-Dushman equation. In our experiment the DC thermionic current was separated from the pulsed photocurrent using a capacitor coupling. Therefore the first term $J_0(n = 0)$ is disregarded. For fitting of the measured photocurrent by FdB equation the modified material constant $a = a_n(1 - R)$ was adjusted to the measured value around the temperature of $1000K$ (first measurement point). For $2.33eV$ the adjustment point corresponds to another cathode temperature ($1400K$). The results are plotted in the Fig.5.14. The corresponded material constants are $a(4.66eV) = 1.88 \times 10^{-6} \pm 6 \times 10^{-11}cm^2s/C$, $a(3.49eV) = 5.95 \times 10^{-7} \pm 2 \times 10^{-9}cm^2s/C$ and $a(2.33eV) = 2.31 \times 10^{-5} \pm 4 \times 10^{-7}cm^2s/C$ respectively. Figure 5.14 demonstrates that the measured values and calculated results have large discrepancy. There are obviously some temperature dependent physical effects involved in the thermally assisted electron extraction, which are not considered by the FdB theory. This fact attracts attention since it provides a method to improve the QE.

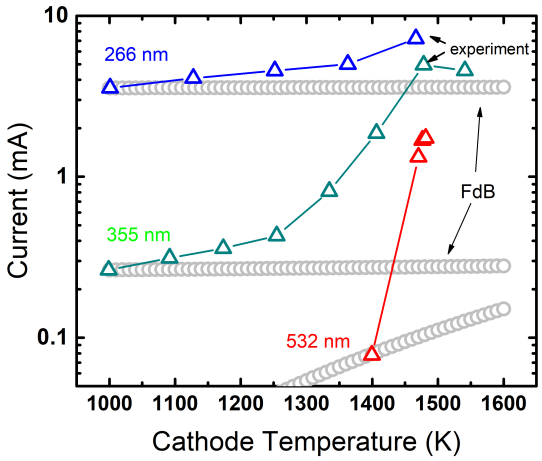

Figure 5.14: The fit of photocurrent by FdB equation (Eq.(5.6)) for three laser wavelengths (266, 355 and 532nm) [108].

5.7.1 Modification of the FdB-Theory

The photon dependent thresholds of the rise of photocurrent as observed using excitation by 4.66eV and 3.49eV, indicate the difference in band structure of electrons excited by various photon-energies. Therefore, it is reasonable to consider the influence of the structure of electronic density of states (DOS) on the temperature dependence of photocurrent. The LaB_6 has a simple cubic crystal structure with one lanthanum (La) atom embedded into a framework of six boron atoms ($B6$) in octahedral configuration. The Figure 5.2 illustrates the corresponding crystal structure. The valence states of La and B are $5s2$, $5p6$, $5d1$, $6s2$ and $2s2$, $2p1$, which contribute to the total electronic density of states [109]. The DOS of LaB_6 is shown in Fig. 5.15a [110]. A well-like feature of the DOS is found near the Fermi energy. That DOS can be approximated by a simple 2-D structure as illustrated in the Fig. 5.15b.

Similarly to the FdB approach the photocurrent density can be modelled using the Som-

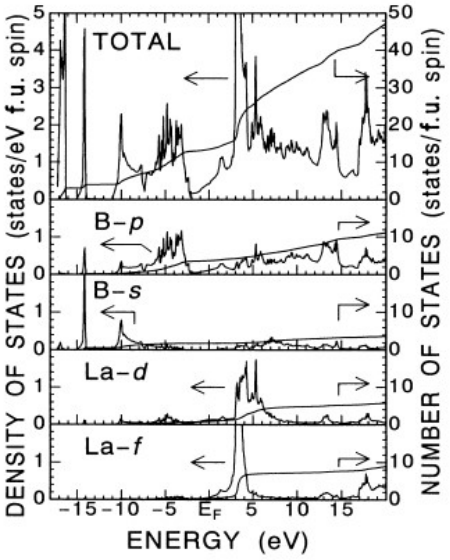

(a) Density of states of LaB_6 [110].

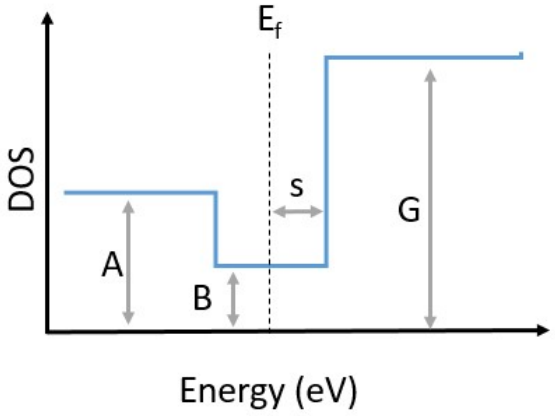

(b) Well-shaped 2-D model representing the total DOS [108].

Figure 5.15: Density of states of LaB_6 and the 2-D model.

merfeld free electron gas model. The number of electrons per second per unit area with energy dE with momentum component normal to the surface is:

$$N(T, E_f, E)dE = \frac{4\pi m k_B T}{h^3} ln(1 + exp(-\frac{E - E_f}{k_B T}))dE. \tag{5.8}$$

With electron mass m, Plank constant h and Fermi energy E_f. The current density is proportional to the integral over the energy deposited by photon.

$$J(h\nu, T) = C(h\nu)\frac{q4\pi m k_B T}{h^3} \int_{E_\nu - h\nu}^{E_\nu} ln(1 + exp(-\frac{E - E_f}{k_B T}))dE. \tag{5.9}$$

The free electron gas model assumes constant density of states $g(E) = const.$, which is included in the integral pre-factor. In order to account for the energy dependent density of states the integral is amended:

$$J(h\nu, T) = C(h\nu)\frac{q4\pi m k_B T}{h^3} \int_{E_\nu - h\nu}^{E_\nu} g(E) ln(1 + exp(-\frac{E - E_f}{k_B T}))dE. \tag{5.10}$$

$$g(E) = AH(E) - BH(E - E_f + s) + (G - 1)H(E - E_f - s), \tag{5.11}$$

Table 5.2: Fitting parameters

Wavelength (nm)	266	355	532
Photon energy (eV)	4.66	3.49	2.33
Laser energy (μJ)	12.5	13	32
$a(cm^2s/C)$	$1.88e^{-6}$	$5.95e^{-7}$	$2.31e^{-5}$
C$(h\nu)$	$7.096e^{4}$	$3.115e^{4}$	$4.54e^{6}$

with proportionality constant $C(h\nu)$. The well-like structure is defined by $g(E)$ using a Heaviside function $H(E)$ with the well-height factors A, B, G and the well width s (see Fig.5.15). The LaB_6 has a metallic character [111], therefore the Fermi energy was set to $E_f = 7eV$ as a typical value for metals. The vacuum level $E_v = 9.7eV$ corresponds to the sum of the work function and the Fermi energy. The well-height factors are set according to the ratio from the LaB_6 DOS (see Fig.5.15a).

The Figure 5.16a shows the difference between photocurrents according to the Eq.5.6 and the Eq.5.10, which has an order of 10^{-3}. Such uncertainty is negligible for our consideration, which empowers us to assume the Eq.5.10 being equivalent to Eq.5.6. The corresponding fitting proportionality constants are: $C(4.66eV) = 7.096 \times 10^{-4} \pm 6$, $C(3.49eV) = 3.115 \times 10^{4} \pm 60$ and $C(2.33eV) = 4.54 \times 10^{6} \pm 8 \times 10^{4}$ respectively. The fitting parameters are summarized in the Table 5.2.

The meaning of the integration constants becomes evident by comparison with the reported QE ratio at the corresponding wavelengths. For example the values for dispenser cathode are $QE(4.66eV) = 3.5 \times 10^{-4}$, $QE(3.49eV) = 1.4 \times 10^{-4}$, $QE(2.33eV) = 2.3 \times 10^{-5}$ [112]. The corresponding ratio are $QE(4.66eV)/QE(3.49eV) = 2.5$ and $QE(4.66eV)/QE(2.33eV) = 15.2$. The ratio of integration constants are $a(4.66eV)/a(3.49eV) = 3.15$, $a(4.66eV)/a(2.33eV) = 0.081$ and $C(4.66eV)/C(3.49eV) = 2.28$, $C(4.66eV)/C(3.49eV) =$

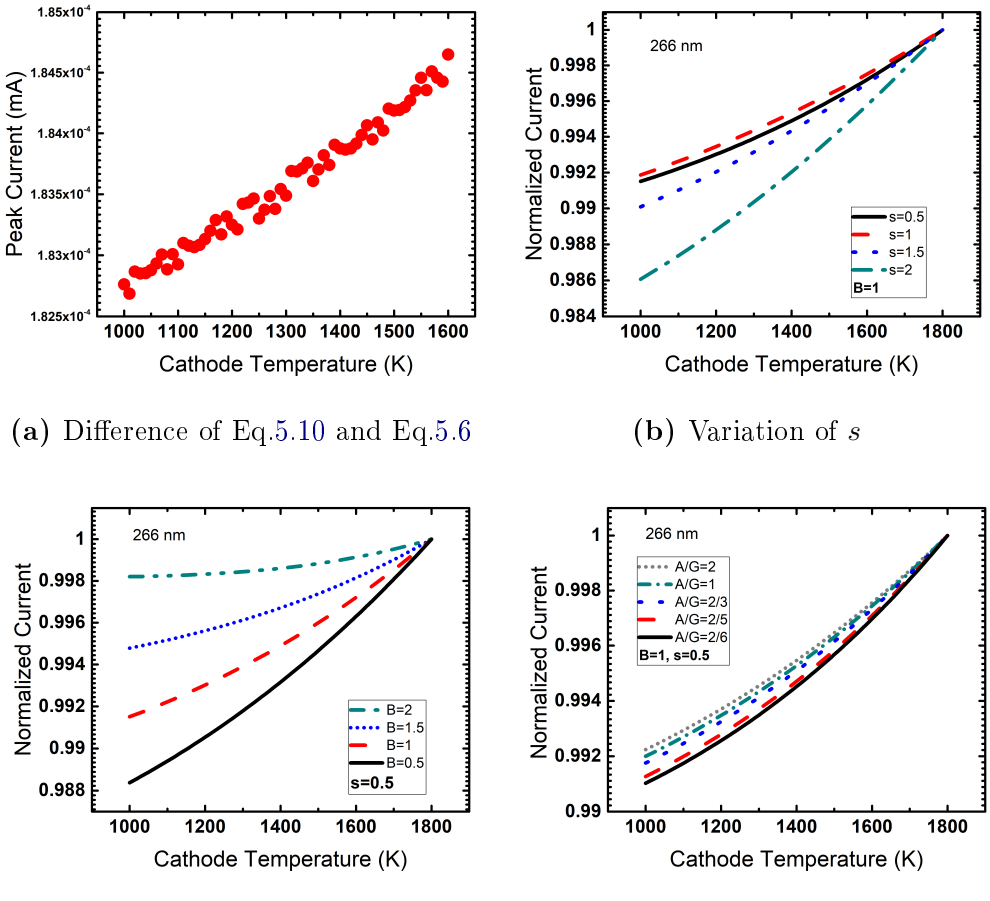

(a) Difference of Eq.5.10 and Eq.5.6

(b) Variation of s

(c) Variation of B

(d) Variation of A/G

Figure 5.16: Parameter variation for the 2-D well structure of the LaB_6 DOS [108].

0.016. The value for $QE(4.66eV)/QE(3.49eV)$ for dispenser cathode has the same magnitude for corresponding LaB_6 ratio of QE, a and C. This fact shows that the integration constants a and C are proportional to the quantum efficiency of LaB_6. Whereas, the values at $2.33eV$ are two orders of magnitudes lower than that of dispenser cathode. This disagreement is understandable since the integration constant for $2.33eV$ was fitted for much higher temperature.

The photocurrent was investigated under variation of the width s, the height B and the A/G ratio of the well structure applying the Eq.5.10. The results are shown in the Fig.5.16b, 5.16c, 5.16d with normalized y-axis. The figures demonstrate that the variation of those three parameters does not affect the temperature dependent emission significantly (in the order of 10^{-3}).

These results indicate that the structure of density of states does not affect the photoemission significantly if the occupation of states follows the Fermi-Dirac statistics as assumed by FdB theory. Other processes for distribution of electrons would be the inter- and intra-band transitions, which do occur for LaB_6 [113],[114]. However, a study on those processes requires more experimental data, in particular the kinetic energy distribution of photocurrent. Since this data is not available, the corresponding considerations are outside of the scope of this work.

5.8 Transmission Coefficient

As discussed before, the free electron gas model is not sufficient to describe the photoemission at high cathode temperatures. For further discussion the photon-energy δE, which is required to obtain the measured thermally assisted increase in photon-current,

is considered. Therefore the measured photocurrent $J_{meas}(h\nu, T)$ is compared with the photocurrent $J_{FdB}(h\nu, T)$ calculated according to the Eq.5.9.

$$\frac{J_{meas}(h\nu, T)}{J_{FdB}(h\nu, T)} = \frac{I(1 - R(h\nu))QEq/h\nu}{I(1 - R(h\nu))QEq/(h\nu + \delta E)} = \frac{h\nu + \delta E}{h\nu}. \tag{5.12}$$

The δE is plotted versus cathode temperature in the Fig.5.17. Considering the first slope of photocurrent, the δE reaches up to $2eV$. This energy has an obvious relation to the excess energy $E_{ex} = h\nu - \phi$, which electrons obtain after absorption of high energy photons. The values corresponding to the electron excess energy $E_{ex}(= 1.96eV, 0.79eV)$ according to photon-energies of $4.66eV$ and $3.49eV$ are indicated in the Fig.5.17 by horizontal lines. The values of δE exceed the E_{ex} at higher temperature for photon energy of $3.49eV$. This fact makes evident that the E_{ex} is not directly affecting the rise in photocurrent. It seems that the E_{ex} changes the escape probability $D(E_{ex})$ of the electron reaching the surface with proper energy. To support this suggestion the Eq.5.9 is modified according to the general electron emission form [115]:

$$J_D(h\nu, T) = C_1(h\nu, T)\frac{q4\pi m k_B T}{h^3}\int_{E_\nu - h\nu}^{E_\nu} D(E_{ex}) ln(1 + exp(-\frac{E - E_f}{k_B T}))dE. \tag{5.13}$$

Usually the transmission coefficient is a convolution of external electric field and the potential barrier at the surface.

The $D(E_{ex})$ can be approximated as:

$$D(E_{ex}) = \frac{1}{(1 + exp(\frac{E_0 - E}{\beta_F}))}. \tag{5.14}$$

where the E_0 is an expansion point and β_F is an energy dependent slope factor [116]. The precise parameters have to be determined by modelling. The excess energy is related to

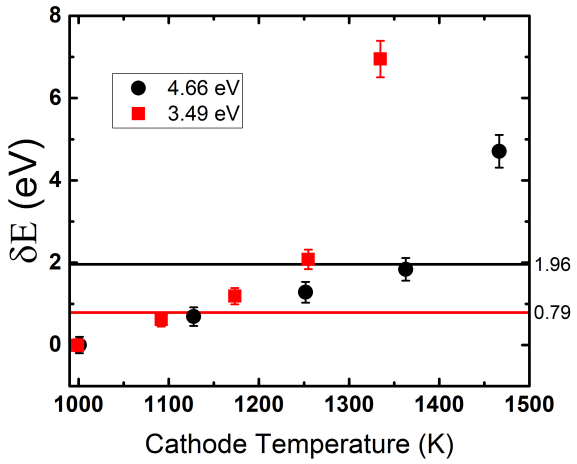

Figure 5.17: The energy required for temperature dependent increase of QE for photo-excitation by $3.49eV$ and $4.66eV$ [108].

energy by $E_{ex} = E - (E_v - h\nu)$.

An empirical ansatz allows us to make an acceptable approximation to the measurement results. The Figure 5.18 shows that the first slope can be fitted well by appropriate choice of the integration constant $C_1(h\nu)$ and $D(E_{ex})$. The Figure 5.18a shows the $D(E)$ for photon-energies $4.66eV$ and $3.49eV$ at $1000K$. The corresponding parameters are $C_1(3.49eV) = 3.9 \times 10^5$, $C_1(4.66eV) = 4.8 \times 10^5$, $E_0(3.49eV) = 1.2$, $E_0(4.66eV) = 2$ and $\beta_F(3.49eV) = 4k_BT$, $\beta_F(4.66eV) = 8k_BT$. The simple ansatz for $D(E_{ex})$ as assumed before, does not fit the second slope, as shown in Fig.5.18b for $4.66eV$ and $3.49eV$. For it, an accurate modelling is required.

As for now, the origin of photon energy dependent transition from the first slope to the second slope is not clear. Possible explanation could be:

- Change of the surface barrier due to the thermally excited electrons.
- Change of photon absorption probability by the bulk electron due to the high tem-

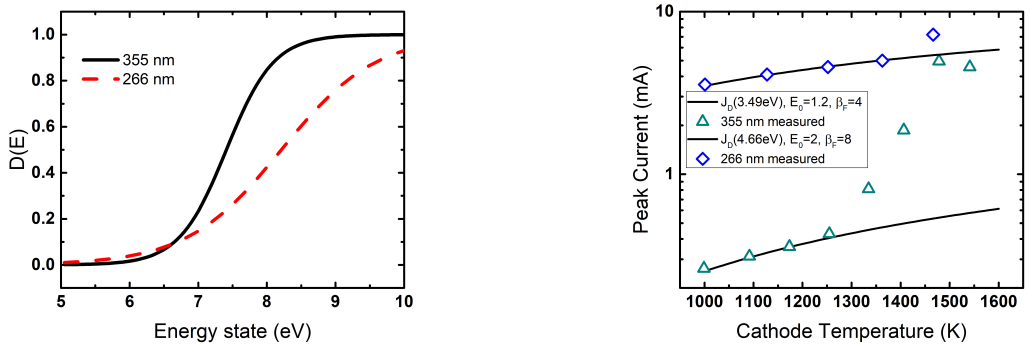

(a) Transmission coefficient for $T = 1000K$. **(b)** Fitting of experimental results.

Figure 5.18: Fitting results for the the first slope of photocurrent at $4.66eV$ and $3.49eV$ [108]. (a) Electron escape probability. (b) Photocurrent.

perature.

By introduction of the transmission coefficient it is intended to make a suggestion for possible emission mechanisms and to indicate the direction for further research. The issue of determining of correct transmission coefficient remains a matter of precise mathematical modelling.

5.9 Summary

In the present chapter the thermally assisted photoemission (TAPE) of LaB_6 and CeB_6 cathodes was investigated by measuring quantum efficiencies under various cathode temperature and excitation photon-energy conditions. It was demonstrated that the quantum efficiency increases with cathode temperature along with thermionic emission. The TAPE effect becomes more significant for lower excitation photon energy. By this means the excitation at $355nm$ can generate the same photocurrent as excitation at $266nm$ at sufficient

high temperature. Especially for excitation with photon energy below the work function, the TAPE is essential to achieve photoemission. The measurement of laser pulse energy dependence revealed that the excitation process under our experimental conditions was a one-photon absorption. Comparing the quantum efficiency of LaB_6 and CeB_6 cathodes, the LaB_6 had a higher quantum efficiency than that of CeB_6 at the same temperature for all tested laser photon-energies. This tendency corresponds to the thermal emission properties of these two materials.

In general, the photocurrent was significantly higher than the thermionic current. However, for CeB_6 at $532nm$ the photocurrent was lower than the thermionic one. During the measurements, a hysteresis-like behavior of quantum efficiency dependence on the cathode temperature was observed. When the cathode temperature was cooled down from a higher temperature, the quantum efficiency was slightly higher than that measured during the heating up process. This behavior indicates a change of surface conditions. In order to avoid this discrepancy a proper laser cleaning of the cathode is required before conducting the experiment.

The Fowler-DuBridge photoemission theory could not explain the results. The influence of the density of state structure also doesn't have significantly the photocurrent. The change in photoemission escape probability of the photo-excited electrons have demonstrated promising results for describing the measured results.

5.10 Conclusions

The study described in this chapter was conducted as proof of principles for increasing the quantum efficiency of the cathode when a thermionic RF gun is being operated in photo-excitation mode. The feasibility of increase in quantum efficiency using the ohmic

heating of the cathode was successfully demonstrated. As for the laser system, when amplifier is used, the increase of quantum efficiency enables extension of macropulse (see the section 5.1).
The increase of quantum efficiency does not correspond to the classical photoemission theory. This fact indicates that there are some photo-excitation mechanisms involved, which are not considered by the theory. Further research on this field has a potential to provide new understanding of the electron extraction mechanisms, which could be eventually a tool to analyze material properties.
It was also demonstrated that photoemission can take place using the excitation with photon-energy below work function as one-photon absorption. This effect was demonstrated for CeB_6 for the first time.
As for the application of TAPE on the 4.5-cell RF gun of KU-FEL, further study on TAPE under RF accelerating conditions would be required.

The results of the study described in this chapter were partially published/submitted in following articles:

- K. Torgasin et al., "Thermally assisted photoemission effect on CeB_6 and LaB_6 for application as photocathodes" DOI:10.1103/PhysRevAccelBeams.20.073401
- K. Morita et al., "Photoemission properties of LaB_6 and CeB_6 under various temperature and incident photo energy conditions", WEOAB03, Proceedings of IPAC2016, Busan, Korea, pp. 2088-2090, 2016.
- K. Torgasin et al., "Study on anomalous photoemission of LaB_6 at high temperatures", submitted Oct. 2018.

The content taken from the published paper is presented in this chapter with friendly permission of the publisher, American Physical Society (APS). The list of copyright owned

content and figures is given in appendix.

Chapter 6

Summary

The research described in this thesis was conducted with the aim to test two methods for improvement of performance of thermionic RF gun. The RF gun, to which these methods are intended to be applied, is used at Kyoto University-Free Electron Laser (KU-FEL) facility. The improvement of the RF gun would allow us to extend the spectral range and to increase the radiation power of the KU-FEL.

The KU-FEL was constructed at the Institute of Advanced Energy (IAE), Kyoto University for study on materials related to energy harvesting e.g. wide gap semiconductors. In this way the thesis can be considered contributing to the energy science.

The 4.5-cell RF gun, which is used to generate the electron beam for the KU-FEL, can be operated in thermionic and photo-excitation modes. In thermionic mode the macropulse radiation energy can be further improved by increasing the electron bunch charge and electron beam macropulse duration. This goal can be achieved by reduction of the Back-Bombardment Effect (BBE). In the photo-excitation mode the improvement can be attained increasing the quantum efficiency of the cathode. In this thesis both methods were investigated as a proof of principles:

1. Feasibility of triode-type thermionic RF gun configuration for reduction of the BBE.
2. Feasibility of quantum efficiency increase by Thermally Assisted Photoemission (TAPE).

1. Triode-type thermionic RF gun

The triode concept of thermionic RF gun concerns the installation of an additional quarter wavelength pre-bunching cavity to a conventional RF gun. The design of the pre-bunching (triode-) cavity and the installation of the power line were done in previous studies. The study described in this thesis concerned the hot and cold tests under low and high input power conditions of the triode cavity. The corresponding experimental work and results were described in the chapter 4.

The tests of the triode cavity have following results:

- The cold test has shown that the triode cavity can accept cavity voltage up to 22.7 kV. If the input power exceeds this value some discharge phenomena occur.
- During the hot test discharges were detected at the beginning ($13 - 22kV$ rising field) and at the end ($1 - 2kV$ decaying field) of the macropulse.
- The hot test has demonstrated that at specific heating power ($> 4.45W$, $1350K$) the reflected power rises over 90 % (changed coupling condition) and low current during the macropulse is detected.
- The detected current at such condition has low frequency and heating current dependence.

- The changed coupling conditions are power dependent.

These characteristics indicate the occurrence of multipactoring. According to the estimation by 2-wall model, the multipactoring corresponds to the distance between the cathode holder and the aperture nose of the cavity ($1.3mm$ for $1kV$). The beam tracking study has shown that the cathode holder is hit by the back-streaming electrons and the aperture is hit by the electron beam due to high divergence at low cathode voltage. The impact of electrons is higher on the cathode holder ($> 1kW$ for cavity voltage $> 20kV$) than on the aperture ($> 100W$ for cavity voltage $> 20kV$) during one RF period. This fact suggests that the Secondary Electron Emission (SSE) is initiated at the cathode holder. The SSE is getting in resonant conditions with the driving RF frequency and evolves to the multipactoring.

This study demonstrates that the design of the triode cavity was limited to desires beam parameters. The influence of low voltage effects like SSE were neglected (the simulation code did not include the multipactoring). This information is useful for general design of small sized cavities. The research described in this thesis has advanced the knowledge about operation of pre-bunching cavity, however, the test of triode-type thermionic RF gun could not be completed.

.

2. Thermally Assisted Photoemission

The influence of cathode temperature on quantum efficiency, when excited by laser was studied as a proof of principles in a DC test bench. This study was described in the chapter 5. The target of the test of TAPE is to increase the Quantum Efficiency (QE) of

the cathode without increasing costs for improvement of laser system.
The tests on the feasibility of TAPE were successful. The results are:

- The QE was raised by temperature at 3 photon energies (2.33, 3.49 and $4.66eV$).
- The QE was raised by one order of magnitude (excited by $3.49eV$).
- The electron emission was achieved using photon energy below the work function (at $1470K$ for $2.33eV$, with work function of $2.7eV$) as one photon absorption.
- The rise of QE of LaB_6 is higher than that of CeB_6

An unexpected result is the photon energy dependent bi-exponential rise of QE with temperature (for photon energy over work function). According to the classical photoemission theory the rise must be a mono-exponential. The origin of this phenomenon is not clear yet.
The study on the change of electron density of states of the cathode material, showed that the differences in DOS structure can not explain the bi-exponential rise. There is a strong evidence that the potential barrier of the cathode is changing with cathode temperature, which leads to the increase of escape probability of excited electrons.

The study on TAPE has shown that cathode temperature can rise the QE unexpectedly high. This is a very important finding for the $R\&D$ of cathode materials.

6.1 Perspectives

1. Triode type thermionic RF gun

The proof of principles for triode cavity system can be considered as successful until the stage of cold test. For further progressing, the generation of a stable electron beam has to be demonstrated. However, it is prevented by the multipactoring process taking place between the cathode holder and the aperture. The multipactoring process is initiated by the back-streaming electrons with low energy, which is unavoidable in thermionic RF systems. Because of the small dimensions the cavity geometry benefits the resonant multipactoring. It is very important to maintain the designed geometry (especially the aperture area), which allows pre-bunching at designed parameters of the electron beam. The finding that the multipactoring is initiated at the cathode holder makes it possible to apply countermeasures without significant modification on cavity geometry. The multipactor suppressing measure, which could be applied is for example a coating of the cathode holder, aiming to increase the secondary emission energy threshold. Another method is the introduction of periodical grooves onto the cathode holder, aiming to change the resonant conditions for the SEE. Owing to the special structure of the triode cavity, the multipactoring countermeasures can be applied to the present cavity, since the cavity is consisting from the two separable parts. Such structure is an innovative advantage of the cavity design. For the final confirmation of the multipactoring location and the effectiveness of countermeasures, a corresponding simulation has to be conducted (modification of the calculation code). In this view point there are good perspectives to complete the hot test of the triode cavity. The outgoing experimental work will concern the electron beam characterization and the integration of the triode cavity to the 4.5-cell RF gun of the KU-FEL, completing the proof-of principles.

In general the triode approach has a potential to be adapted to any electron thermionic RF gun, since it has a compact structure and does not require big changes in the beamline. According to simulations, the triode approach can mitigate the impact of the BBE by 80%, which would be a significant improvement for the stability of the beam energy. At BBE less conditions the extension of the spectral range and increase in lasing power of KU-FEL is expected.

2. Thermally Assisted Photoemission

As for the proof of principles of a Thermally Assisted Photoemission (TAPE), the results were successful. It was demonstrated that the increase of temperature can rise the quantum efficiency of the cathode (up to one order of magnitude). This result could allow us to increase the bunch charge using lower laser power. In case of application of a laser amplifier, the increase of quantum efficiency would allow extending the laser macropulse duration. Furthermore the TAPE makes it possible to extract electrons using photon-energy lower than the work function by single photon absorption. This principle was demonstrated for CeB_6 for the first time.
Besides of mentioned findings an additional effect was detected. The quantum efficiency is rising in a bi-exponential slope (for photon energy over the work function). The origin of such behaviour is not clear now. As for the application of TAPE at the 4.5-cell RF gun of KU-FEL, further study on TAPE under RF accelerating conditions are required.

6.2 Conclusions

In general the laser excitation can't be applied to conventional thermionic RF guns,which were not designed for laser excitation, since it requires an additional window for laser incidence (or an aperture with big diameter). Moreover a laser system is an expensive device and is difficult in operation. From this point of view the triode approach has clear advantages in compactness simplicity in operation and moderate costs.
In conclusion, the triode system, when proved to be successful, has a good chance to be developed to a commercial thermionic injector for oscillator type FEL facilities. In contrary, the TAPE has the potential to increase the quantum efficiency of cathodes, but does not enable us to use laser excitation as an equivalent alternative to thermionic injectors for oscillator type FEL.

I have a hope that the research described in this thesis would find application in other fields studying on electron beam generation, such as material study, medical diagnostics, safety inspections.

Publication List

This section contains the list of publications made during the work on this thesis.

Journal Papers

- K. Torgasin, K. Morita, H. Zen, K. Masuda, M.Bakr, K. Nagasaki, T. Kii, and H. Ohgaki
  Study on Anomalous Photoemission of LaB6 at High Temperatures, journal paper, submitted Oct. 2018.

- K. Torgasin, K. Mishima, H. Zen, K. Yoshida, H. Negm, M. Omer, T. Kii, K. Nagasaki, K. Masuda, and H. Ohgaki
  Properties of Quarter Wavelength Coaxial Cavity for Triode-Type Thermionic RF Gun, Jpn. J. Appl. Phys., 56. 096701, (2017).

- K. Torgasin, K. Morita, H. Zen, K. Masuda, T. Katsurayama, T. Murata, S. Suphakul, H. Yamashita, T. Nogi, T. Kii, K. Nagasaki, H. Ohgaki
  Thermally Assisted Photoemission (TAPE) Effect on CeB_6 and LaB_6 for Application as Photocathodes, Phys. Rev. Accel. Beams 20, 073401 (2017).

Conference Papers

- K. Torgasin, H. Zen, T. Kii, K. Nagasaki, K. Masuda, and H. Ohgaki
  Study on Secondary Electron Emission of a Quarter Wavelength Coaxial Cavity for Triode-Type Thermionic RF Gun, submitted July 2018, (Poster presentation at SFR2018).

- K. Torgasin, H. Zen, T. Kii, K. Nagasaki, K. Masuda, and H. Ohgaki
  Methods for Counteracting the Back-Bombarding Effect for thermionic RF guns, submitted July 2018, (Oral presentation at SFR2018).

- K. Torgasin et al., *Coaxial Quarter Wavelength Impedance Converter for Coupling control of Triode Cavity*,
  (RuPAC) Russian Particle Accelerator Conference, Nov. 21-25, 2016, St. Petersburg, Russia. Proceeding paper, p.689-691.

- K. Torgasin et al., *Cold Test of the Coaxial Cavity for Thermionic Triode Type RF Gun*,
  (IPAC) International Particle Accelerator Conference, Mai 12-17, 2013, Shanghai, China. Proceeding paper, p.324-326.

- K. Torgasin et al., *Practical Design of Resonance Frequency Tuning System for Coaxial RF Cavity for Thermionic Triode RF Gun*,
  The 34th International Free Electron Laser Conference, August 26-31, 2012, Nara, Japan, Proceeding paper, p.333-336.

Acknowledgement

In course of the work on this thesis I had to face the challenge of combination of research with a new lifestyle. The lifestyle in Japan is a special one due to the complexity in human relationship. But without establishing good relationship it is difficult to conduct experiments successfully. Under this circumstances the main challenge for me was the establishment of good relation to colloquies and other people surrounding me in daily life. First of all I have to mention our group leader Prof. Nagasaki. He is a very kind person, who has an open mind for people with different cultural background. Prof. Nagasaki was the first Japanese person, who advised me to enjoy life in Japan during my study. I am very grateful to my supervisor Ass. Prof. Kai Masuda. He is a knowledgeable researcher, who is managing the supervision of several projects in different fields at the same time. Especially remarkable is that Dr. Masuda sets the main emphasis on research as a process of obtaining knowledge, which should be useful for the society. Furthermore I owe him thank for employing me for NEDO project.

Regarding my experimental work, I have greatly benefited from the cooperation with the group of Prof. Ohgaki, where I have got a strong technical and scientific support. The feedback I have obtained from Prof. Ohgaki and Ass. Prof. Kii at the FEL-Meetings were very useful. I am very thankful for our collaboration. In this context I would like to express my special gratitude to Dr. Heishun Zen. He is a very patient and experienced researcher, who devotes a lot of his effort to support students. Dr. Zen has an exemplary attitude towards problem solving. If some problems are reported, he guides with useful advises until the problem is solved or recognized as being not solvable. Especially valuable were his comments regarding published reports on conferences and papers submitted in journals. Dr. Zen has also built my image of a traditional Japanese working style:-'A cat might bring luck, but success is obtained by own effort'. As for documentary issue, most of the students

of the Laboratory of Prof. Nagasaki have assisted me with phone calls and communication in Japanese language. Especially the secretaries Ms. Murata, Ms. Yamamura, Ms. Nakao and Keiko Nakamura they have helped me to cope with administrative work and with numerous translations. I owe them my gratitude. I have got a lot of help by learning about Japan and Japanese customs. I would like to show my greatest appreciations to my friends from Osaka language group, especially to Mrs. Tokieda, Mr. Michitoshi, Mrs. Moriuka, Mrs. Emily, Mrs. Kazu and Mr. Shibamura. Another person whom I want to thank is Mr. Shimotani. He is helping to international students by all available means. Thanks to his activity I have got acquainted with interesting people. An important role in my social life in Japan have played my international friends. I will omit to mention all their names, and since the most important friends came to my defence, I would like to thank to all the people who has attended this event on their own will and to them who wanted to attend but was prevented by some circumstances. Finally my deepest gratitude goes to my family for their patience and support.

Bibliography

[1] IAE web-page, http://www.iae.kyoto-u.ac.jp/en/organization/generation/quantum.html

[2] Patrick G. O'Shea and Henry P. Freund, *Free-Electron Lasers: Status and Applications*, Science, Vol. 292, No. 5523, pp. 1853-1858, 2001. doi:10.1126/science.1055718, http://science.sciencemag.org/content/292/5523/1853

[3] Kyohei Yoshida, *Direct observation of mode-selective phonon excitation for bulk material by MIR-FEL*, Ph.D. thesis, Graduate School of Energy Science, Kyoto University, Kyoto, Japan, Sept. 2014.

[4] Heishun Zen, *Generation of high quality electron beam using a thermionic RF gun for mid-infrared free electron lasers*, Ph.D. thesis, Graduate School of Energy Science, Kyoto University, Kyoto, Japan, Mai 2009.

[5] H. Zen et al., *Feasibility study of photocathode operation of thermionic RF gun at KU-FEL*, in Proc. IPAC'16, Busan, Korea, 2016, pp. 754-756.

[6] C. B. McKee and J. M. J. Madey, *Computer simulation of cathode heating by back-bombardment in the microwave electron gun*, in Proceedings of the

Eleventh International Free Electron Laser Conference, Aug. 1989, pp. 716-719, doi:10.1109/FEL.1989.716096.

[7] T. Kii et al., *MIR-FEL with 4.5-cell thermionic RF-gun*, in Proc. LINAC'08, 2008, pp. 477-479.

[8] H. Ohgaki, T. Kii, K. Masuda, H. Zen, S. Sasaki, T. Shiyama, R. Kinjo, K. Yoshikawa, and T. Yamazaki, *Lasing at* $12\mu m$ *Mid-Infrared Free-Electron Laser in Kyoto University*, Jpn. J. Appl. Phys. Vol. 47, No. 10R. p. 8091, 2009.

[9] D. H. Dowell, *High brightness electron injectors for 4th generation light sources*, U. S. Particle Accelerator School, Lecture notes, 2007. http://uspas.fnal.gov/materials/08UCSC/HBl1%20_Intro_and_Motivation.pdf

[10] C. Hernandes-Garcia, P. G. O'Shea, and M. L. Stutzman, *Electron sources for accelerators*, AIP, S-0031-9228-0802-030-9, 2008. http://www.physicstoday.org/

[11] D. H. Dowell, *Electron emission and cathode emittance*, U.S. Particle Accelerator School, Lecture notes, 2010. http://uspas.fnal.gov/materials/10MIT/Lecture2_EmissionStatisticsCathodeEmittance_text.pdf/

[12] W. E. Spicer and A. Herrera-Gómez, *Modern theory and application of photocathodes*, SLAC-PUB-6306, pp. 1-16, Aug. 1993.

[13] A. Modinos, *Field, Thermionic, and Secondary Electron Emission Spectroscopy*, Plenum, New York, 1984.

[14] D. H. Dowell, *Electron emission and cathode emittance*, U.S. Particle Accelerator School, Lecture notes, June 2010. http://uspas.fnal.gov/materials/08UCSC/Lecture2_EmissionStatisticsCathodeEmittance.pdf

[15] J. W. Gerwatowski and H. A. Watson, *Principles of electron tubes*, D. Van Nostrand Company, Inc., 1965. http://www.westernelectric.com/support-principles-of-electron-tubes.html

[16] R. L. Sheffield, *High-brightness electron injectors: a review*, IEEE in PAC, pp. 1098-1102, 1989.

[17] W. B. Herrmannsfeldt, *Low emittance thermionic electron guns*, SLAC-PUB-4843, pp. 1-11, Jan. 1989.

[18] G. A. Westenskow and J. M. J. Madey, *Microwave electron gun*, Laser and particle beams. Vol. 2, Part 2, 2232, 1984.

[19] C. Travier, *Review of microwave guns*, Particle Accelerators, Vol. 36, pp. 33-74, 1991. http://www.sciencemag.org

[20] Tutorialspoint, *Microwave engineering-transmission lines*, https://www.tutorialspoint.com/microwave_engineering/microwave_engineering_transmission_lines.htm

[21] T. P. Wangler, *Principles of RF linear accelerators*, Willer Interscience Publication, John Wiley and Sons, Inc., 1998.

[22] F. Furuta et al., *Measurement of field emission dark current from the titanium, copper, and stainless steel electrodes under the high DC-field gradient condition*, in Proc. LINAC'02, 2002, Gyeongju, Korea, pp. 431-433.

[23] J. C. Travier, *RF Guns: Bright Injectors for FEL*, Nucl. Instrum. Methods Phys. Res., A **304**, pp. 285-296, 1991.

[24] C. B. McKee, M. J. Madey,*Optimization of a thermionic microwave electron gun*, Nucl. Instrum. Methods Phys. Res., A 304, pp. 386-391, 1991.

[25] J. M. D. Kowalczyk, M. R. Hadmack, and J. M. J. Madey, *Measurement of back-bombardment temperature rise in microwave thermionic electron guns*, Rev. Sci. Instrum. 84, p. 084905, 2013.

[26] S. O. Cho et al., *Time-resolved measurement of electron beam emittance and energy spread with optical transition radi-ation*, Nucl. Instrum. Methods Phys. Res., A **407**, pp. 359-363, 1998.

[27] T. Kii et al., *Evaluation of thermal effects due to back-streaming electrons in the IAE RF gun*, Nucl. Instrum. Methods Phys. Res., A **483**, pp. 310-314, 2002.

[28] C. B. McKee and M. J. Madey, *Optimization of a thermionic microwave electron gun*, Nucl. Instrum. Methods Phys. Res., A **296**, pp. 386-391, 1990.

[29] Y. Huang and J. Xie, *Measures to alleviate the back-bombardment effect of thermionic RF electron gun*, in Proc. PAC'91, San Francisco, USA, May 1991, pp. 2017-2019.

[30] Hongxiu Liu, *Simulation studies on back bombardment of electrons in RF thermionic guns*, Nucl. Instrum. Methods Phys. Res., A **302**, pp. 535-546, 1991.

[31] J. M. D. Kowalczyk and J. M. J. Madey, *Back-bombardment compensation in microwave thermionic electron guns*, Phys. Rev. Spec. Top. Accel. Beams 17, p. 1204023, 2014.

[32] E. Z. Biller et al., *High-temperature metallic cathode for RF gun*, Problems of Atomic Science and Technology, ser. Nuclear Physics Research (39), No. 5, pp. 103-105, 2001.

[33] M. Bakr et al., *Comparison of the heating properties of LaB_6 and CeB_6 due to the back-bombardment effect in a thermionic RF gun*, J. Kor. Phys. Soc., Vol. 59, pp. 3273-3279, 2011.

[34] M. Bakr et al., *Back bombardment for dispenser and lanthanum hexaboride cathodes*, Phys. Rev. Spec. Top. Accel. Beams 14, pp. 2824-2829, 2011.

[35] M. Satoh et al., *Compensation of initial beam loading for electron linacs*, in Proc. 7th Europ. Particle Accelerator Conf. (EPAC 2000), Vienna, Austria, June 2000, paper THP5A07, pp. 2462-2464.

[36] T.Kii, et al., *Reducing energy degradation due to back-bombardment effect in S-band thermionic RF gun*, in Proc. 9th Int. Conf. Synchrotron Radiation Instrumentation (SRI 2006), Daegu, Korea, May 2006, paper AIP CP879, pp. 248-251.

[37] T.Kii, et al., *Reducing back-bombardment effect using thermionic cathode in IAE RF gun*, in Proc. 26th Int. Free-Electron Laser Conf. (FEL'04), Trieste, Italy, Sept. 2004, paper TUPOS21, pp. 443-446.

[38] H. Zen et al., *Beam energy compensationin a thermionic RF gun by cavity detuning*, IEEE Trans. Nucl. Sci., Vol. 56, No. 3, pp. 1487-1491, 2009.

[39] J. R. Harris and P. G. O'Shea, *Gridded electron guns and modulation of intense beams*, IEEE Trans. Electron Devices, Vol. 53, No. 11, pp. 2824-2829, 2006.

[40] V. Trebich, *Simulation of thermionic RF gun with a grid*, Nucl. Instrum. Methods Phys. Res., A **345**, pp. 417-420, 1994.

[41] H. P. Bluem et al., *High brightness thermionic electron gun performance*, in Proc. ERL'11, Tsukuba, Japan, Oct. 2011, paper WG1010, pp. 30-35.

[42] V. Volkov et al., *CW 100 mA electron RF gun for Novosibirsk ERL FEL*, in Proc. RuPAC'16, St. Petersburg, Russia, Nov. 2016, paper TUCAMH02, pp. 24-26.

[43] Y. Zou et al., *Theoretical study of transverse emittance growth in a gridded electron gun*, Nucl. Instrum. Methods Phys. Res., A **519**, pp. 432-441, 2004.

[44] C. Mitchell, P. Sprangle, and J. Peñano, *A gridded thermionic injector gun for high-average power free-electron-lasers*, IEEE Trans. Plasma Sci., Vol. 4, No. 8, pp. 1977-1983, 2012.

[45] I. V. Khodak and V. A. Kushnir, *Method of electron emission control*, Issues of Atomic Science and Technology, Ser. Nuclear-physical research (38), No. 3, pp. 68-70, 2001.

[46] Xiao Fu Du and Chuan Xiang Tang, *A microwave thermionic gun with harmonic cavity*, in Proc. APAC'01, Beijin, China, Sept. 2001, paper TUBU06, pp. 526-528.

[47] J. P. Edelen et al., *Electron back-bombardment and mitigation in a short gap, thermionic cathode RF gun*, IEEE Trans. Nucl. Sci., Vol. 61, No. 2, pp. 830-831, 2014.

[48] K. Kanno and E. Tanabe, *Design of back-bombardment less thermionic RF gun*, Jpn. J. Appl. Phys., Vol. 41, pp. 62-64, 2002.

[49] AET, http://www.aetjapan.com/

[50] K. Torgasin et al., *Properties of quarter-wavelength coaxial cavity for triode-type thermionic RF gun*, Jpn. J. Appl. Phys. 56, 096701 (2017).

[51] E. Tanabe et al., *A 2 MeV microwave thermionic RF gun*, SLAC-PUB-5054, 1989.

[52] M. Borland, *A high-brightness thermionic microwave electron gun*, Ph.D. thesis, Department of Energy, Stanford University, Stanford, USA, 1991.

[53] V. V. Mitrochenko, *Thermionic RF gun with high duty factor*, in Proc. PAC'97, Vancouver, Canada, May 1997, paper 3W034, pp. 2817-2819.

[54] C. Tang et al., *A multi-cell RF electron gun with thermionic cathode for the Beijin Free Electron Laser*, Nucl. Instrum. Methods Phys. Res., A **421**, pp. 406-410, 1999.

[55] E. Tanabe et al., *A novel structure of multi-purpose RF gun* in Proc. LINAC'98, Chicago, USA, Aug. 1998, pp. 162-164.

[56] F. Oda et al., *The properties of on-axis coupled structure RF gun*, Nucl. Instrum. Methods Phys. Res., A **445**, pp. 404-407, 2000.

[57] J. W. Lawellen, *Energy-spread compensation of a thermionic-cathode RF gun*, in Proc. PAC'03, Portland, USA, May 2003, paper WPAB003, p. 2035.

[58] T. Tanaka et al. *An independently tunable cells thermionic RF gun (ITC-RF gun) for sub-picosecond short pulse*, in Proc. FEL'05. Stanfort, USA, Aug. 2005, paper MOPP043, pp. 142-145.

[59] N. Y. Huang et al., *Beam characteristics measurement of ITC-RF gun for t-ACTS project*, in Proc. PASJ'11, Osaka, Japan, Aug 2012, paper WEUH06, pp. 51-53.

[60] X. Li et al., *Progress in reducing the back-bombardment effect in the ITC-RF gun for t-ACTS project at Tohoku University*, in Proc. IPAC'12, New Orleans, USA, May 2012, paper MOPPP036, pp. 643-645.

[61] Y.J. Pei et al., *R&D a compact EC-ITC RF gun for FEL*, in Proc. IPAC'10, Kyoto, Japan, May 2010, paper TU-PEC013, pp. 1737-1739.

[62] Hu Tong-Ning et al., *Physical design of FEL injector based on performance enhanced EC-ITC RF gun*, Chinese Phys., C38 018101.

[63] Y. Otake, *Overview of SACLA machine status*, in Proc. LINAC'12, Tel-Aviv, Israel, Sept. 2012, paper TU2A02, pp. 427-431.

[64] M. Borland, *Simulation of cathode back-bombardment in a 100 MHz thermionic RF gun*, in Proc. LINAC'10, Tsukuba, Japan, Sept. 2010, paper THP0872.

[65] Y. Yamamoto, T. Inamasu, K. Masuda, M. Sobajima, M. Ohnishi, K. Yoshikawa, H. Toku, and E. Tanabe, *Simulations of electron backstreaming in a microwave thermionic RF gun*, Nucl. Instrum. Methods, A **393**, 443 (1997).

[66] K. Masuda, T. Kii, T. Yamaguchi, H. Toku, K. Yoshikawa, and T. Yamazaki, Int. J. Appl. Electrom., Vol. 14, No. 1-4, pp. 163-170, 2001/2002.

[67] H. Zen, T. Kii, K. Masuda, R. Kinjo, K. Higashimura, K. Nagasaki, and H. Ohgaki, *Beam energy compensation in a thermionic RF gun by cavity detuning*, IEEE Trans. Nucl. Sci., Vol. 56, No. 3, 1487 (2009).

[68] T. Kii, H. Zen, K. Higashimura, R. Kinjo, K. Masuda, and H. Ohgaki, *MIR-FEL with 4.5-cell thermionic RF gun*, in Proc. LINAC'08, 2008, p. 477.

[69] H. Zen et al., *Present status of mid-infrared free electron laser facility at Kyoto University*, in Proc. IPAC'13, Shangai, China, 2013, p. 1190.

[70] T. Shiyama, *Generation of high brightness thermal electron beam with long pulse duration by using triode RF gun structure*, MS. thesis, Graduate School of Energy Science, Kyoto University, Kyoto, Japan, 2008. [in Japanese].

[71] K. Masuda et al., *Design study of RF triode structure for the KU-FEL thermionic RF gun*, in Proc. FEL'06, 2006, pp. 656-659.

[72] T. Shiyama, K. Masuda, H. Zen, S. Sasaki, T. Kii, and H. Ohgaki, *A triode-type thermionic RF gun for drastic reduction of back−streaming electrons*, in Proc. FEL'07, 2007, pp. 398-401.

[73] K. Torgasin et al., *Properties of quarter-wavelength coaxial cavity for triode-type thermionic RF gun*, Jpn. J. Appl. Phys. 56, 096701 (2017).

[74] M. Takasaki, *Design and characterization of a coaxial RF Cavity for thermionic triode RF gun*, MS. thesis, Graduate School of Energy Science, Kyoto University, Kyoto, Japan, 2011. [in Japanese]

[75] K. Torgasin et al., *Practical design of resonance frequency tuning system for coaxial RF cavity for thermionic triode RF gun*, in Proc. FEL'12, Nara, Japan, 2012, pp. 333-336.

[76] K. Masuda et al., *Transient beam loading effects due to back-streaming electrons onto a thermionic cathode in an RF gun*, Nucl. Instrum. Methods, A **483**, pp. 315-320, 2002.

[77] K. Masuda, *Development of numerical simulation codes and application to klystron efficiency enhancement*, Ph.D. thesis, Graduate School of Electrical Engineering, Kyoto University, Kyoto, Japan, 1997.

[78] K. Mishima et al., *Numerical Study on Electron Beam Properties in Triode Type Thermionic RF Gun*, in Proc. FEL'013, 2013, pp. 344-347.

[79] Scientific Instrument Services, Inc. (SIS). 2003-2005. http://simion.com/definition/richardson_dushman.html/

[80] K. Torgasin et al., *Cold test of the coaxial cavity for thermionic triode type RF gun*, in Proc. IPAC'13, Shanghai, China, 2013, pp. 324-326.

[81] K. Torgasin et al., *Study on secondary electron emission of quarter wavelength coaxial cavity for triode type thermionic RF electron gun*, submitted July 2018.

[82] D. Proch et al., *Measurement of multipacting current of metal surfaces in RF fields*, in Proc. PAC'95, 1995, pp. 1776-1778.

[83] P. Tolis, *On secondary electron emission and its semi-empirical description*, in Plasma Phys. Control. Fusion 56 (2014) 123002.

[84] K. Torgasin et al., *Coaxial quarter wavelength impedance converter for coupling control of triode cavity*, in Proc. RuPAC'16, St. Petersburg, Russia, Nov. 2016 p. 691.

[85] T. Abe et al., *Multipactoring suppression by fine grooving of conductor surfaces of coaxial-line input couplers for high beam current storage rings*, Phys. Rev. ST. Accel. Beams, 102001, (20010), DOI: 10.1103/PhysRevSTAB.13.102001.

[86] K. Torgasin et al., *Thermally assisted photoemission effect on CeB_6 and LaB_6 for application as photocathodes*, DOI:10.1103/PhysRevAccelBeams.20.073401.

[87] H. Zen et al., *Development of photocathode drive laser system for RF guns in KU-FEL*, in Proc. FEL'14, Basel, Switzerland, 2014, pp. 828-831.

[88] M. Asakawa et al., *Experimental studies of photocathode materials for FELs*, Nucl. Instr. and Meth., A **331**, pp. 302-306, 1993.

[89] S. Thorin et al., *Characterization of the beam from thermionic RF-gun adapted for photo cathode operation*, in Proc. FEL'09, Liverpool, UK, 2009.

[90] S. Giermann et al., *Operating a tungsten dispenser cathode in photo-emission mode*, in Proc. PAC'09, Vancouver, Canada, 2009.

[91] P. G. O'Shea et al., *Radio frequency photoinjector using LaB6 cathode and a nitrogen drive laser*, App. Phys. Lett., Vol. 73, No. 3, 20 July 1998.

[92] D. J. Bamford et al., *The search for rugged, efficient photocathode materials*, Nucl. Instrum. Methods, A **318**, pp. 377-380, 1992.

[93] S. Mogren et al., *Thermionic and threshold photoemission energy distributions from LaB6 (110)*, Surface Science 186, pp. 232-246, 1987.

[94] M. Boussoukaya et al., *Pulsed photocurrents from lanthanum hexaboride cathodes in the ns regime*, Nucl. Instrum. Methods, A **264**, pp. 131-134, 1988.

[95] J. M. Lafferty, *Boride Cathodes*, J. Appl. Phys., 22, 299 (1951).

[96] M. Bakr et al., *Comparison between hexaboride materials for thermionic cathode RF gun*, in Proc. IPAC'10, Kyoto, Japan, pp.1782-1784.

[97] M. Bakr et al., *Comparison of the heating properties of LaB_6 and CeB_6 to the back bombardment effect in a thermionic RF gun*, J. Kor. Phys. Soc., Vol. 59, No.5, Nov. 2011, pp. 3273-3279.

[98] Technical datasheet. https://www.emsdiasum.com/microscopy/technical/datasheet/80920.aspx

[99] P. van der Heide et al., *Differences between LaB_6 and CeB_6 by means of spectroscopic ellipsometry*, J. Phys. F: Met. Phys., 16, pp. 1617-1623, 1986.

[100] K. Morita, *Research on dependence of LaB_6 and CeB_6 photocathodes on temperature and incident laser wavelength and modeling*, MS. thesis, Graduate School of Energy Science, Kyoto University, Kyoto, Japan, 2017. [in Japanese]

[101] B. Leblond et al., *Short pulse photoemission from LaB_6- based materials*, Nucl. Instrum. Methods, A **372**, pp. 562-566, 1996.

[102] M. Aono et al., *Direct observation of LaB_6 (001) surface at high temperatures by x-ray and ultraviolet photoelectron spectroscopy, and work-function measurements*, J. Appl. Phys. 50, 4802 (1979); 10.1063/1.326542.

[103] D. Satoh, M. Yoshida, and N. Hayashizaki, *Development of better quantum efficiency and long lifetime iridium cerium photocathode for high charge electron RF gun*, in Proc. Of IPAC2013, Shanghai, China, MOP-FI023, pp. 327-329.

[104] R. H. Fowler, *The analysis of photoelectronic sensitivity curves for clean metals at various temperatures*, Phys. Rev. vol. 38, 45, pp.41-56, 1931.

[105] L. A. DuBridge, *Theory of the energy distribution of photoelectrons*, Phys. Rev. vol. 38, 45, pp. 727-741, 1933.

[106] G. Ferrini et al., *Non-linear electron photoemission from metals with ultrashort pulses*, Nucl. Instrum. Methods Phys. Res., Sect. A, vol. 601, pp.123-131, 2009.

[107] J. H. Bechtel, *Laser induced electron emission*, Ph.D. thesis, University of Michigan, Michigan, USA, 1973.

[108] K. Torgasin et al., *Study on anomalous photoemission of LaB_6 at high temperatures*, submitted Oct. 2018.

[109] F. M. Hossain, D. P. Riley, and G. E. Murch, *Ab initio calculations of the electronic structure and bonding characteristics of* LaB_6, Phys. Rev. B: Condens. Matter 72, p. 235101, 2005.

[110] S. Kimura et al., *Electronic structure of rare-earth hexaborides*, Phys. Rev. B: Condens. Matter, vol. 46, no. 19, pp. 196-204, 1992.

[111] E. Krauer, *Optical and electrical properties of* LaB_6, Phys. Lett., vol. 7, no. 3, pp. 171-173, 1963.

[112] B. Leblond, *Short pulse photoemission from a dispenser cathode under the 2nd, 3rd and 4th harmonics of picosecond Nd:YAG laser*, Nucl. Instrum. Methods Phys. Res., Sect. A **317**, pp. 365-372, 1992.

[113] S. Kimura, *Interband optical spectra of rare-earth haxaborides*, J. Phys. Soc. Jpn., vol. 59, no. 9, pp. 3388-3392, 1990.

[114] N. Singh, S. M. Saini, T. Nautiyal, and S. Auluck, *Electronic structure and optical properties of rare earth hexaborides* RB_6 *(R=La, Ce, Pr, Nd, Sm, Eu, Gd)*, J. Phys.: Condens. Matter 19, p. 346226, 2007.

[115] S. G. Christov, *Unified theory of thermionic and field emission from superconductors*, Phys. Status Solidi 21, 159, 1967.

[116] K. J. Jensen, and M. Cahay, *General thermal-field emission equation*, Appl. Phys. Lett. 88, p. 154105, 2006.

[117] P. J. Neyman et al., *Free Electron Lasers in 2017*, in Proc. FEL'17, Santa Fe, NM, USA, paper MOP066, 2017, pp. 204-209.

[118] Large-Area Picosecond Photo-Detectors Project, web page, http://psec.uchicago.edu/library/photocathodes/klaus_overview_table.pdf/

Copyrights

The content of the chapter 4 was published in a modified version in Japanese Journal of Applied Physics https://doi.org/10.7567/JJAP.56.096701, the following figures were reproduced in this thesis with friendly permission of the publisher (©Japan Society of Applied Physics (JSAP)). Figures: 4.3, 4.4, 4.7, 4.8, 4.9, 4.11, 4.12, 4.13, 4.14, 4.17a, 4.18b, 4.19a, 4.20, 4.21, 4.22.

The content of the chapter 5 was published in a modified version in Physical Review Accelerators and Beams https://doi.org/10.1103/PhysRevAccelBeams.20.073401, the following figures were reproduced in this thesis with friendly permission of the publisher (©American Physical Society). Figures: 5.1, 5.3, 5.4a, 5.6a, 5.7, 5.8, 5.9, 5.12, 5.13.

LOCATION (NAME)	λ(μm)	t_b(ps)	E(MeV)	I(A)	N	λ_0(cm)	K(rms)	Type
Ariel (EA-FEL)	3000	5×10^7	1.4	0.5-3	26	4.44	0.8	EA,O
Frascati (FEL-CATS)	430-760	15-20	2.5	5	16	2.5	0.5-1.4	RF
UCSB (mm FEL)	340	25000	6	2	42	7.1	0.7	EA,O
Dresden (TELBE)	100-3000	0.15	15-34	15	8	30	≤5.7	RF,SU
Nijmegen (FLARE)	100-1400	3	10-15	50	40	11	0.5-3.3	RF,O
KAERI (THz FEL)	100-1200	20	4.5-6.7	0.5	80	2.5	1.0-1.6	MA,O
Novosibirsk (FEL1)	90-240	100	12	10	2x32	12	0-0.9	ERL,O
Osaka (ISIR, SASE)	70-220	20-30	11	1000	32	6	1.5	RF,S
Himeji (LEENA)	65-75	10	5.4	10	50	1.6	0.5	RF,O
UCSB (FIR FEL)	60	25000	6	2	150	2	0.1	EA,O
Osaka (ILE/ILT)	47	3	8	50	50	2	0.5	RF,O
Novosibirsk (FEL2)	37-85	20	22	50	32	12	0-1.1	ERL,O
Osaka (ISIR)	25-150	20-30	13-20	50	32	6	≤1.5	RF,O
Tokai (JAEA-FEL)	22	2.5-5	17	200	52	3.3	0.7	RF,O
Bruyeres (ELSA)	20	30	18	100	30	3.2	0.8	RF,O
Dresden (ELBE U100)	18-250	1-25	15-34	30	38	10	0.5-2.7	RF,O
Osaka (iFEL4)	18-40	10	33	40	30	8	1.3-1.7	RF,O
Novosibirsk (FEL3)	9	10	42	100	3x28	6	0.3-1.8	ERL,O
Darmstadt (FEL)	6-8	2	25-50	2.7	80	3.2	1.0	RF,O
Osaka (iFEL1)	5.5	10	33.2	42	58	3.4	1.0	RF,O
Nijmegen (FELICE)	5-100	1	18-50	50	48	6.0	1.8	RF,O
Dresden (ELBE U37)	5-40	0.8-4	15-34	60	54	3.7	0.5-1.34	RF,O
Beijing (BFEL)	5-25	4	30	15-20	50	3	0.5-0.8	RF,O
Kyoto (KU-FEL)	5-21.5	<1	20-36	17-40	52	3.3	0.7-1.56	RF,O
Daresbury (ALICE)	5-11	~1	27.5	80	40	2.7	0.35-0.9	ERL,O
Tokyo (MIR-FEL)	4-16	2	32-40	30	43	3.2	0.7-1.8	RF,O
Orsay (CLIO)	3-150	10	12-50	100	38	5	≤1.4	RF,O
Nijmegen (FELIX)	3-150	1	15-50	50	38	6.5	1.8	RF,O
Berlin (FHI MIR FEL)	2.9-50	1-5	15-50	200	50	4	0.5-1.5	RF,O
Hawaii (MkV)	2-10	2-5	30-45	30-60	47	2.3	0.1-1.3	RF,O
Osaka (iFEL2)	1.88	10	68	42	78	3.8	1.0	RF,O
Nihon (LEBRA)	1.5-6.5	1	58-100	10-20	50	4.8	0.7-1.4	RF,O
JLab (IR upgrade)	0.7-10	0.35	120	300	30	5.5	3.0	ERL,O

Figure 6.1: List of long wavelength FEL facilities for 2017 [117]

Table 6.1: Legend to the Figure 6.1

Accelerator type:	FEL type:
MA-Microtron Accelerator	A- FEL Amplifier
ERL-Electron Recovery Linear Accelerator	K- FEL Klystron
EA- Electrostatic Accelerator	O-FEl Oscillator
RF- Radio-Frequency Linear Accelerator	S- Self-Amplified Spontaneous Emission (SASE)
SR- Electron Storage Ring	H- Harmonic Generation (CHG, HGHG)
PW- Laser Plasma Wakefield Accelerator	E- Echo-Enabled Harmonic Generation (EEHG)

Photocathode material		Work function/ E_{photon} (eV)	QE	λ (nm)	Operational lifetime	Vacuum (Torr)	Response time	Reference
Metallic								
	Cu	4,3 - 4,7	0,014 %	266	Very long	10^{-7}	< ps	[1]
	Mg	3,66	0,06 %	266	> 5000 h	10^{-7}	< ps	[1]
			0,027 %	266				[b*]
	Mg (laser-cleaned)		0,20 %	266	Long	10^{-9} - 10^{-8}		[10]
	Y	2,9	0,05 %	266	Long	< 10^{-7}	< ps	[1]
	Sm	2,7	0,07 %	266	Long	< 10^{-7}	< ps	[1]
	Ba	2,5	0,10 %	337	Short-long	< 10^{-7}	< ps	[1]
	Nb	4	0,01 %	266				[23]
	Ca	2,9	0,05 %	248				[b*]
	Mg-Ba	low	0,10 %	266				[16]
Semiconductor								
Alkali-telluride	Cs_2Te	3,5	4 - 20 %	251 – 266	Few hours - months	10^{-10} - 10^{-9}	~ ps	
	CsTe +CsBr	4,1	5 - 6 %		> 2 months			[38]
			1,2 %	266	No difference	10^{-8}		[39]
	CsKTe	4,0 - 4,5	22,5 % 2 % at saturation	259	T1/2 = 1+12 h Tsat= 20 h Tstor = 100 h	10^{-9}		[20],[28], [29]
	K_2Te	4,5	1,6 %	266				[b*]
			1 - 3%	262				[27]
			2,6 %	254		10^{-11}		[24]
			4,75 %	259	Long	10^{-10} - 10^{-9}		[25]
			8,3 %					[26]
			8,9 %					[20]
	Rb_2Te	4,1	4,5 %	266				[b*]
	RbCsTe		7,7 %	266				[b*]

Figure 6.2: Overview over photocathodes: Metals and semiconductors [118].

Photocathode material		Work function/ $E_{photons}$ (eV)	QE	λ (nm)	Operational lifetime	Vacuum (Torr)	Response time	Reference
Alkali-antimonide	K_2CsSb	~2	8 %	527	T1/2 < 4 h	10^{-10} - 10^{-9}	~ ps	[1]
			3 %	532	T1/e > 1 h	10^{-10}		[19]
			4 %	534	T1/2 < 2 h	10^{-9}		[19], [29]
			6 %	543		10^{-11} - 10^{-10}		[19]
	KCsSb + CsBr		5 % 10%	312		150 0,1		[30],[37]
	Cs_3Sb	2	4 %	527	T1/2 < 4 h	10^{-10} - 10^{-9}	~ ps	[1],[19]
			2 %	266	Very short			[b*]
			0,38 %	532	1 to few hours	10^{-9}		[19]
			1,3 %	532		10^{-10}		[19]
			1 - 2%	527				[29]
			9 %	543		10^{-10} - 10^{-9}		[19]
	Cs_3Sb + NaI/CsI/HTC		1 %	312				[35],[36]
	K_3Sb	2,3	1,6 % 0,023%	266 523	Very short 1 to few hours			[b*]
			< 1%	527	Short			[29]
	Na_2KSb	2	6,1 % 0,02 %	266 532	Very short 1 to few hours			[b*]
	Li_2CsSb		100 %	all colors				[31]
Alkali-halide	CsI	6,3	2 %	209	T1/2 > 150 h	10^{-10} - 10^{-9}	> ps	[1],[b*]
			0,007%	262				
			20 %	180				[92]
	CsI-Ge	5	0,73 % 0,13 %	213 262	T1/e > 1 y (storage)			[27]

Figure 6.3: Overview over photocathodes: Semiconductors [118].

Photocathode material		Work function/ $E_{photons}$ (eV)	QE	λ (nm)	Operational lifetime	Vacuum (Torr)	Response time	Reference
NEA	DC GaAs		5 %	527	T1/e = 58 h	~ $5 \cdot 10^{-11}$		[93]
	GaAs (Cs)		1.5 - 6%	750	Short	10^{-11}	< ns	[1]
	GaN (CsO)	3,4	20 %	300	10h + T1/2 = 8h	10^{-10}		[94],[95]
	GaN (Cs)	<3.4	30 %	200				[96]
	Diamond	Large	> 1%	< 210	Very long		> ps	[1]
	Polycrystalline diamond		10^{-6}	266	Long			[33]
	Hydrogenated diamond		0,08 %	213		10^{-8}		[32]
	Nanostructured fullerine		0,002%	213		10^{-8}		[32]
Internal field-assisted	Ag-O-Cs, Ag-BaO Cu-O-Cs	Lowered by external bias	15,7% enhanced	510				[34]
Thermionic								
	LaB_6		0,1 %	355	~ 1 d	< 10^{-7}		[1]
	Thermionic dispenser		0,23 %	266	T1/2 = 12 h	$3*10^{-10}$	< 380 ps	[1],[7]
	Trioxide termionic		0,035%	266	T1/2 = 10 h	$3*10^{-10}$	< 400 ps	[1]
Ferroelectric								
	Ferroelectric		0,06 %	355	Very long	10^(-7)	< ns	[1],[8],[9]
	Ferroelectric ceramic		10^{-6}					[8],[9]

Figure 6.4: Overview over photocathodes: Semiconductors, thermionic materials and others [118].